Millimeter Wave Spatial Statistical Channel Model for High-altitude Military UAV Battlefield Situation Awareness

Jinsheng Yang[1], Huan Xi[1], and Zhou Pan[2]

[1]Tianjin University
[2]Tianjin Navigation Instrument Research Institute, Tianjin, China

February 27, 2023

Abstract

A high-altitude military UAV air-to-ground scenario model is established for the battlefield scenario without base station, the MIMO antenna array technology is used to improve the channel communication performance, and the spatial statistical channel model (SSCM) of this scenario is constructed in this paper. According to the simulation results, the dependence of the channel on T-R separation distance, frequency, rain rate and antenna HPBW parameters was investigated, the large-scale fading and small-scale fading characteristics was analyzed. By calculating and analyzing the condition number and rank of the channel transmission matrix, the spatial multiplexing under different MIMO antenna arrays was investigated. The simulation results can provide a theoretical basis for future high-altitude military UAV battlefield situation awareness frequency selection and antenna design.

Hosted file

`956915_0_art_file_10729651_rqfnkr.docx` available at https://authorea.com/users/589412/articles/626259-millimeter-wave-spatial-statistical-channel-model-for-high-altitude-military-uav-battlefield-situation-awareness

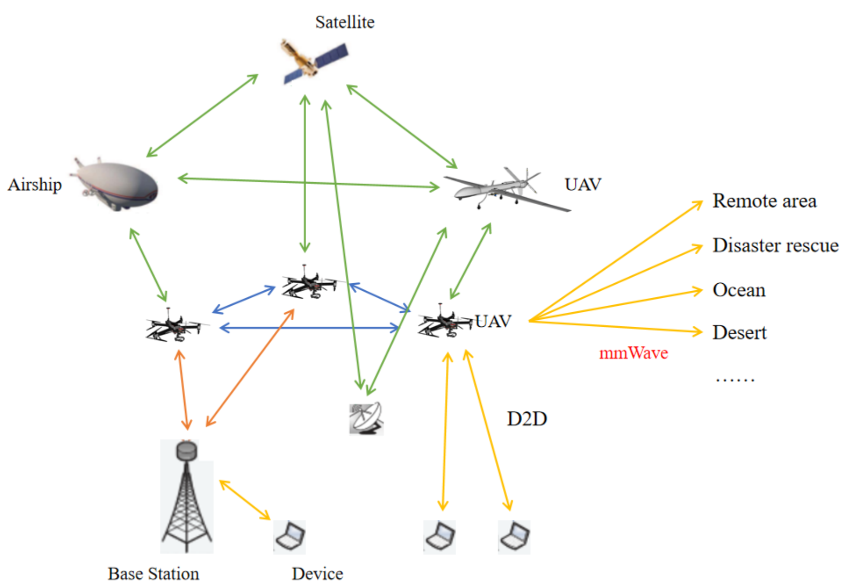

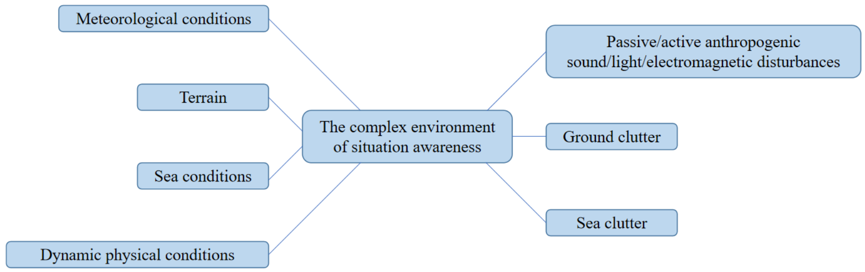
Meteorological conditions
Terrain
Sea conditions
Dynamic physical conditions
The complex environment of situation awareness
Passive/active anthropogenic sound/light/electromagnetic disturbances
Ground clutter
Sea clutter

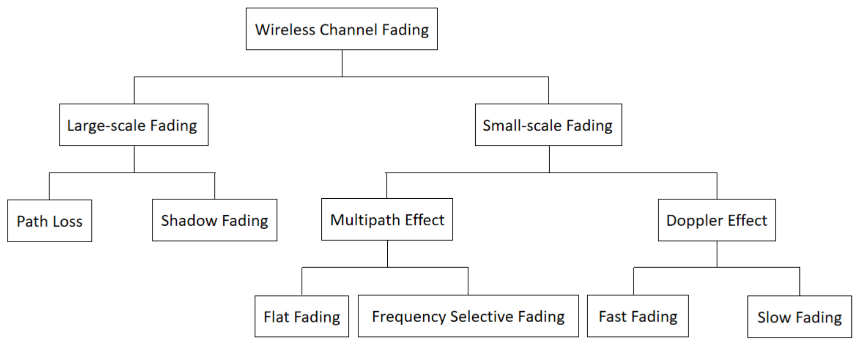
Wireless Channel Fading
Large-scale Fading
Small-scale Fading
Path Loss
Shadow Fading
Multipath Effect
Doppler Effect
Flat Fading
Frequency Selective Fading
Fast Fading
Slow Fading

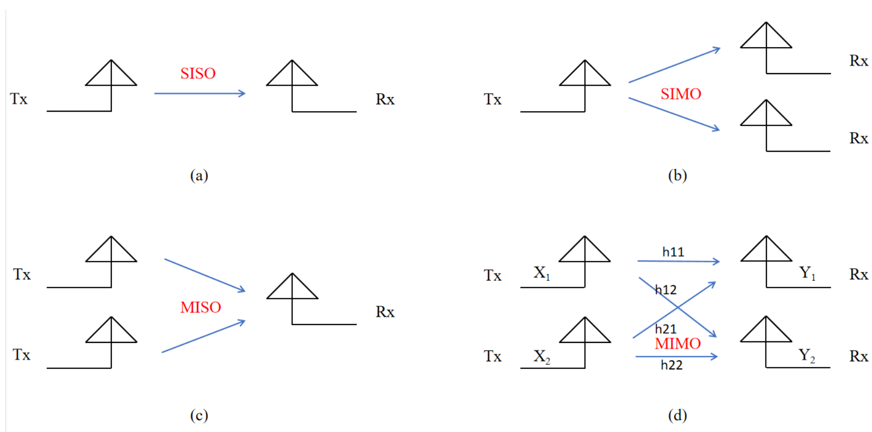
Tx
SISO
Rx
(a)
Tx
SIMO
Rx
Rx
(b)
Tx
Tx
MISO
Rx
(c)
Tx
X1
Tx
X2
h11
h12
h21
MIMO
h22
Y1
Y2
Rx
Rx
(d)

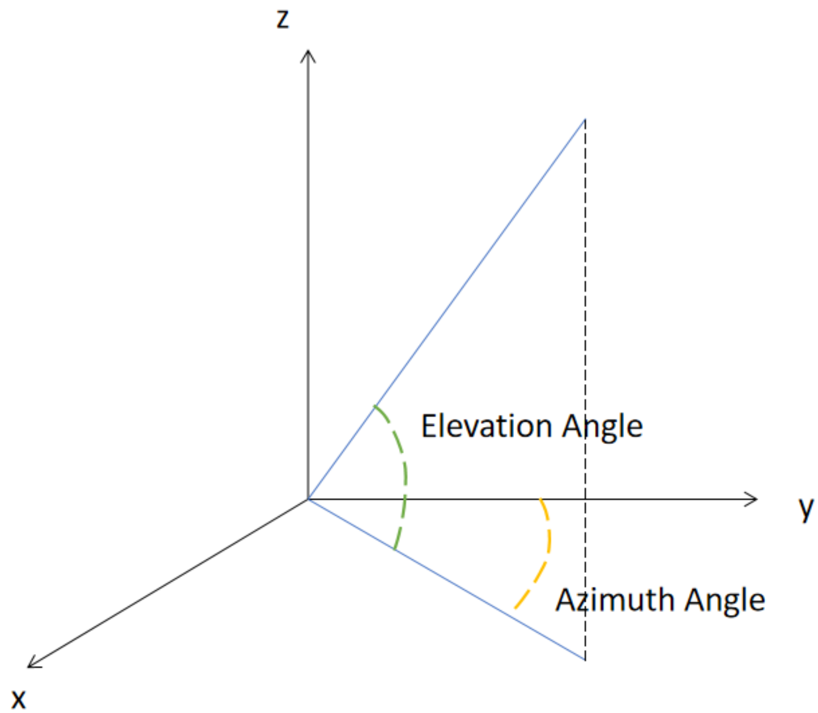
z
Elevation Angle
y
Azimuth Angle
x

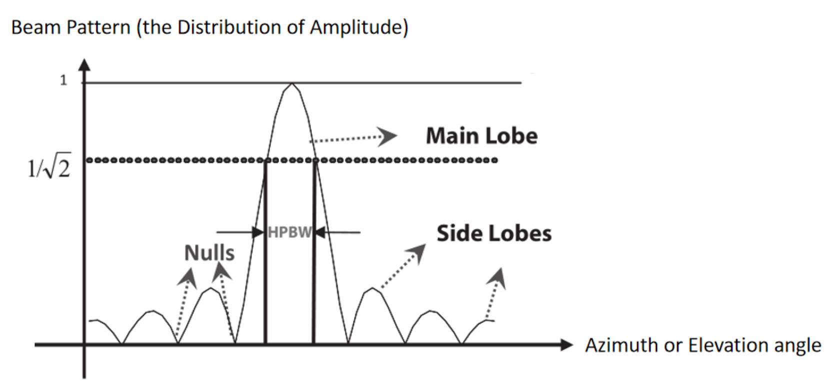
Beam Pattern (the Distribution of Amplitude)
1
$1/\sqrt{2}$
Main Lobe
HPBW
Side Lobes
Nulls
Azimuth or Elevation angle

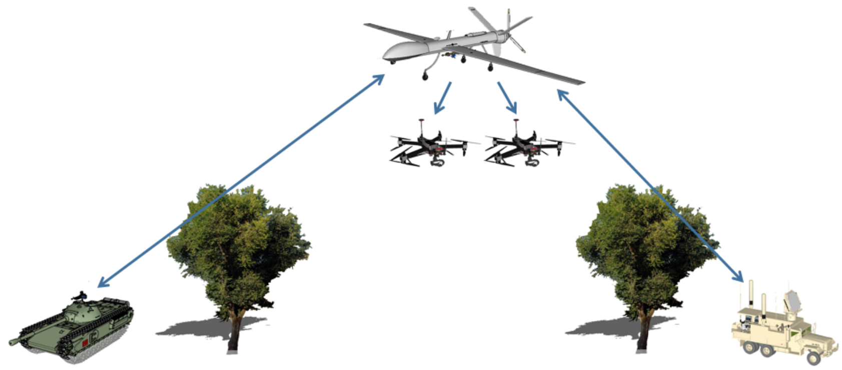

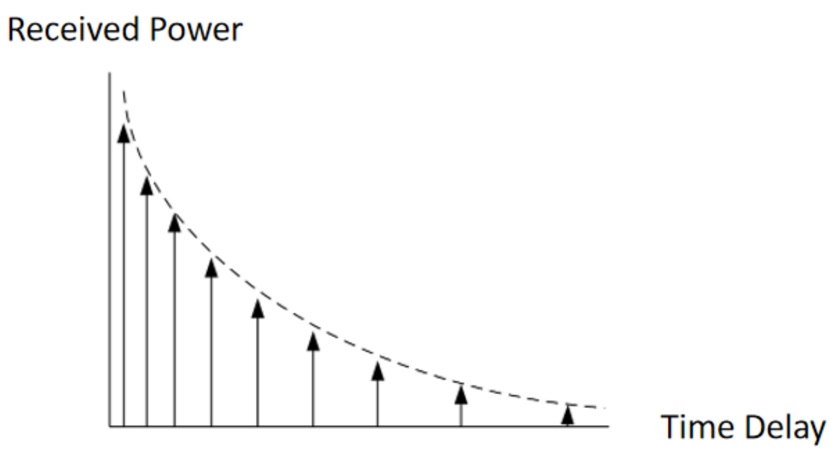
Received Power
Time Delay

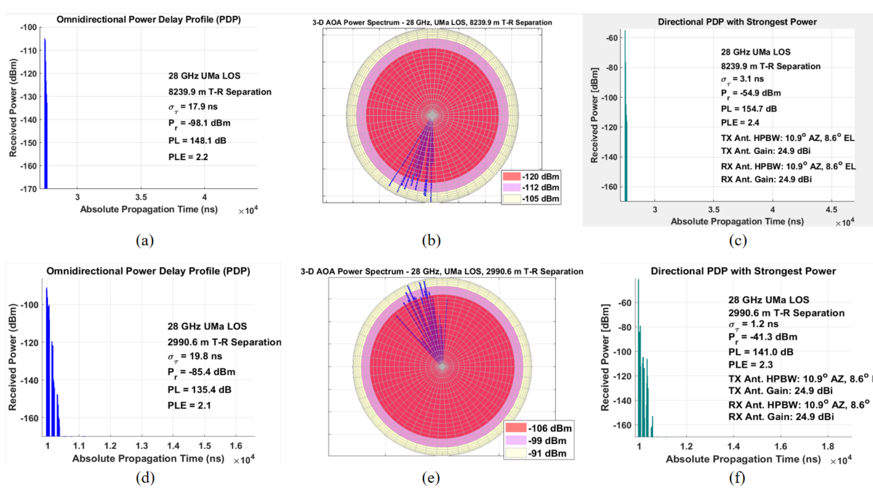
Omnidirectional Power Delay Profile (PDP)
28 GHz UMa LOS
8239.9 m T-R Separation
σ_τ = 17.9 ns
P_r = -98.1 dBm
PL = 148.1 dB
PLE = 2.2
Received Power (dBm)
Absolute Propagation Time (ns)
3-D AOA Power Spectrum - 28 GHz, UMa LOS, 8239.9 m T-R Separation
-120 dBm
-112 dBm
-105 dBm
Directional PDP with Strongest Power
28 GHz UMa LOS
8239.9 m T-R Separation
σ_τ = 3.1 ns
P_r = -54.9 dBm
PL = 154.7 dB
PLE = 2.4
TX Ant. HPBW: 10.9° AZ, 8.6° EL
TX Ant. Gain: 24.9 dBi
RX Ant. HPBW: 10.9° AZ, 8.6° EL
RX Ant. Gain: 24.9 dBi
Received Power [dBm]
Absolute Propagation Time (ns)
Omnidirectional Power Delay Profile (PDP)
28 GHz UMa LOS
2990.6 m T-R Separation
σ_τ = 19.8 ns
P_r = -85.4 dBm
PL = 135.4 dB
PLE = 2.1
Received Power (dBm)
Absolute Propagation Time (ns)
3-D AOA Power Spectrum - 28 GHz, UMa LOS, 2990.6 m T-R Separation
-106 dBm
-99 dBm
-91 dBm
Directional PDP with Strongest Power
28 GHz UMa LOS
2990.6 m T-R Separation
σ_τ = 1.2 ns
P_r = -41.3 dBm
PL = 141.0 dB
PLE = 2.3
TX Ant. HPBW: 10.9° AZ, 8.6° E
TX Ant. Gain: 24.9 dBi
RX Ant. HPBW: 10.9° AZ, 8.6° E
RX Ant. Gain: 24.9 dBi
Received Power [dBm]
Absolute Propagation Time (ns)

(a) (b) (c)

(d) (e) (f)

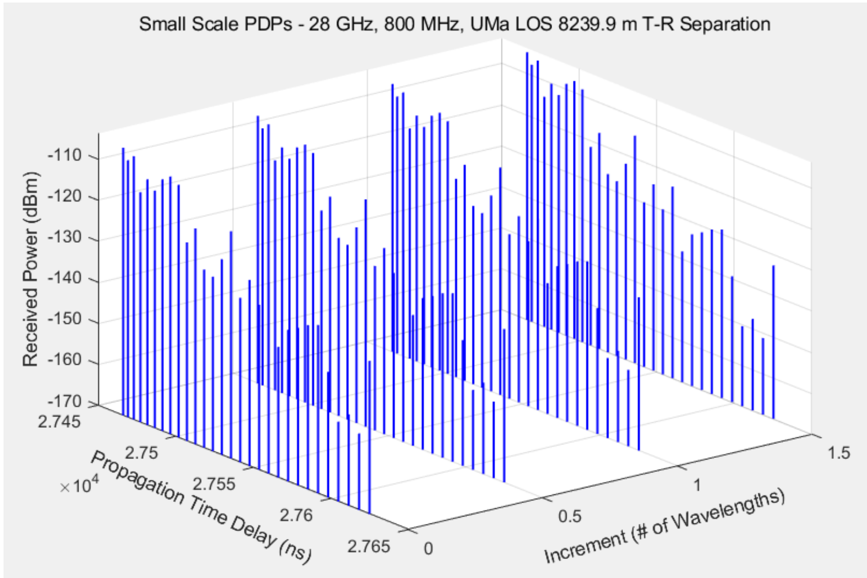
Small Scale PDPs - 28 GHz, 800 MHz, UMa LOS 8239.9 m T-R Separation
Received Power (dBm)
Propagation Time Delay (ns)
×10^4
Increment (# of Wavelengths)

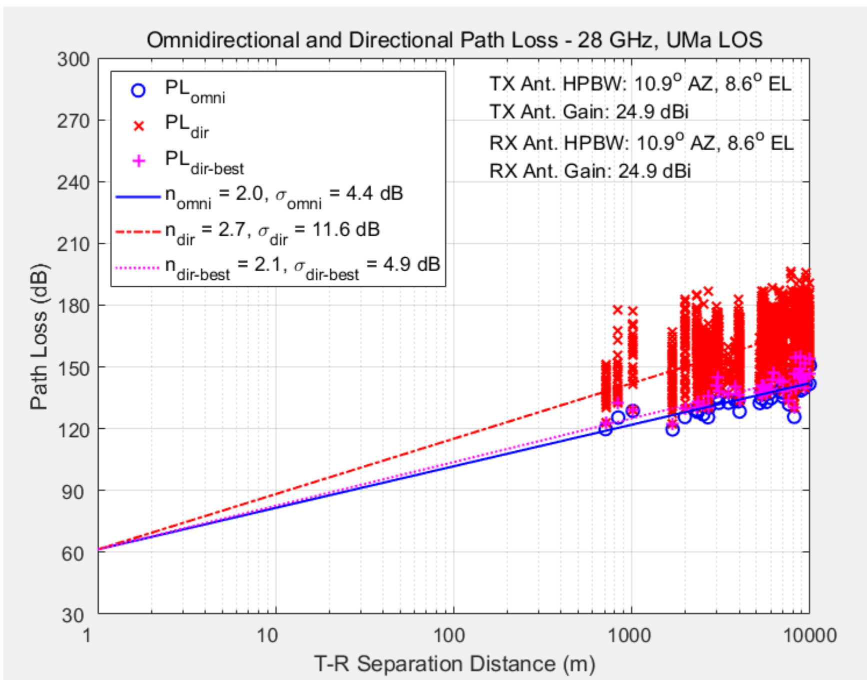
Omnidirectional and Directional Path Loss - 28 GHz, UMa LOS
PL_omni
PL_dir
PL_dir-best
n_omni = 2.0, σ_omni = 4.4 dB
n_dir = 2.7, σ_dir = 11.6 dB
n_dir-best = 2.1, σ_dir-best = 4.9 dB
TX Ant. HPBW: 10.9° AZ, 8.6° EL
TX Ant. Gain: 24.9 dBi
RX Ant. HPBW: 10.9° AZ, 8.6° EL
RX Ant. Gain: 24.9 dBi
Path Loss (dB)
T-R Separation Distance (m)

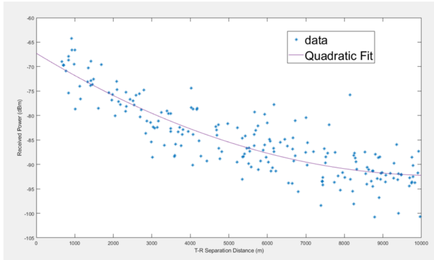
data
Quadratic Fit
Received Power (dBm)
T-R Separation Distance (m)

(a)

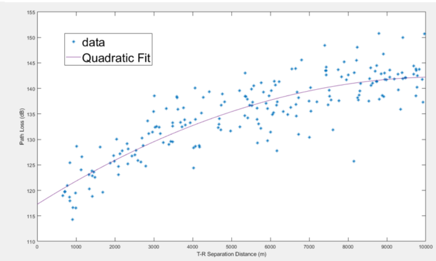
data
Quadratic Fit
Path Loss (dB)
T-R Separation Distance (m)

(b)

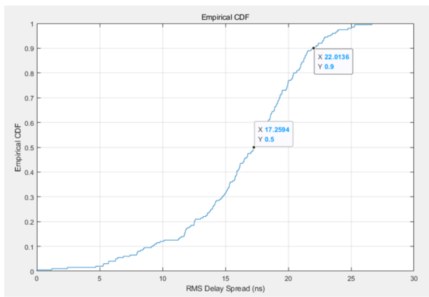
Empirical CDF
X 22.0136
Y 0.9
X 17.2594
Y 0.5
Empirical CDF
RMS Delay Spread (ns)

(a)

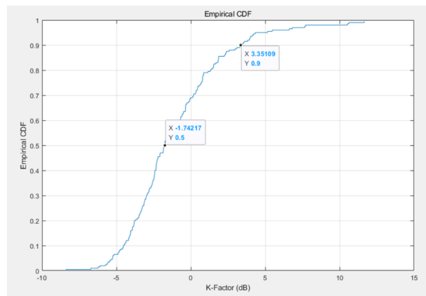
Empirical CDF
X 3.35109
Y 0.9
X -1.74217
Y 0.5
Empirical CDF
K-Factor (dB)

(b)

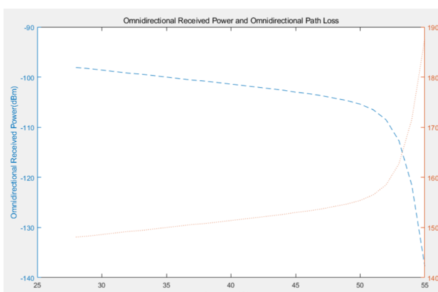
Omnidirectional Received Power and Omnidirectional Path Loss
Omnidirectional Received Power(dBm)
Omnidirectional Path Loss(dB)
frequency(GHz)

(a)

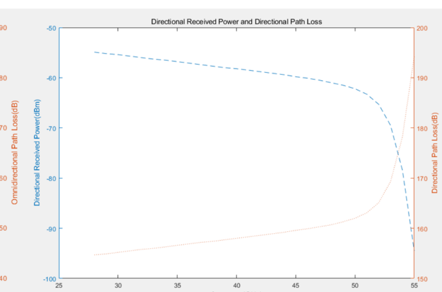
Directional Received Power and Directional Path Loss
Directional Received Power(dBm)
Directional Path Loss(dB)
frequency(GHz)

(b)

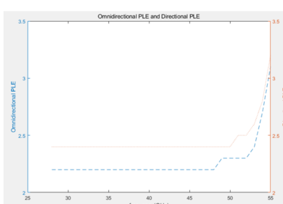
Omnidirectional PLE and Directional PLE
Omnidirectional PLE
Directional PLE
frequency(GHz)

(a)

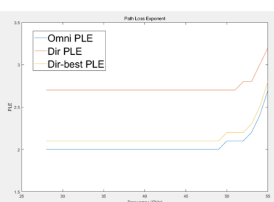
Path Loss Exponent
Omni PLE
Dir PLE
Dir-best PLE

(b)

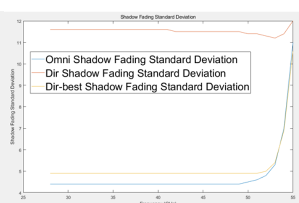
Shadow Fading Standard Deviation
Omni Shadow Fading Standard Deviation
Dir Shadow Fading Standard Deviation
Dir-best Shadow Fading Standard Deviation

(c)

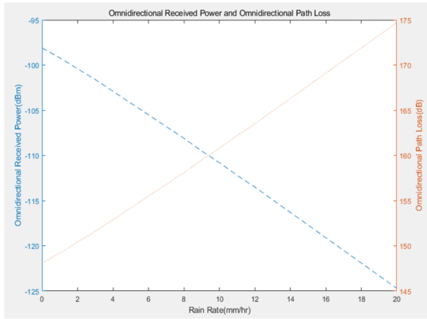
Omnidirectional Received Power and Omnidirectional Path Loss
Omnidirectional Received Power(dBm)
Omnidirectional Path Loss(dB)
Rain Rate(mm/hr)

(a)

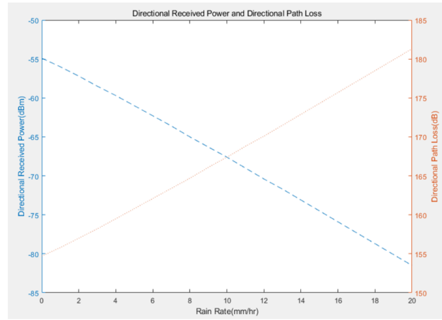
Directional Received Power and Directional Path Loss
Directional Received Power(dBm)
Directional Path Loss(dB)
Rain Rate(mm/hr)

(b)

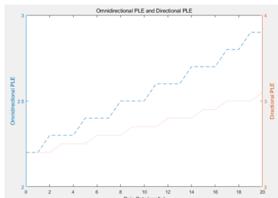
Omnidirectional PLE and Directional PLE
Omnidirectional PLE
Directional PLE
Rain Rate(mm/hr)

(a)

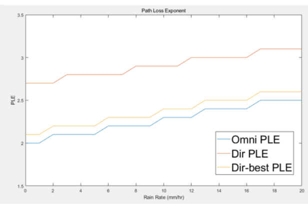
Path Loss Exponent
PLE
Rain Rate (mm/hr)
Omni PLE
Dir PLE
Dir-best PLE

(b)

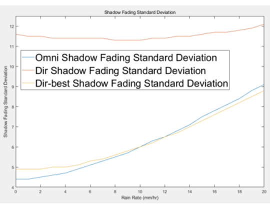
Shadow Fading Standard Deviation
Omni Shadow Fading Standard Deviation
Dir Shadow Fading Standard Deviation
Dir-best Shadow Fading Standard Deviation
Rain Rate (mm/hr)

(c)

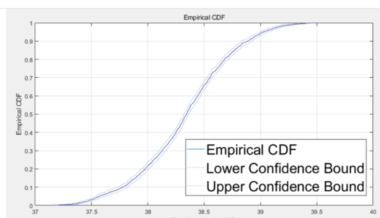
Empirical CDF
Empirical CDF
Empirical CDF
Lower Confidence Bound
Upper Confidence Bound
Condition Number (dB)

(a)

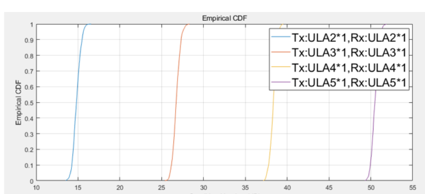
Empirical CDF
Empirical CDF
Tx:ULA2*1,Rx:ULA2*1
Tx:ULA3*1,Rx:ULA3*1
Tx:ULA4*1,Rx:ULA4*1
Tx:ULA5*1,Rx:ULA5*1
Condition Number (dB)

(b)

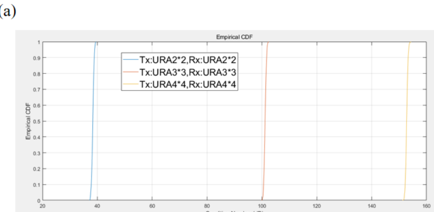
Empirical CDF
Empirical CDF
Tx:URA2*2,Rx:URA2*2
Tx:URA3*3,Rx:URA3*3
Tx:URA4*4,Rx:URA4*4
Condition Number (dB)

(c)

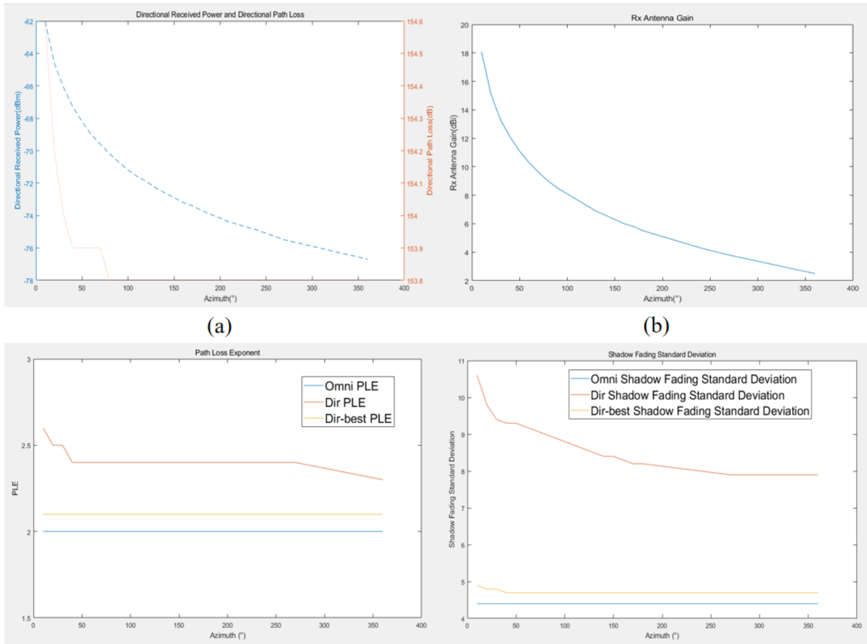
Directional Received Power and Directional Path Loss
Directional Received Power(dBm)
Directional Path Loss(dB)
Azimuth(°)
Rx Antenna Gain
Rx Antenna Gain(dB)
Azimuth(°)
Path Loss Exponent
Omni PLE
Dir PLE
Dir-best PLE
PLE
Azimuth (°)
Shadow Fading Standard Deviation
Omni Shadow Fading Standard Deviation
Dir Shadow Fading Standard Deviation
Dir-best Shadow Fading Standard Deviation
Azimuth (°)

(a) (b)

(c) (d)

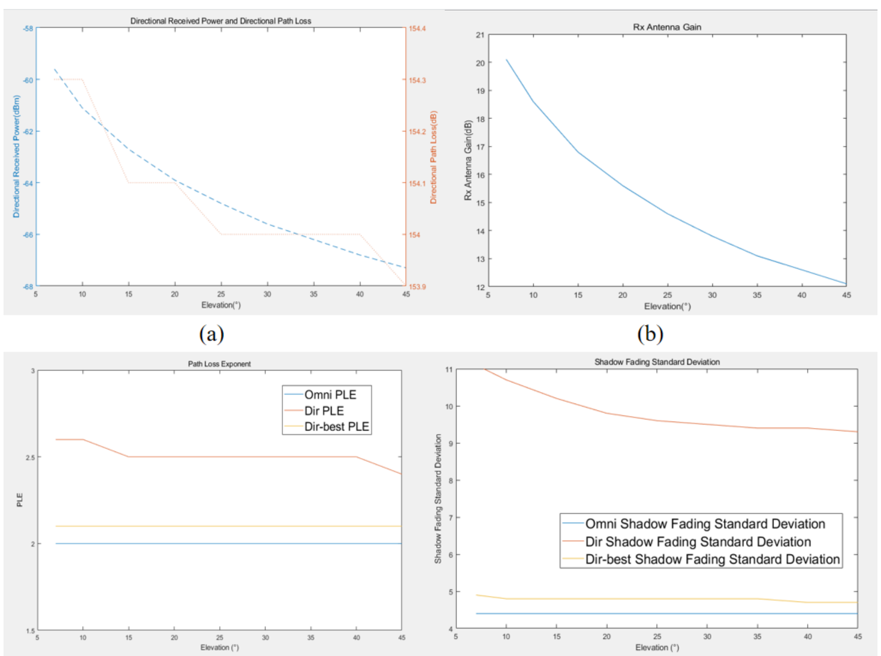
Directional Received Power and Directional Path Loss
Directional Received Power(dBm)
Directional Path Loss(dB)
Elevation(°)
Rx Antenna Gain
Rx Antenna Gain(dB)
Elevation(°)
Path Loss Exponent
Omni PLE
Dir PLE
Dir-best PLE
PLE
Elevation (°)
Shadow Fading Standard Deviation
Omni Shadow Fading Standard Deviation
Dir Shadow Fading Standard Deviation
Dir-best Shadow Fading Standard Deviation
Elevation (°)

(a) (b)

(c) (d)

Millimeter Wave Spatial Statistical Channel Model for High-altitude Military UAV Battlefield Situation Awareness

Jinsheng Yang[1], Huan Xi[1], and Zhou Pan[2]

[1]School of Microelectronics, Tianjin University,Tianjin 300072, China

[2]Tianjin Navigation Instrument Research Institute, Tianjin, China

Corresponding author: Zhou Pan(panli_an@163.com)

Key Points:

- A high-altitude military UAV air-to-ground scenario model is established for the battlefield scenario without base station
- The MIMO antenna array technology and the spatial statistical channel model of battlefield situation awareness scenario is constructed
- The simulation results can provide a theoretical basis for future high-altitude military UAV frequency selection and antenna design

Abstract

A high-altitude military UAV air-to-ground scenario model is established for the battlefield scenario without base station, the MIMO antenna array technology is used to improve the channel communication performance, and the spatial statistical channel model (SSCM) of this scenario is constructed in this paper. According to the simulation results, the dependence of the channel on T-R separation distance, frequency, rain rate and antenna HPBW parameters was investigated, the large-scale fading and small-scale fading characteristics was analyzed. By calculating and analyzing the condition number and rank of the channel transmission matrix, the spatial multiplexing under different MIMO antenna arrays was investigated. The simulation results can provide a theoretical basis for future high-altitude military UAV battlefield situation awareness frequency selection and antenna design.

1 Introduction

With the continuous advancement of global informatization process, the Fifth-Generation (5G) wireless communication technology has developed rapidly and been continuously applied. As shown in Figure 1, all kinds of UAVs have become an important component and effective supplement to realize the 6G air-space-ground-sea integrated communication system (Xiao et al., 2022), and have become an important part of building SAGIN (space-air-ground integrated network) (Bai et al., 2021). Full-spectrum resources will be further exploited, such as sub-6GHz, millimeter wave (mmWave), terahertz, and optical bands (You et al., 2020). Among them, millimeter wave bands provide new facilities for 5G mobile communication networks, as do broadband wireless communication links, to meet the growing demand for higher data rates (Al-Shammari et al., 2021).

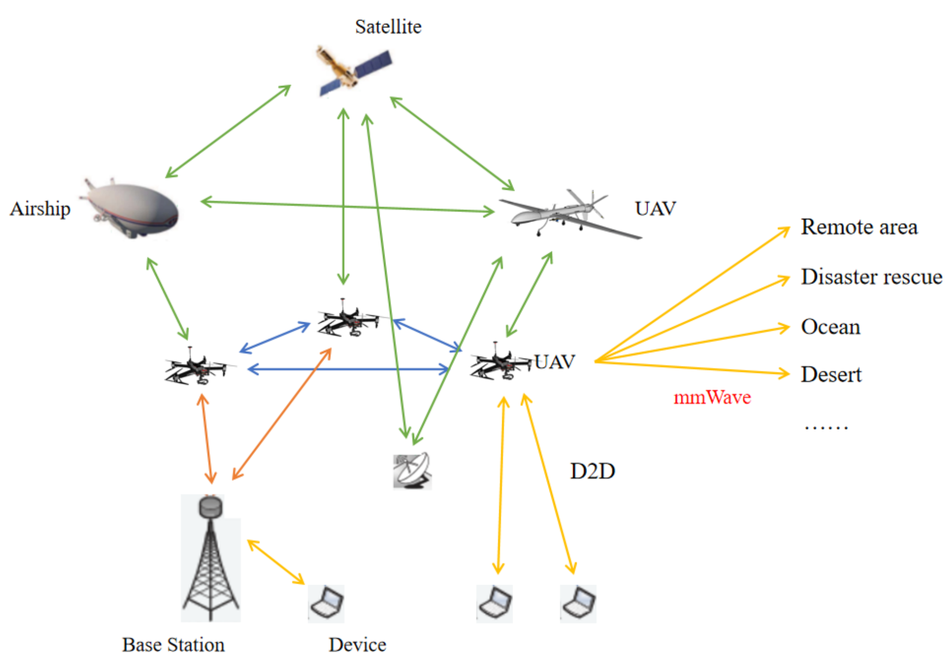

Figure 1. Millimeter-wave band UAV application scenarios.

The modern battlefield environment represented by the electromagnetic environment has become more and more prominent in its extensiveness, foundation, pillar, and commonality between the enemy and ourselves. In the military field, UAVs, as a new type of combat unit relying on electromagnetic signals, can be widely used in war zones, spies, combat aircraft, attack and missile launches, border surveillance, etc. (Bajracharya et al., 2022). Compared with manned aircraft, the use of UAVs can save costs to a greater extent, but it will also bring a series of problems such as UAV control and communication. Since base stations are vulnerable to jamming and destruction in battlefield scenarios, the use of high-altitude military UAVs for battlefield situation awareness through electromagnetic environment and electromagnetic actions is an effective means of response.

Battlefield support from UAVs is inseparable from fortified battles and street battles in modern cities. Among them, micro/small UAVs play a key role. However, UAVs that use millimeter wave bands for communication at close range are prone to signal interference, while military reconnaissance and combat integrated UAVs are usually at a higher altitude and far from the target. It can deal with enemy omnidirectional jammers with insufficient power when the enemy cannot determine its own position effectively. Meanwhile, it can carry out electromagnetic perception, take the lead on the battlefield, and form an optimal battlefield electromagnetic situation. Battlefield situation awareness through electromagnetism is an important and fundamental part of Electromagnetic Battle Management (EMBM), through which single or multiple combat operations can be closed-loop and efficient coordination. More importantly, military UAVs can enhance Line-of-sight (LOS) wireless channels (Zhang, Wang, & Poor, 2022; Li et al., 2020) and have clear advantages in terms of link budget and latency compared to multi-hop communication (Tozer et al., 2000). The targets in the battlefield situation awareness scenario are scattered in the complex natural and electromagnetic environment including complex terrain, sea conditions, meteorological conditions, ground clutter, sea clutter and various passive/active anthropogenic disturbances (Yang, Song, Xu et al., 2022), as shown in Figure 2. In the battlefield, the communication function of the base station may be stopped due to interference, and the reconnaissance and combat integrated UAV flying at high altitude directly communicates information with the ground target for UAV control and battlefield situation awareness. This type of reconnaissance and combat integrated UAV needs to have a wider reconnaissance range, so its flight altitude is higher than that of civilian UAVs. For example, the maximum flight altitude of the US MQ-9 UAV can reach 12,192 meters. China's CH-5 UAV cruises at an altitude of about 15,000 meters and a combat altitude of about 8,000 meters. Therefore, the use of UAVs for battlefield situation awareness will be more extensive, and its air-to-ground channel characteristics are of great significance in military scenarios.

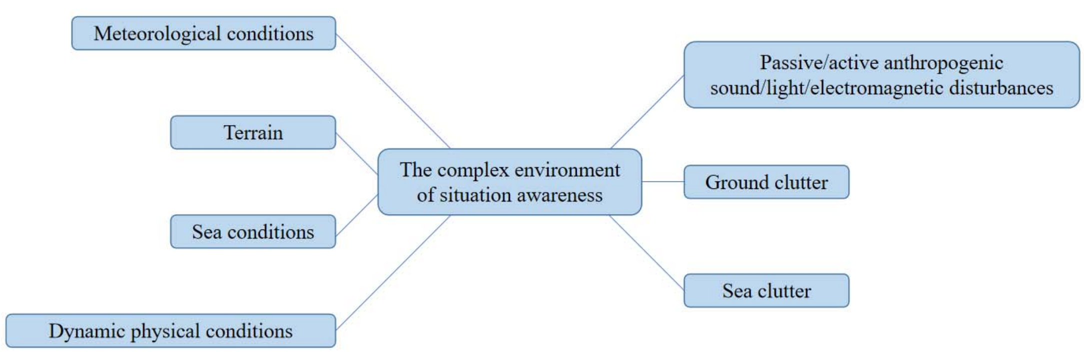

Figure 2. The complex environment of situation awareness.

Meanwhile, long-distance communication means that millimeter waves face high losses during propagation, which usually need to be solved by using highly directional antennas or using antenna arrays (Xiao et al., 2022; Bian et al., 2021; Wang et al., 2021). In the battlefield scene without base station, the highly directional antenna is not suitable for the task of finding targets in high-altitude military UAVs. From the point of view of UAV control, omnidirectional antennas have better communication performance during movement, while directional antennas perform poorly during movement (Khawaja et al, 2019), so the use of MIMO antenna arrays can better meet the needs of battlefield situation awareness. MIMO antenna arrays can improve channel reliability and channel capacity (Liao et al., 2020), and multiple antennas in a MIMO system can be utilized in different ways effectively. The most common of these are spatial multiplexing (SM) and beamforming (BF) (Sun et al., 2014).

In more scenarios as mentioned, high-altitude military UAVs and low-altitude UAVs can work together on the battlefield, and micro/small UAV swarms are usually used at low altitudes for close target strikes. It has obvious advantages such as indestructibility, low cost, and function distribution in complex battlefield environments with powerful electronic jamming and anti-aircraft firepower, which involves non-terrestrial networks (NTN) communication problems (Zhu, 2020). In the 3GPP specification, it is proposed that NTN can perform high-capacity transmission in millimeter wave, which requires huge bandwidth and can achieve high-speed connection through high-directional antennas (Traspadini et al., 2022). Therefore, after receiving electromagnetic signals, military UAVs can transmit electromagnetic signals to UAV swarms to complete efficient cooperative operations (Bajracharya et al., 2022; Zhang, Zhu, & Poor, 2022a). Meanwhile, high-altitude UAVs have greater coverage and smaller path loss than low-altitude UAVs compared to high-altitude platforms.

In recent years, the channel modeling researches of millimeter wave and MIMO antenna arrays mainly focus on indoor short-range communication scenarios, outdoor device-to-device (D2D) communication scenarios and low-altitude civil UAV-to-ground communication scenarios. The research on the application of ray tracing method to assist indoor positioning in millimeter band map was analyzed in reference (Kanhere et al., 2019). Satellite-to-UAV MIMO communication channel for LOS scenarios at terahertz frequencies was analyzed in reference (Geraci et al., 2022). Model of the communication channel of the UAV with the offshore unit at sub-6GHz was analyzed in reference (Liu, Wang, Chang et al., 2021; Wang et al., 2020). V2V channel model for mmWave MIMO channels was analyzed in reference (Bian et al., 2021; Huang et al., 2020). The above research results provide a theoretical basis and feasibility support for mmWave MIMO channels. A linear relationship between rain rate and attenuation for Ku/C band is presented in reference (Tian & Shi, 2020).

At present, in the study of UAV air-to-ground channel, an UAV trajectory tracking control with base station Non-line-of-sight (NLOS) scene was analyzed in reference (Zhang, Zhu, & Poor, 2022b), the Offload problem of UAV as an edge server in the construction of Internet of Vehicles was analyzed in reference (Liu, Liu, Qu et al., 2021), the three-dimensional nonstationary model based on geometry and the GBSM channel model to investigate low-altitude UAV ground channel modeling were analyzed in reference (Chang et al., 2021; Liu et al., 2019), a shaded double scattering channel to investigate the dynamic propagation conditions of LOS scene was analyzed in reference (Bithas et al., 2020).

In terms of battlefield situation awareness, the evolution trend of battlefield situation awareness of unmanned platforms was summarized in reference (Yang, Yang, Zhang et al., 2021), a new kind of vehicle-mounted battlefield perception system design and implementation scheme is presented in reference (Gao et al., 2021). The signal propagation loss model proposed by ITUR P.1546 is applied and implemented in reference (Shen et al., 2017). The ITU-R P.1546 model is a ground-based service node-to-surface prediction method suitable for the prediction range of 30 MHz to 3000 MHz frequency. It is suitable for effective transmission of tropospheric radio circuits on land, sea and/or land-sea hybrid paths with a small antenna height of 3000 m and a path length of 1 to 1000 km, and has wide applicability.

The above research results focus more on millimeter-wave ground equipment communication, indoor communication or low-altitude UAV (below 150 meters) ground communication, and lack the research on air-to-ground channel characteristics of high-altitude military UAV in the scenario of no base station. At present, the studies supports the feasibility of MIMO antenna array modeling of millimeter wave of UAVs, but lacks channel modeling for long-distance communication application scenarios.

In order to fill this gap, this paper uses the spatial statistical channel model modeling method to establish the air-to-ground communication channel of high-altitude military UAV, and simulates the scenario of receiving control signals and conducting electromagnetic situation perception in the case of base station failure in the battlefield, and gets a large amount of statistics through simulation. The channel parameters such as AOA power spectrum, AOD power spectrum, omnidirectional and directional received power, path loss, small-scale power delay spectrum, rms delay spread, Rice K-factor, path loss index, shadow fading standard deviation and other channel parameters were statistically analyzed to comprehensively characterize the channel characteristics. The analysis results provide a reference for the battlefield situation awareness communication link design of high-altitude military UAVs in the future, and supplement the communication of high-altitude UAVs in the air-space-ground-sea integration under the 6G framework effectively. The main research contents of this paper are as follows:

- In this paper, a high-altitude military UAV air-to-ground scenario model is established for the battlefield scenario without base station, and a MIMO antenna array is used to improve the channel communication performance, and the spatial statistical channel model of this scenario is constructed. The channel was simulated to get statistics, the dependence of the channel on T-R distance, frequency, rain rate, antenna HPBW parameters, and conduct large-scale fading and small-scale fading statistical analysis was investigated to get channel characteristics.
- According to the statistics derived by simulation, the spatial multiplexing of channels in the air-to-ground scenario of high-altitude military UAVs in the air-to-ground scene of high-altitude military UAVs under different MIMO antenna arrays is investigated by calculating and analyzing the condition number and rank of the channel transmission matrix.

The remainder of this study is organized as follows. Section 2 introduces the relevant theoretical basis, including channel fading model parameters, MIMO antenna array technology, beamforming and half-power-beamwidth (HPBW). Section 3 models the high-altitude military UAV air-to-ground communication channel without base station, characterizes modeling scenarios, and analyzes the channel fading characteristics. Section 4 introduces the configuration of various simulation parameters, and analyzes the simulation results of the channel model parameters. Section 5 provides a conclusion.

2 Relevant Theoretical Basis

2.1 Channel Fading Model Parameters

In addition to direct radiation, radio waves encounter an obstacle, according to their own wavelength and the relative size of the obstacle to reflect, diffract, scatter, which will have a certain loss of radio wave energy, resulting in signal fading. According to the interval of the field strength change of the received signal, radio waves can be divided into large-scale fading and small-scale fading. The size of the interval here means the relationship between the distance we observe the movement of the mobile station and the wavelength of the signal itself. The classification of wireless fading channels can be summarized in the Figure 3.

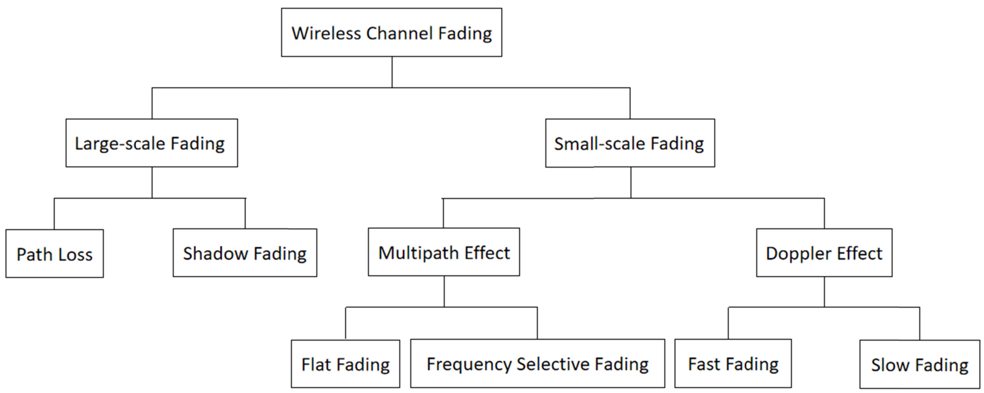

Figure 3. Wireless channel fading classification.

According to Figure 2, the characteristics of large-scale fading are described by path loss and shadow fading. Large-scale average path loss measures the average fading of the signal between the transmitter and receiver, defined as the difference between the effective transmit power and the average received power. Shadow fading refers to the formation of a shadow area behind the obstruction due to the obstruction of obstacles such as terrain undulations or tall building groups when radio signals are transmitted in channels at mesoscale distances, resulting in random changes in the average power of the received signal. Its fading characteristics approximately follow a lognormal distribution (Rappaport, 1996).

Small-scale fading refers to the rapid change in amplitude, phase, or multipath delay of a radio signal after a short time or distance (several wavelengths). This fading is caused by the same transmission signal traveling along different paths, and the signals arriving at the receiver at different moments (or phases) are superimposed on each other. The signals that arrive at these different paths are called multipath signals, and multipath signals include direct paths and multiple path signals such as reflection, diffraction and scattering generated by the presence of scatterers. Small-scale channel modeling mainly considers the modeling of time dispersion parameters, frequency dispersion parameters and spatial dispersion parameters (Chetlur & Dhillon, 2017).

The type of small-scale fading depends on the characteristics of the transmitted signal (signal bandwidth and symbol period) and channel characteristics (delay spread and Doppler spread). The relationship between signal parameters and channel parameters determines that different transmitted signals will undergo different fading characteristics. According to the delay spread of the channel, the channel can be divided into flat fading channel and frequency selective fading channel. According to the Doppler expansion of the channel, the channel can be divided into fast fading channel and slow fading channel.

In the actual scene propagation process, the signal will experience both large-scale fading and small-scale fading, large-scale fading generally affects the network coverage ability of the wireless system, and small-scale fading affects the communication quality of the communication system (Khuwaja et al., 2018).

For UAV air-to-ground channel analysis, this paper performs channel modeling for the simulation measurement of path loss, received power, shadow fading, AOA angle, AOD angle, RMS delay spread, antenna gain, pass loss exponent and other parameters. The symbols and descriptions of each parameter are shown in Table 1.

Table 1. The Symbols and Descriptions of Channel Parameters

Parameter	Symbol	Description
T-R Separation Distance (m)	d_{T-R}	The separation distance from the transmitter to the receiver.
Time Delay (absolute propagation time) (ns)	τ	The time it takes for an electromagnetic or optical signal to travel a certain distance in the transmission medium.
RMS Delay Spread (ns)	σ_τ	Standard deviation of power delay distribution, the most commonly used temporal dispersion parameter.
Received Power (dBm)	P_r	The power RX received.
Path Loss (dB)	PL	The loss caused by the propagation of radio waves in space. It is caused by the radiated diffusion of the transmitted power and the propagation characteristics of the channel.
Path Loss Exponent	$n, n_{omni}, n_{dir}, n_{dir-best}$	The path loss exponent ranges from 2 to 6, with 2 representing free space and 6 representing severe obstruction.
Shadow Fading Standard Deviation (dB)	$\sigma, \sigma_{omni}, \sigma_{dir}, \sigma_{dir-best}$	Obstacles attenuate signal power by absorption, reflection, scattering and

		diffraction, causing shadow fading. The range is from 5dB to 12dB, and the typical value is 8dB.
Rician K-factor	K	An important parameter to characterize the degree of channel fading, and has an important impact on link budget, transmit diversity power allocation, and adaptive receiver design.
TX Ant. HPBW	AZ_{TX}, EL_{TX}	An editable parameter denoting the azimuth/elevation half-power-beamwidth (HPBW) of the TX antenna (array) in degrees.
TX Ant. Gain (dBi)	G_{TX}	TX antenna gain.
RX Ant. HPBW	AZ_{RX}, EL_{RX}	An editable parameter denoting the azimuth/elevation half-power-beamwidth (HPBW) of the RX antenna (array) in degrees.
RX Ant. Gain (dBi)	G_{RX}	RX antenna gain.

In the lower corner mark of n and σ, ‘omni’ represents omnidirectional, ‘dir’ represents directional, ‘dir − best’ represents the direction with the strongest received power.

In the table above, the omnidirectional received power can be described as

$$P_r = \sum_{i,j} \sum_{k,m} P_r(AZ_{TX,i}, EL_{TX,j}, AZ_{RX,k}, EL_{RX,m})(d_{T-R}) \quad (1)$$

Where i, j, k, m denotes unique pointing directions indices in azimuth and elevation at the TX and RX, respectively. $AZ_{TX,i}, EL_{TX,j}, AZ_{RX,k}, EL_{RX,m}$ represents the TX azimuth and elevation angles, and the RX azimuth and elevation angles, respectively (Mou et al., 2019).

Path loss can be described as

$$PL(dB) = FSPL(dB) + 10nlog_{10}(d/d_0) + AT(dB) + X_\sigma \quad (2)$$

Where FSPL implies free space path loss, AT is related to the attenuation factor, X_σ is a zero-mean Gaussian random variable with a standard deviation σ in dB, d_0 signifies the free space reference distance (Teixeira et al., 2021).

According to the Friis transmission equation, free space path loss can be described as

$$FSPL(dB) = \left(\frac{4\pi d_{T-R}}{\lambda}\right)^2 = \left(\frac{4\pi d_{T-R} f}{c}\right)^2 = -32.44 - 20lg(d_{T-R}) - 20lgf \tag{3}$$

Where c represents the electromagnetic wave propagation speed (approximate speed of light). The unit of d_{T-R} is km, the unit of f is MHz (Jawhly & Chandra, 2021).

From another point of view, the directional path loss is equal to the transmit power plus the TX and RX antenna gains, minus the directional received power (Sun et al., 2017), it can be written as

$$PL = P_{TX} + G_{TX} + G_{RX} - P_r \tag{4}$$

In addition, the relationship between time delay and T-R separation distance can be described as

$$\tau = \frac{d_{T-R}}{c} \tag{5}$$

The time delay of the direct path is T-R separation distance divided by the electromagnetic wave propagation speed. In the presence of multipath components, the multipath component has a slightly larger time delay than the direct path.

Power Delay Profile (PDP) describes the dispersion of a channel over time, which is the expectation of received power at a certain delay. It is calculated by averaging the channel impulse response CIR (Channel Impulse Response) in the time domain and squaring it (Yang, Li, & Xu, 2021; Yang, & Yuan, 2022).

The parameters used to describe time expansion are mean excess delay, RMS delay spread and X dB, which are all related to PDP.

Mean excess delay is the first moment of PDP. It is defined as

$$\overline{\tau} = \frac{\sum_{n=1}^{N} \tau_n p_n}{\sum_{n=1}^{N} p_n} \tag{6}$$

Where p_n is the n^{th} multipath power, τ_n is the n^{th} extra delay.

RMS Delay Spread is an important latency domain parameter used to quantify the dispersion effect caused by radio waves propagating in the delay domain due to the sensitivity of the communication system, and describes the delay statistics of the multipath effect of the channel, as shown in Equation 7,

$$\sigma_\tau = \sqrt{\frac{\sum_{n=1}^{N} \tau_n^2 p_n}{\sum_{n=1}^{N} p_n} - \left(\frac{\sum_{n=1}^{N} \tau_n p_n}{\sum_{n=1}^{N} p_n}\right)^2} \tag{7}$$

The Rician K-factor can reflect the effect of direct paths and multipath components on the channel, defined as the ratio of the principal signal power (the strongest) to the variance of the multipath components, as shown in Equation 8,

$$K(dB) = 10log_{10}\left(\frac{P_{strongest}}{\sum P_{remaining}}\right) \tag{8}$$

2.2 MIMO Antenna Array Techology

MIMO technology can exponentially increase the capacity and spectrum utilization of communication systems without increasing bandwidth, and more importantly, improve long-distance communication performance, which is suitable for the channel requirements of the scenarios investigated in this paper.

In the arrangement of MIMO antennas, there are usually four common ways of ULA (uniform linear array), URA (uniform rectangular array), UCA (uniform circular array), CCA (cylindrical conformal array) (Xiao et al., 2022; Wang et al., 2021). This paper uses ULA and URA arrangement to simulate and measure channel characteristics, and further describes the channel characteristics in the form of HPBW azimuth and elevation.

As shown in Figure 4, according to the number of antennas, it can be divided into four types: SISO, SIMO, MISO and MIMO. Adding antennas on the transceiver can provide multiplexing ideally.

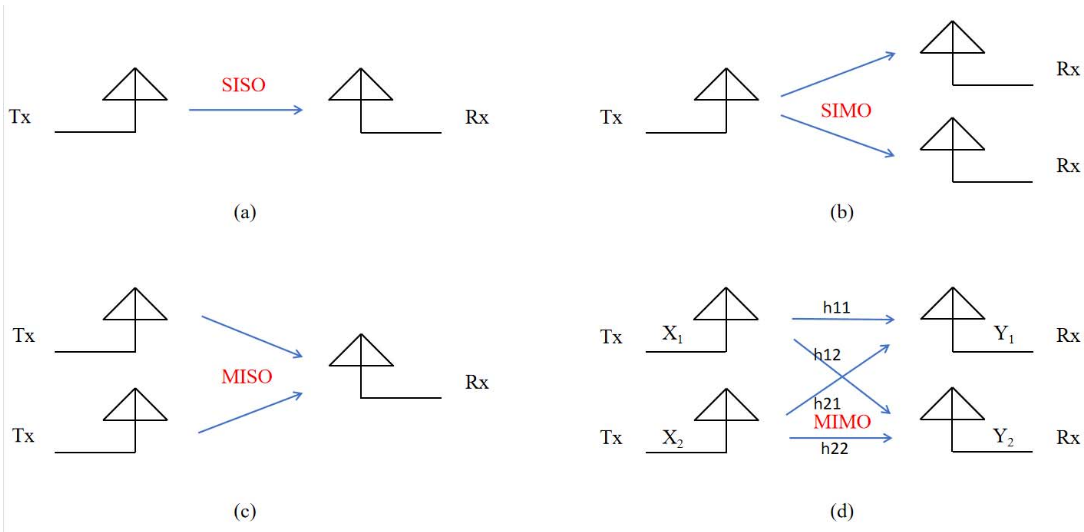

Figure 4. Four types of transmission divided by the number of receivers and transmitters, (**a**) SISO; (**b**) SIMO; (**c**) MISO; (**d**) MIMO.

Space division multiplexing is a method that uses multiple antennas to multiplex different transmission paths in space to send multiple copies of different data in parallel to increase capacity. Figure 4(d) shows a 2×2 MIMO channel formed by two antennas on both transceiver and receiver, and four transmission paths can be established ideally, reaching 4 times the capacity of SISO. However, in reality, due to the same fading and interference of multiple paths, due to spatial correlation, it may not be possible to transmit different signals in multiple ways, resulting in poor spatial multiplexing effect.

In Figure 4(d), the transmitter data is recorded as $\mathrm{X}_1, \mathrm{X}_2$, the receiver data is recorded as $\mathrm{Y}_1, \mathrm{Y}_2$, in order to judge the independence of the transmission path, the transmission channel matrix H is established as

$$H = \begin{bmatrix} h_{11} & h_{21} \\ h_{12} & h_{22} \end{bmatrix} \tag{9}$$

So there is

$$\begin{bmatrix} Y_1 \\ Y_2 \end{bmatrix} = \begin{bmatrix} h_{11} & h_{21} \\ h_{12} & h_{22} \end{bmatrix} \begin{bmatrix} X_1 \\ X_2 \end{bmatrix} \tag{10}$$

When referring to output Y, input X is pre-encoded, the above equation can be varied to

$$\begin{bmatrix} Y_1^{'} \\ Y_2^{'} \end{bmatrix} = \begin{bmatrix} \lambda_1 & 0 \\ 0 & \lambda_2 \end{bmatrix} \begin{bmatrix} X_1^{'} \\ X_2^{'} \end{bmatrix} \tag{11}$$

λ_1 and λ_2 are transfer coefficients. If neither is 0, the matrix rank is 2, which means that the system has two relatively independent spatial channels and can send and receive two data channels at the same time; If one of them is 0, the matrix rank is 1, which means that the transmission space of this 2×2 MIMO system is very correlated, and it has degenerated from MIMO to SISO or SIMO, and can only send and receive data at the same time. To determine its channel capacity, its condition number was determined as

$$Condition\ Number = \frac{\lambda_1}{\lambda_2} \tag{12}$$

When the condition number is 1, the transmission coefficients of the two channels are equal and the channel independence is high. When the condition number is greater than 1, the transmission quality of the two channels is different, the capacity of this 2×2 MIMO system is between 1 and 2 times that of the SISO system.

Orthogonal Frequency Division Multiplexing (OFDM) is a specific implementation of multi-carrier modulation (MCM), which utilizes MCM to reduce the transmission rate, increase the symbol period, effectively reduce and eliminate the influence of inter-symbol interference and frequency-selective weakening, increasing the utilization of the spectrum and improving the performance of systems (Jia et al., 2020).

Take ULAs at both the transmitter and receiver for example, the equation for generating such a channel coefficient is

$$h_{m,k}(f) = \sum_p \alpha_{m,k,p} e^{j\Phi_{m,k,p}} e^{-j2\pi\tau_{m,k,p}} e^{-j2\pi d_T m sin(\phi_{m,k,p})} e^{-j2\pi d_R k sin(\varphi_{m,k,p})} \tag{13}$$

$H_{m,k}(f)$ is expressed as the channel coefficient between the m^{th} transmitting antenna and the k^{th} receiving antenna when the subcarrier is f. p represents the p^{th} resolvable multipath component. α is the amplitude of the channel gain, Φ denotes the phase of the multipath component, τ represents the time delay , d_T and d_R are the antenna element spacing at the transmitter and receiver, respectively. ϕ and φ denote the azimuth angle of departure and angle of arrival, respectively. In a MIMO-OFDM system, each subcarrier f corresponds to a channel transmission matrix H with the product of the number of transmit antennas and the number of received antennas (Sun et al., 2017; Ji et al., 2022).

2.3 Beamforming and HPBW

The purpose of beamforming is to concentrate the energy radiated by the antenna. It can form specific beams and transmit data through the beams. Beamforming is mainly based on MIMO antenna arrays, and antenna beam patterns can be obtained by beamforming. Antenna beam pattern indicate that the power or amplitude of a signal changes with angle. Antenna beam pattern is generally a function of antenna shape, size, and frequency. The angles here are expressed in azimuth angle and elevation angle. These angles are shown in the Figure 5.

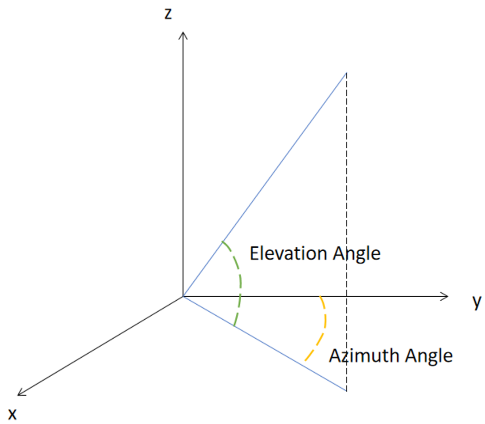

Figure 5. Azimuth Angle and Elevation Angle.

The beam pattern usually consists of a main lobe, some side lobes, and some nulls, as shown in Figure 6. The y-axis in the Figure 8 is the signal amplitude normalized to the maximum value of the main lobe. HPBW is a measure of beam width and is important for beamforming performance analysis. The half-power beamwidth of the main lobe on a given main section is an angular region in the direction of maximum radiation in which the relative radiated power of the antenna is greater than one-half. In this example, HPBW is the angular distance (azimuth angle or elevation angle) between two antenna pattern points, where the power becomes half of its maximum. HPBW can be found by drawing the line $y = \frac{1}{\sqrt{2}}$.

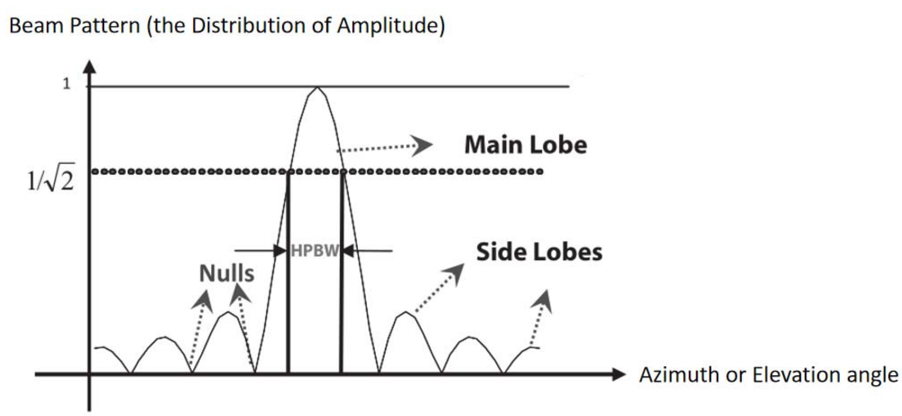

Figure 6. Antenna beam pattern.

3 Channel Scenario Model

In this application scenario, this paper builds a scene model as shown in Figure 7 , mainly investigates the air-to-ground communication mode of high-altitude military UAV in the open scene without base station, and considers the foliage loss caused by vegetation.

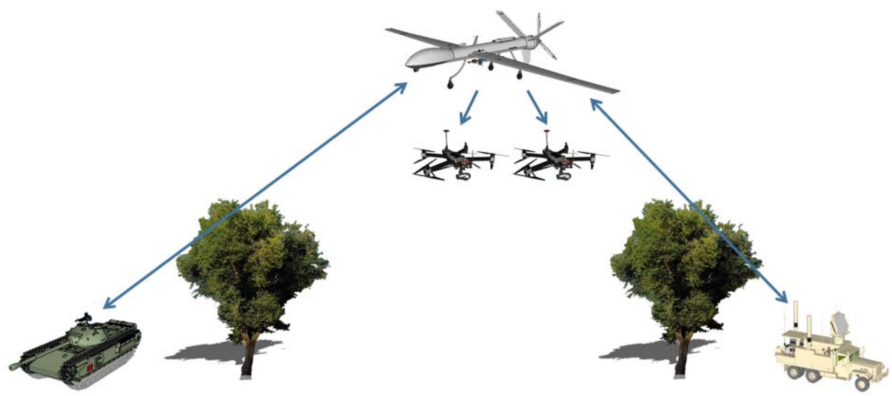

Figure 7. Air-to-ground simulation scenario of high-altitude military UAV, considering foliage loss.

3.1 Modeling Scenario Characterization

In the basic scene construction, this paper uses a free space propagation model, which is closer to the type in the battlefield situation. This is a common large-scale loss model, where the PLE (path loss exponent) parameter provides an insight into the path loss based on the environment, with a PLE value of 2 for free space and a PLE value of 4 for the asymptotic bidirectional ground reflection propagation model (Sun et al., 2017). The reference distance normalized to 1 meter makes it easy to compare measurements and models, provides a standard definition for PLE, while enabling intuitive and fast calculation of path losses. Compared with the existing alpha-beta-gamma (ABG) path loss model used in the 3GPP/ITU channel model, this model has better model parameter stability, better prediction performance over a wide range of microwave and millimeter wave frequencies, distances, and scenarios, and fewer parameters (Sun et al., 2017).

From the fading causes and the model constructed in this paper, this channel has both large-scale fading and small-scale fading, and the large-scale fading characteristics are more obvious. In order to solve the problem of high propagation loss, it is common to use a highly directional antenna or use an antenna array. When searching for targets, the problem of setting up highly directional antennas is difficult to solve, so the using of antenna arrays is a better choice. In the selection of MIMO antenna, since the reconnaissance and combat integrated UAV needs to have the function of cruising strike at the same time, the results of the omnidirectional channel model and the directional channel model should be considered. Military UAVs require highly directional antennas to ensure the huge bandwidth to reach such ultra-high data rates and meet massive wireless data traffic demands (Zhang et al., 2021). Meanwhile, the directional channel model is of great significance for the correct implementation of MIMO systems, so this paper further investigates the channel characteristics of the direction with the strongest energy received at the receiver.

3.2 Theoretical Analysis of Channel Fading Characteristics

In this section, the large-scale fading and small-scale fading characteristic parameters of the channel was analyzed through formulas, which provides a theoretical basis and analysis source for subsequent simulation work.

3.2.1 Large-scale Fading

According to Equation 3, the free space path loss can be calculated by T-R separation distance and the frequency. For example, when d_{T-R} is 8.2399 km, f is 28000 MHz, the theoretical value of FSPL will be -139.7 dB. According to Equation 4, if both the TX power and the antenna array are determined, the sum of the directional path loss and the received power will be a constant value.

Since in the actual transmission scenario, the factors that cause the random attenuation of the signal are generally unknown, so only statistical models can be used to characterize this random attenuation, the most commonly used model is the lognormal shadow fading model, which has been confirmed by measured data and can be used to model the change of received power in outdoor and indoor wireless propagation environments.

The lognormal shadow fading model assumes the ratio of transmit power (P_t) and received power (P_r) as a random variable with a lognormal distribution. Set the ratio to K_{tr}, it can be written as

$$K_{tr} = \frac{P_t}{P_r} \tag{14}$$

The lognormal distribution can be written as

$$p = \frac{\xi}{\sqrt{2\pi}\sigma K_{tr}} exp[-\frac{(10\log_{10} K_{tr} - PL)^2}{2\sigma^2}] \tag{15}$$

Where $\xi = \frac{10}{\ln 10}$. A large number of outdoor channel measurements show that the shadow fading standard deviation σ range from 4 dB to 13 dB.

3.2.2 Small-scale Fading

According to Equation 5, when d_{T-R} is 8239.9 m, the time delay of the directional path will be 2.749×104 ns. As described in Section 2.1, power delay profile describes the dispersion of a channel over time, which is the expectation of received power at a certain delay. It refers to the phenomenon of signal time diffusion due to multipath propagation. The reason for this is that the time it takes for the transmitted signal to travel through different paths to the receiving point varies.

The small-scale PDP generally follows an exponential distribution. The PDP distribution can be written as

$$P_\tau = \frac{1}{T} e^{-\frac{\tau}{T}} \quad 0 < \tau < \infty \tag{16}$$

Where T is the average of the multipath time delay. The theoretical correlation between time delay (or call it absolute propagation time) and received power can be can be represented by Figure 8.

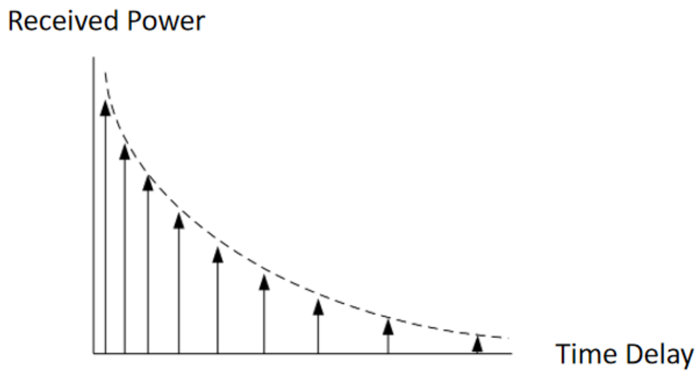

Figure 8. The theoretical Power Delay Profile.

Under the law of negative exponential, according to Equation 6 and 7, the mean excess delay and RMS delay spread can be derived as

$$\bar{\tau} = E(\tau) = \int_0^{\infty} \tau P(\tau) d\tau = T \tag{17}$$

and

$$\sigma_\tau = \sqrt{\int_0^{\infty} (\tau - \bar{\tau})^2 P(\tau) d\tau} = \sqrt{\int_0^{\infty} (\tau - T)^2 P(\tau) d\tau} = T \tag{18}$$

Both the mean excess delay ($\bar{\tau}$) and RMS delay spread (σ_τ) are equal to the average of the multipath time delay (T). In addition, the multipath delay is mainly distributed in the range of 0 to 2T.

4 Channel Characterization and Simulation Analysis

The current wireless channel modeling methods mainly include statistical modeling methods, deterministic modeling methods and semi-deterministic modeling methods. The statistical modeling method relies on channel measurement, summarizes the statistical characteristics and empirical formulas of channels through a large number of measured statistics, and extends to other scenarios with similar structures. Spatial statistical channel model is a common statistical channel model. SSCM has high prediction accuracy and fast processing speed in applicable environments, so it has become the preferred signal propagation loss model for real-time systems (Shen et al., 2017).

In this paper, some parameters are used as variables, such as T-R separation distance, frequency, rain rate, number of MIMO antennas, azimuth HPBWs and elevation HPBWs of RX antennas. Based on a large number of simulation statistics, the channel of the model is comprehensively characterized by using SSCM.

4.1 Simulation Parameter Configuration

In this paper, the channel parameters of high-altitude military UAVs are modeled by using the open-source software NYU Simulator (NYUSIM) for millimeter wave channel modeling. This is a simulation software for SSCM that uses OFDM modulation. Its latest version, V3.1, contains three important channel characteristics: spatial consistency, human blockage parameters, and outdoor-to-indoor (O2I) penetration loss. Meanwhile, it contains the calculation ability of path loss and shadow fading models and RMS delay propagation parameters, which can be well applied to the simulation of mmWave MIMO channels. For more information about NYUSIM, see reference (Sun et al., 2017) and https://wireless.engineering.nyu.edu/nyusim/.

Due to its lack of data analysis capabilities and partial visualization output, MATLAB is used to visualize the simulation statistics generated by its multiple runs for the investigate and analysis of channel characteristics.

Set the distance between transmitter TX and receiver RX to be in the range of 500 meters to 10,000 meters, corresponding to possible UAV and ground unit distances. The RF bandwidth is set to 800 MHz to meet the needs of military UAV use, the TX power is set to 50 dBm, the atmospheric pressure is 1013.25 mbar, the humidity is 50%, the temperature is 20°C, considering the foliage loss caused by vegetation, the total distance that the transmitted signal travels within foliage is set to 0.1 m, and the foliage attenuation is 0.4 dB/m.

4.2 T-R Separation Distance

At a frequency of 28 GHz, according to reference (Rappaport et al., 2013, 2015), set the HPBW of the MIMO antenna as a definite value. Set the azimuth and elevation HPBW of the antenna to 10.9◦ and 8.6◦ at both TX and RX, respectively. The antenna spacing is 0.5 times the wavelength, the polarization direction is Co-Pol(co-polarization), the rain rate is 0 mm/hr. Considering that the target is outdoors, ignore the O2I loss. Assume that the MIMO antennas are all URA 2×2 arrangement, forming a 4×4 MIMO antenna array. In this way, channel characteristics with T-R separation distances of 500 to 10,000 meters can be simulated.

Taking the T-R separation distance at 8239.9 meters and 2990.6 meters as an example, the omnidirectional power delay profile can be derived as shown in Figure 9(a) and 9(d). The X-axis is the absolute propagation time (ns), the Y-axis is the received power (dBm), each line in the figure represents a multipath component, and also corresponds to the multipath component of the arrival threshold shown in the 3-D AOA power spectrum in Figure 9(b) and 9(e), respectively. It can be seen that this channel has more multipath components, such as 29 at a distance of 8239.9 meters, 64 at a distance of 2990.6 meters, and the power the receiver received decreases exponentially with the increase of propagation time. This result ties well with the theoretical result in Section 3.2.2. Figure 9(c) and 9(f) shows the directional PDP with strongest power, which is based on omnidirectional PDP, derived from HPBW and antenna gain. Its multipath case is similar to omnidirectional, and its characteristics can be used to guide the design of directional antennas at specific altitudes.

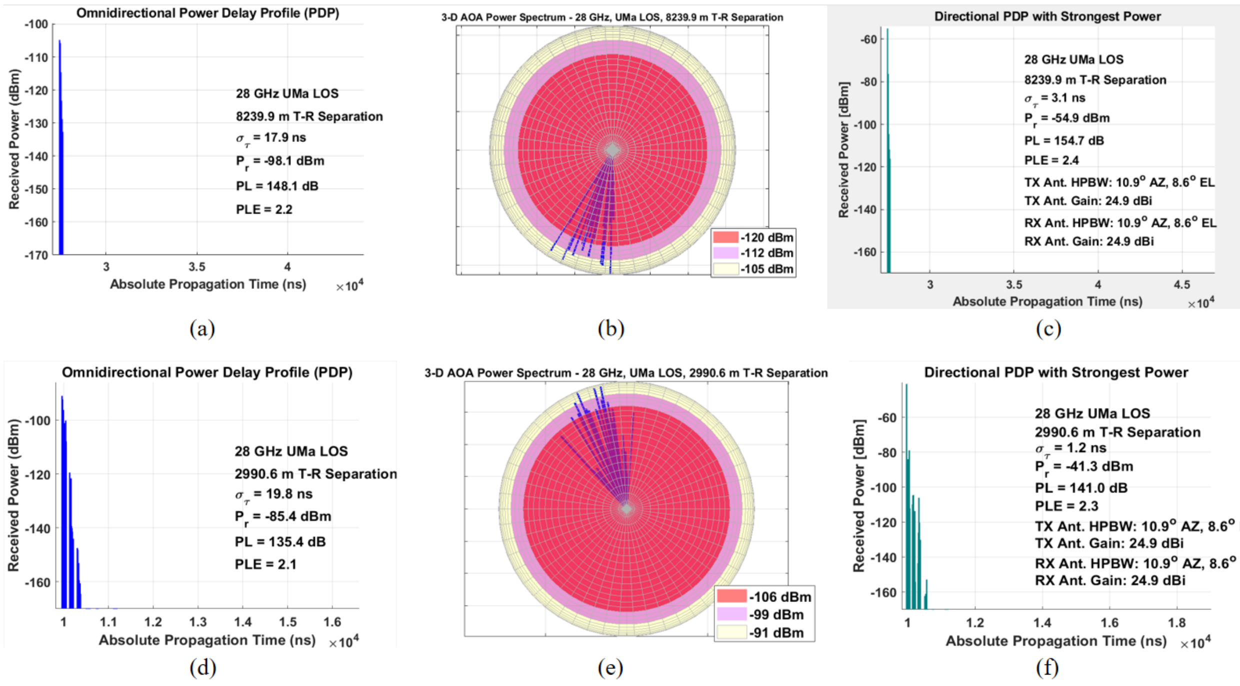

Figure 9. Omnidirectional power delay profile, 3-D AOA power spectrum, directional PDP with strongest power of 8239.9 m and 2990.6 m. (**a**) omnidirectional power delay profile, 8239.9 m; (**b**) 3-D AOA power spectrum, 8239.9 m; (**c**) directional PDP with strongest power, 8239.9 m; (**d**) omnidirectional power delay profile, 2990.6 m; (**e**) 3-D AOA power spectrum, 2990.6 m; (**f**) directional PDP with strongest power, 2990.6 m.

In addition, the small scale PDPs of each array of the receiving antenna under the model can be derived as shown in Figure 10, where the third dimension is the interval of the antenna in the antenna array. Figure 10 shows the PDP of the four antennas, and the PDP is basically the same, but there are some differences in delay. At a distance of 8239.9 meters, according to Section 3.2.2, the theoretical value of direct path delay in this scenario is about 2.749×104 ns.

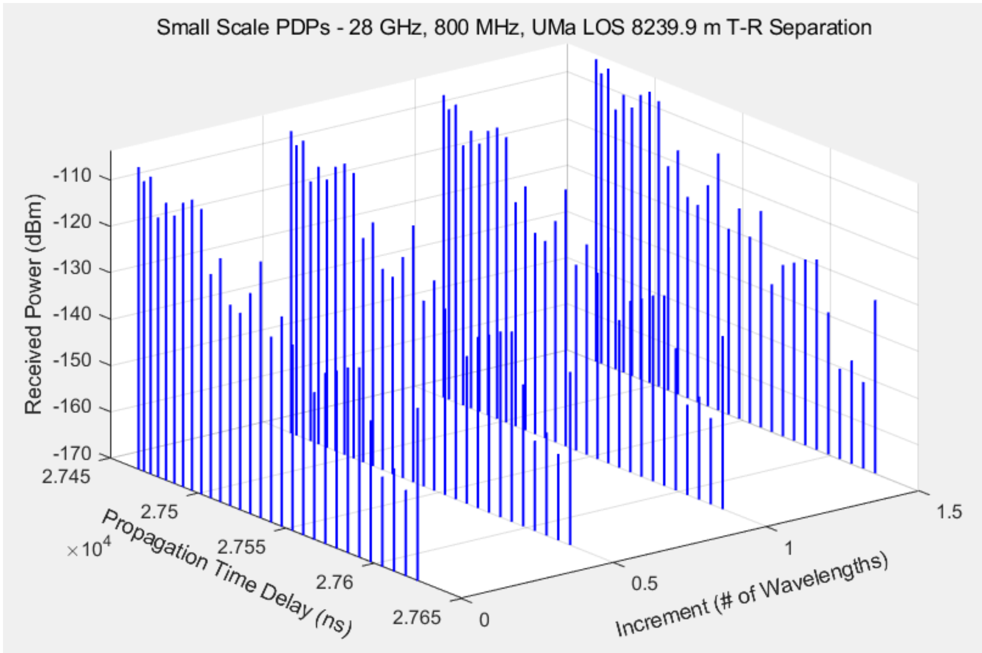

Figure 10. Small Scale PDPs of each array of the receiving antenna.

The total propagation delay is distributed from about 2.747×104 ns to 2.763×104 ns, and the smallest propagation delay component corresponds to the direct path. This result ties well with the theoretical value. In terms of trends, the decay situation is also the same as above. In addition, the omnidirectional and directional path loss value scatter plot and fitted plot line are generated by NYUSIM as shown in Figure 11. Due to the presence of multipath components, RX receives more multipath components and energy, and the directional path loss and PLE will always be greater than the omnidirectional path loss and PLE. PLE will reach 2.7 in this scenario.

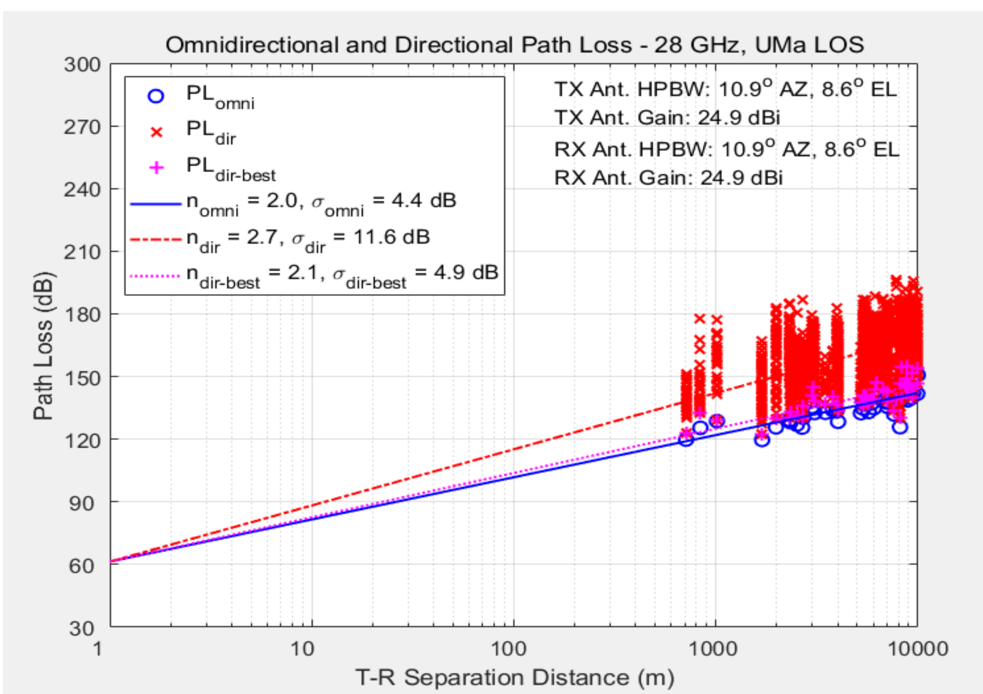

Figure 11. Scatterplots and fitted plot lines of path loss values generated by NYUSIM.

The omnidirectional received power and omnidirectional path loss at different distances are shown in Figure 12, and they are quadratically fitted, where R square is 0.7508 and the residual value is 53.37, which can get a relatively good fitting effect.

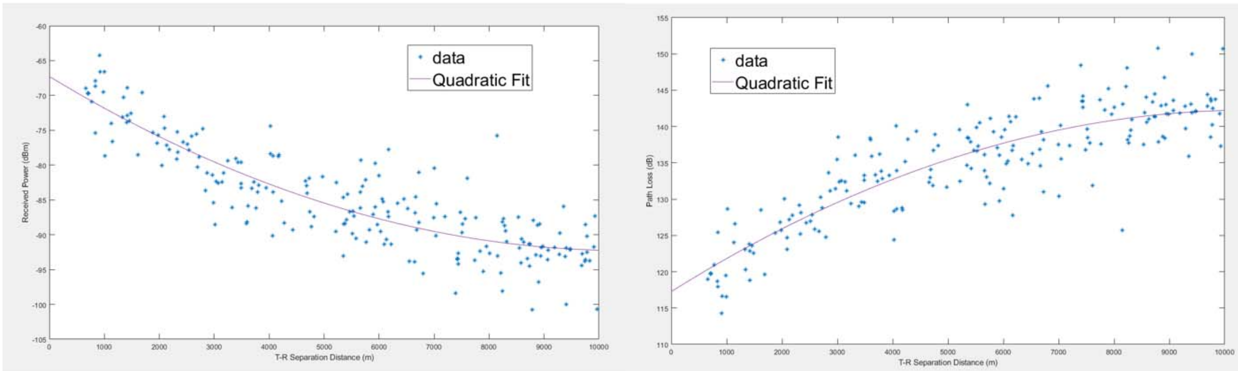

(a) (b)

Figure 12. The omnidirectional receiving power and omnidirectional path loss varies with distance.

The empirical cumulative distribution function (Empirical CDF) of the RMS delay spread derived from the simulation is shown in Figure 13(a). Its values are distributed from about 0 to 27 ns, of which 90% of the RMS delay spread value is less than 22 ns, and the median value is about 17.26 ns. It can be seen from the figure that the RMS delay spread is large due to the influence of high-altitude distance in this scenario. Moreover, the higher RMS delay spread part accounts for a relatively large part, which indicates that there is an obvious multipath effect other than the direct component in this channel, so it is necessary to pay attention to the small-scale fading of the channel.

The empirical cumulative distribution function of the omnidirectional Rician K-factor derived from the simulation is shown in Figure 13(b). Its values range from -8 to 12 dB, with 90% of the Rician K-factor values less than 3.35 dB and the median value being about -1.74 dB. The Rician K-factor value is small, which means that this channel can maintain a large channel capacity because it is not completely dominated by direct paths, and the multipath component has a large contribution. In addition, the simulation shows that the small-scale fading characteristics of the channel conform to the Gaussian distribution.

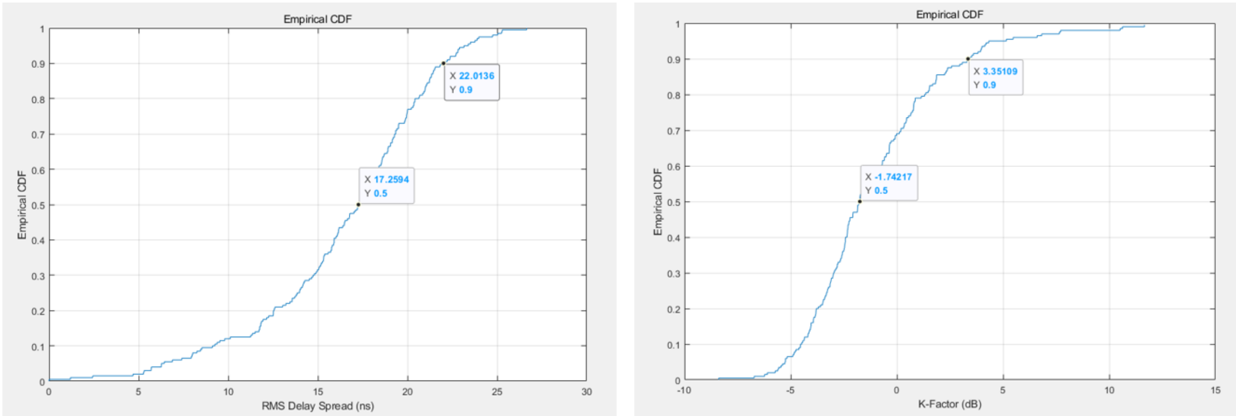

(a) (b)

Figure 13. The Empirical CDF of RMS Delay Spread (ns) and Rician K-factor (dB). (**a**) The Empirical CDF of RMS Delay Spread (ns); (**b**) The Empirical CDF of Rician K-factor (dB).

4.3 Frequency

From the point of view of UAV controlling, in order to prevent inter-signal interference, the frequency is selected from 28 GHz to 55 GHz. Considering the frequency dependence at the distance of 8239.9 m at the transmitter and receiver, it can be derived by simulation that the omnidirectional RMS delay spread is 17.9 ns, the directional RMS delay spread is 3.1 ns, and the antenna gain of both the transmitter and receiver is 24.9 dBi. Its omnidirectional received power and omnidirectional path loss are shown in Figure 14(a), and directional receive power and directional path loss are shown in Figure 14(b). It can be concluded that when the frequency is less than 50 GHz, the two curves are linear; when the frequency is greater than 50 GHz, the omnidirectional received power (dBm) decreases rapidly, and the omnidirectional path loss (dB) increases rapidly. Therefore, the frequency selection of high-altitude military UAVs should be as much as possible not greater than 50 GHz to maintain a linear relationship and avoid excessive channel fading.

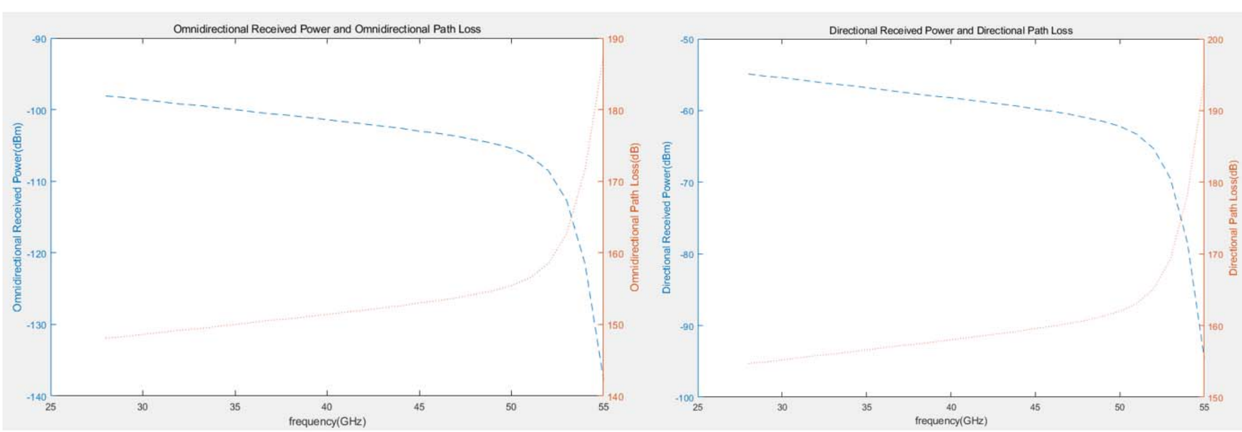

(a) (b)

Figure 14. Omnidirectional/Directional received power and path loss at 28 to 55 GHz, (**a**) omnidirectional; (**b**) directional.

At a distance of 8239.9 m, the frequency dependence of omnidirectional and directional PLE is shown in Figure 15(a), which can ensure good PLE stability below about 49 GHz. The omnidirectional PLE is about 2.2 and the directional PLE is about 2.4 in this range.

By fitting at a distance of 500 to 10,000 meters, considering the path loss exponent and the shadow fading standard deviation, the curve is derived as shown in Figure 15(b) and 15(c). It can be seen that in the research of high-altitude UAV-to-ground channels, frequencies below about 49GHz can ensure better channel stability, and the loss above 52 GHz will be significantly improved.

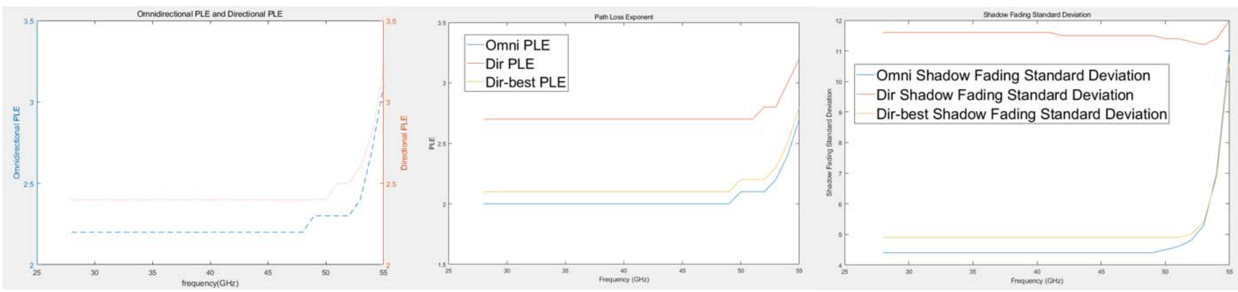

(a) (b) (c)

Figure 15. PLE and shadow fading standard deviation varies with frequency, (**a**) omnidirectional and directional PLE at 28 to 55 GHz of 8239.9 m; (**b**) PLE at 28 to 55 GHz of 500 m to 10000 m; (**c**) shadow fading standard deviation at 28 to 55 GHz of 500 m to 10000 m.

4.4 Rain Rate

The passage of radio waves through the rain area will produce attenuation, and when the frequency of the radio wave is higher, the wavelength will be shorter. High-band microwaves such as Ku and Ka with frequencies above 10 GHz have a wavelength of only 10 to 30 millimeters, similar to raindrops with a diameter of several millimeters, and the polarization angle of electromagnetic waves is also changed by rainfall.

Assuming that at the 28 GHz frequency, other simulation parameters are the same as Section 4.1 and 4.2, and the rain rate is between 0 and 20 mm/hr. According to Figure 16, at 8239.9 m, the omnidirectional receiving power (dBm) decreases linearly, the omnidirectional path loss (dB) increases linearly, and the directional received power and path loss also have the same change characteristics.

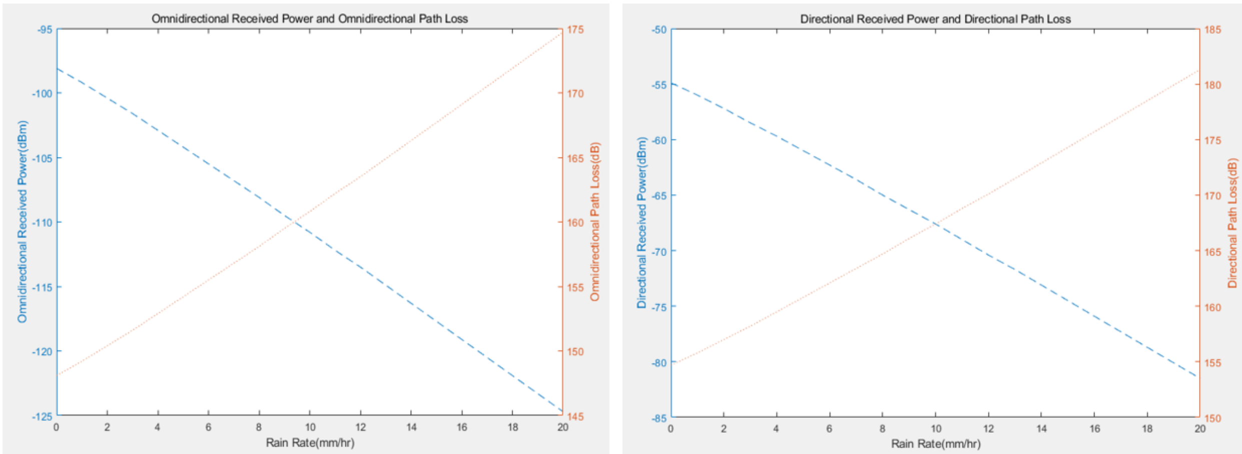

(a) (b)

Figure 16. Omnidirectional/Directional received power and path loss at 0 to 20 mm/hr.

According to Figure 17(a), rain rate has a greater impact on the PLE of high-altitude to ground channel, so the impact of current rain rate cannot be ignored in the battlefield scenario. By fitting at a distance of 500 to 10,000 meters, considering the path loss exponent and the shadow fading standard deviation, the curve is derived as shown in Figure 17(b) and 17(c). Therefore, in the rainfall scenario, it is necessary to appropriately reduce the signal frequency or increase the number of system antennas to ensure that the path loss exponent and shadow fading standard deviation are not too high, the channel capacity should be increased.

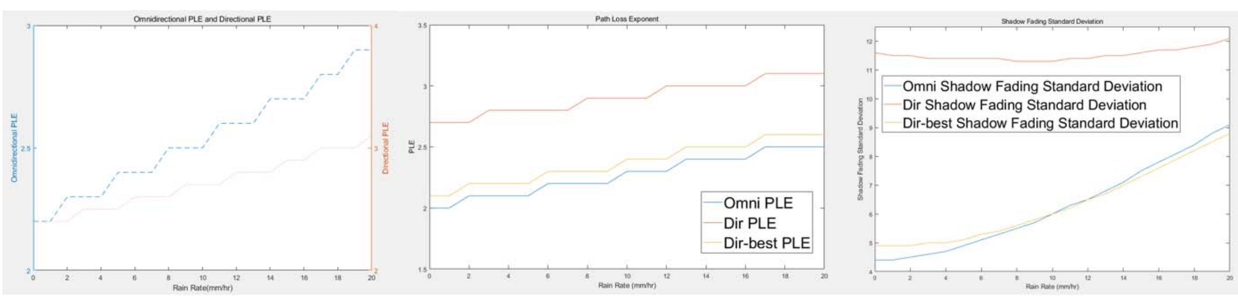

(a) (b) (c)

Figure 17. PLE and shadow fading standard deviation varies with rain rate. (a) omnidirectional and directional PLE at 0 to 20 mm/hr of 8239.9 m; (b) PLE at 0 to 20 mm/hr of 500 m to 10000 m; (c) shadow fading standard deviation at 0 to 20 mm/hr of 500 m to 10000 m.

4.5 MIMO Antennas

According to Section 2.2, the condition number of the MIMO channel and the rank of the channel transmission matrix can be investigated to judge its spatial multiplexing application. Taking a 4×4 MIMO channel with both receiver and transmitter antenna numbers of URA 2×2 as an example, an empirical CDF plot of the channel condition number and its 95% confidence bound can be derived, as shown in Figure 18(a). Similarly, the MIMO channels of 9×9 and 16×16 are modeled, and the condition number empirical CDFs are derived as shown in Figure 18(b). The MIMO channels of 2×2, 3×3, 4×4, and 5×5 are modeled, and the empirical CDFs with the condition number are derived as shown in Figure 18(c). The rank distributions of each channel transmission matrix under each main simulation condition are shown in Table 2.

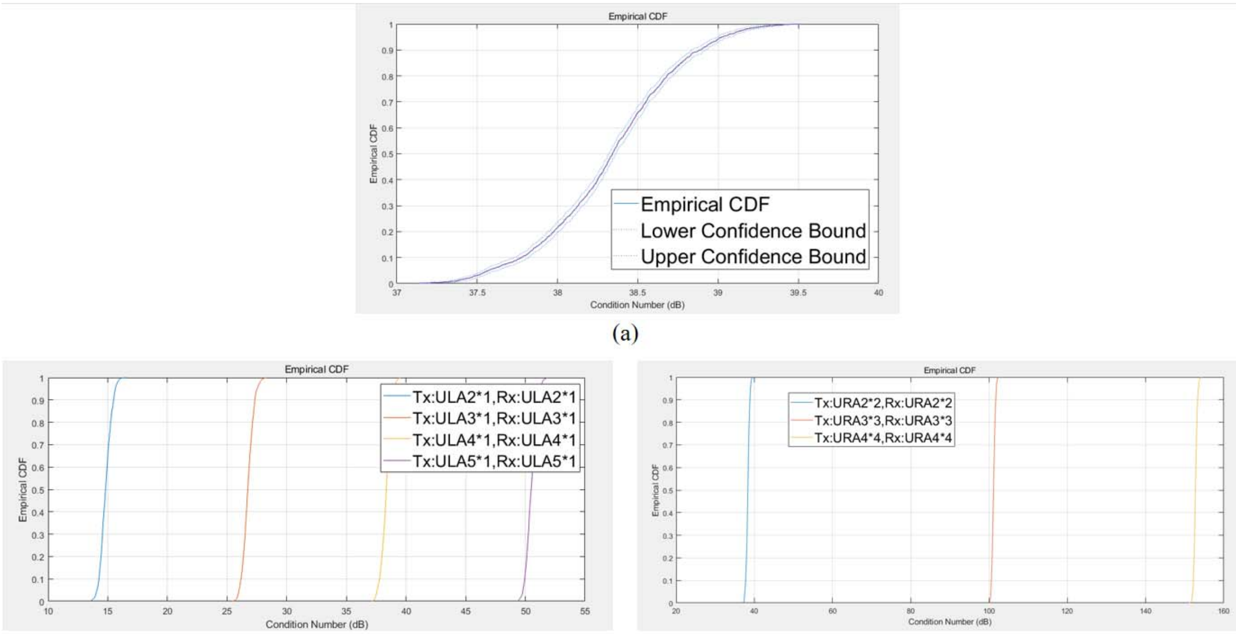

(a)

(b) (c)

Figure 18. The Empirical CDF of Condition Number, (**a**) 4×4 MIMO; (**b**) 4×4, 9×9, 16×16 MIMO; (**c**) 2×2, 3×3, 4×4, 5×5 MIMO.

Table 2. The Rank Distribution of Channel Transmission Matrix

MIMO	Rank=1	Rank=2	Rank=3	Rank=4	Rank=5	Rank=6	Rank=7	Rank=8	Rank=9
2×2	1805	78245							
3×3	1612	19348	59090						
4×4	1602	7813	37286	33349					
5×5	1601	4118	29789	33105	11437				
9×9	1601	30	9768	21291	16556	20386	7529	1311	1578

As can be seen from the Figure 18 and the Table 2, for MIMO channels below 9×9, each antenna is added to the transmitter and receiver, and the condition number is increased by about 12dB. In the 2×2 MIMO channel, 97.7% of the channel transmission matrix is in the full-rank condition, which can realize the spatial multiplexing of two channels. In the 3×3 MIMO channel, 73.8% of the channel transmission matrix is in the full-rank condition, which can realize the spatial multiplexing of three channels. In contrast, the proportion of full rank in MIMO channels decreases as the number of antennas increases, and there is not even a full rank situation in MIMO channels of 16x16 (the maximum rank is 15). This provides a basis for selecting the number of antennas in the case of multiplexing.

4.6 HPBW Simulation

Suppose there is a signal transmitter at 50 dBm power, azimuth HPBW 10°, elevation HPBW 10°, and other relevant parameter settings are the same as Section 4.1 and 4.2.

Figure 19 shows the effects of the azimuth of the receiving antenna on directional received power and path loss, receiver antenna gain, path loss exponent and shadow fading standard deviation, respectively. Figure 20 shows the effects of the elevation of the receiving antenna on directional received power and path loss, receiver antenna gain, path loss exponent and shadow fading standard deviation, respectively. This provides a basis for the HPBW design of directional antennas in the air-to-ground channel of high-altitude military UAVs.

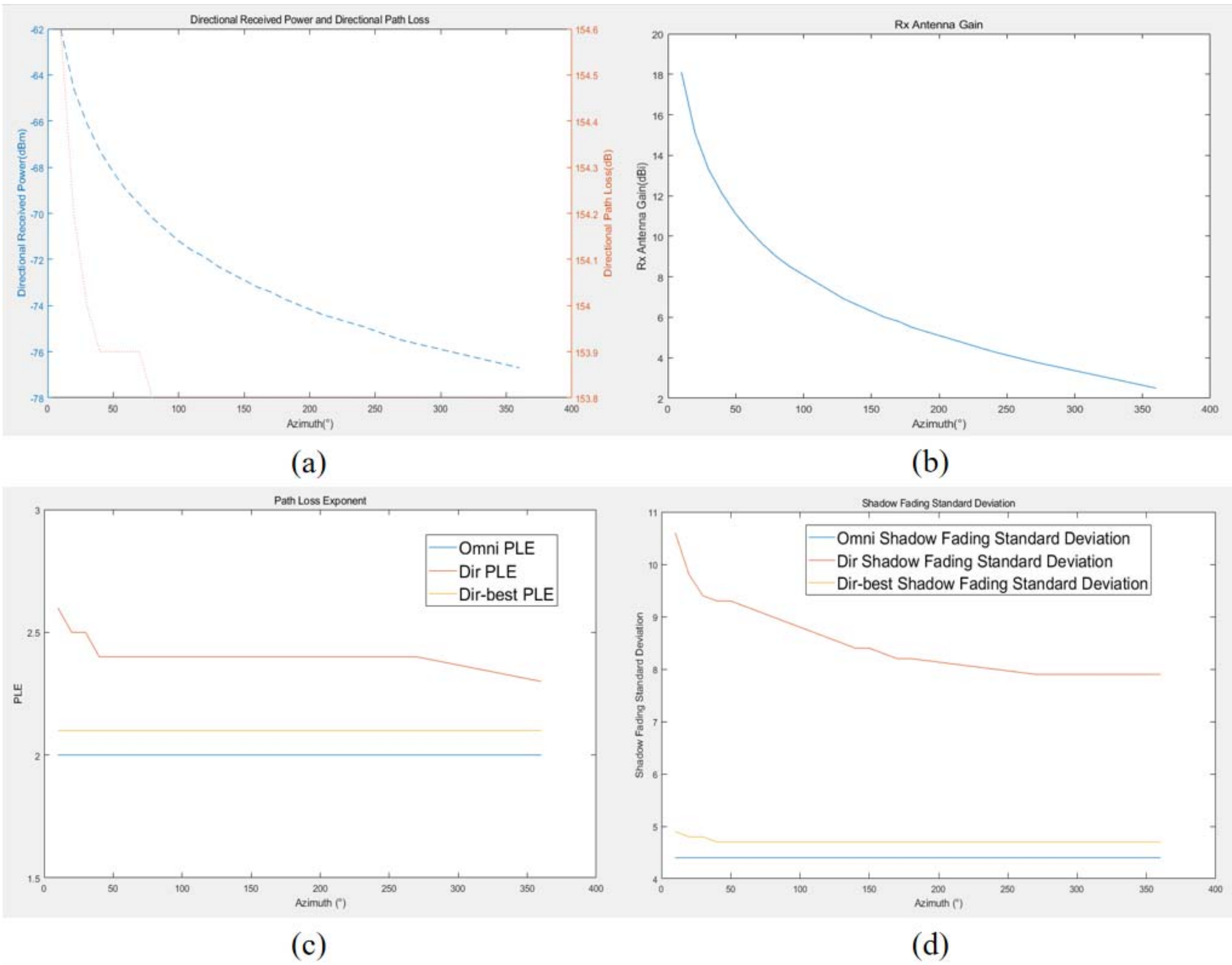

Figure 19. The effects of the azimuth of the receiving antenna, (**a**) directional received power and path loss; (**b**) receiver antenna gain; (**c**) path loss exponent; (**d**) shadow fading standard deviation.

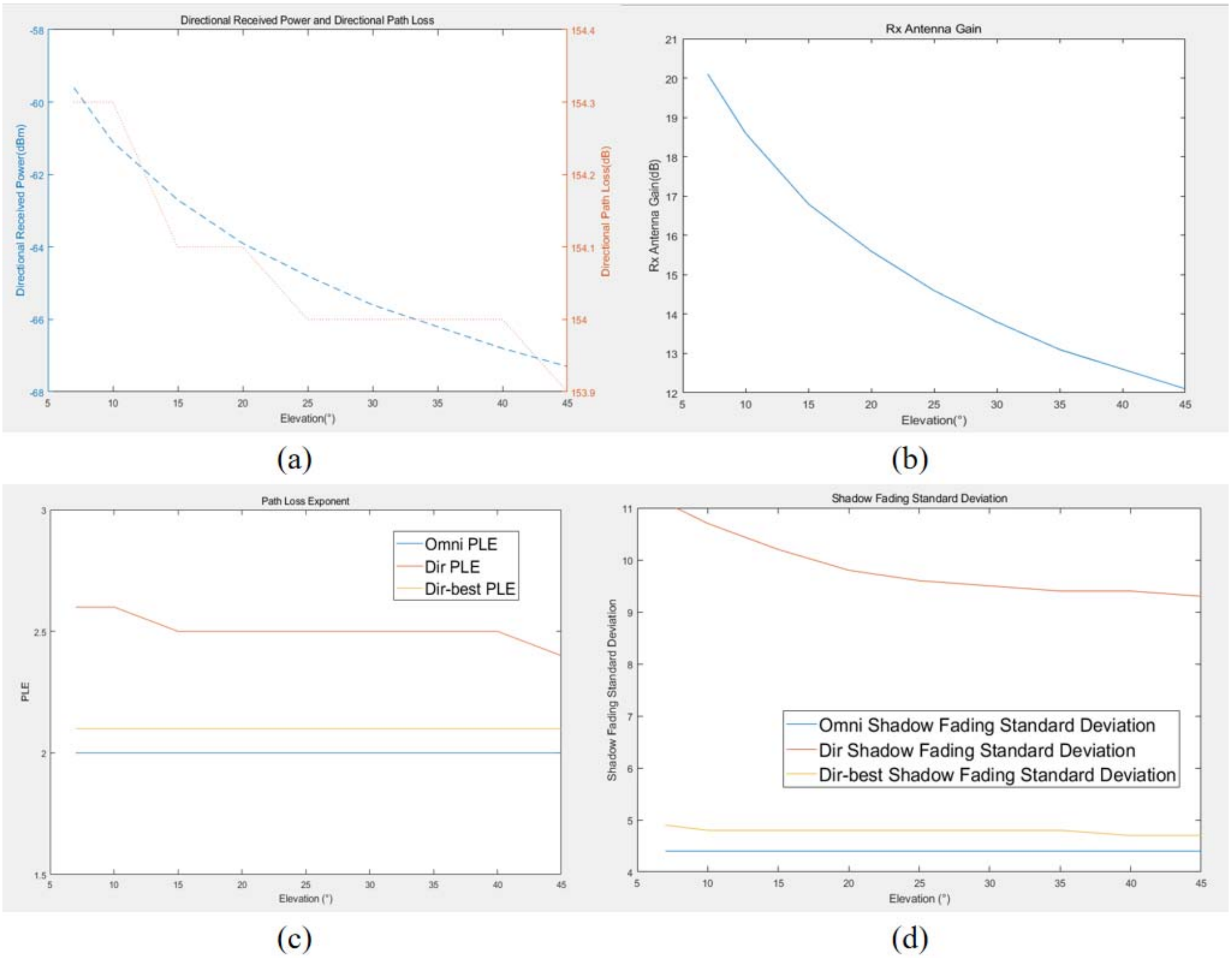

Figure 20. The effects of the elevation of the receiving antenna, (**a**) directional received power and path loss; (**b**) receiver antenna gain; (**c**) path loss exponent; (**d**) shadow fading standard deviation.

5 Conclusions

In this paper, the spatial statistical channel model of high-altitude military UAV air-to-ground scenario is constructed. By using NYUSIM, a multi-dimensional model of the high-altitude military UAV air-to-ground channel without base station was built, and the channel was simulated to get useful statistics. The dependence of the channel on T-R separation distance, frequency, rain rate and antenna HPBW parameters have been analyzed, and large-scale fading and small-scale fading statistical analyses were carried out to get channel characteristics. In addition, by calculating and analyzing the condition number and rank of the channel transmission matrix, the spatial multiplexing of the high-altitude military UAV air-to-ground channel without base station scenario under different MIMO antenna arrays have been analyzed.

According to the channel analysis results, under this model, the linearity of the millimeter band below 49 GHz is better, which is suitable for this battlefield situation awareness scenario. The use of 2×2 and 3×3 MIMO antenna arrays can realize spatial multiplexing effectively. Moreover, this communication channel should also take the rain rate and distance conditions into account, adjust the communication frequency and MIMO antenna parameters flexibly. The result can provide a theoretical basis for future high-altitude military UAV frequency selection and antenna design.

References

Al-Shammari, B. K. J., Hburi, I., Idan, H. R., & Khazaal, H. F. (2021). An Overview of mmWave Communications for 5G. *2021 International Conference on Communication & Information Technology (ICICT)* (pp. 133-139). https://doi.org/10.1109/ICICT52195.2021.9568459

Bai, L., Huang, Z., Zhang, X., & Cheng, X. (2021). A Non-Stationary 3D Model for 6G Massive MIMO mmWave UAV Channels. *IEEE Transactions on Wireless Communications*, 21(6), 4325-4339. https://doi.org/10.1109/TWC.2021.3128970

Bajracharya, R., Shrestha, R., Kim, S., & Jung, H. (2022). 6G NR-U Based Wireless Infrastructure UAV: Standardization, Opportunities, Challenges and Future Scopes. *IEEE Access*, 10, 30536-30555. https://doi.org/10.1109/ACCESS.2022.3159698

Bian, J., Wang, C. -X., Gao, X., You, X., & Zhang, M. (2021). A General 3D Non-Stationary Wireless Channel Model for 5G and Beyond. *IEEE Transactions on Wireless Communications*, 20(5), 3211-3224. https://doi.org/10.1109/TWC.2020.3047973

Bithas, P. S., Nikolaidis, V., Kanatas, A. G., & Karagiannidis, G. K. (2020). UAV-to-Ground Communications: Channel Modeling and UAV Selection. *IEEE Transactions on Communications*, 68(8), 5135-5144. https://doi.org/10.1109/TCOMM.2020.2992040

Chang, H., Wang, C. -X., Liu, Y., Huang, J., Sun, J., Zhang, W., & Gao, X. (2021). A Novel Nonstationary 6G UAV-to-Ground Wireless Channel Model With 3-D Arbitrary Trajectory Changes. *IEEE Internet of Things Journal*, 8(12), 9865-9877. https://doi.org/10.1109/JIOT.2020.3018479

Chetlur, V. V., & Dhillon, H. S. (2017). Downlink Coverage Analysis for a Finite 3-D Wireless Network of Unmanned Aerial Vehicles. *IEEE Transactions on Communications*, 65(10), 4543-4558. https://doi.org/10.1109/TCOMM.2017.2722500

Gao, Q., Wan, Z. -N., Zhang, M. -X., & Ma, W. -Q. (2021). Design and implementation of panorama vehicle-mounted battlefield perception system based on multi-light fusion imaging technology. *2021 2nd International Conference on Computer Communication and Network Security (CCNS)* (pp. 80-83). https://doi.org/10.1109/CCNS53852.2021.00024

Geraci, G., Garcia-Rodriguez, A., Azari, M. M., Lozano, A., Mezzavilla, M., Chatzinotas, S., et al. (2022). What Will the Future of UAV Cellular Communications Be? A Flight From 5G to 6G. *IEEE Communications Surveys & Tutorials*, 24(3), 1304-1335. https://doi.org/10.1109/COMST.2022.3171135

Huang, J., Wang, C. -X., Chang, H., Sun, J., & Gao, X. (2020). Multi-Frequency Multi-Scenario Millimeter Wave MIMO Channel Measurements and Modeling for B5G Wireless Communication Systems. *IEEE Journal on Selected Areas in Communications*, 38(9), 2020-2025. https://doi.org/10.1109/JSAC.2020.3000839

Jawhly, T., & Chandra Tiwari, R. (2021). Loss exponent modeling for the hilly forested region in the VHF band III. *Radio Science*, 56, e2020RS007201. https://doi.org/10.1029/2020RS007201

Ji, Z., Zhang, Y., He, Z., Yeoh, P.L., Li, B., Yin, H., et al. (2022). Wireless Secret Key Generation for Distributed Antenna Systems: A Joint Space-Time-Frequency Perspective. *IEEE Internet of Things Journal*, 9(1), 633-647. https://doi.org/10.1109/JIOT.2021.3084361

Jia, Y., Tu, X., & Yan, W. (2020). An UAV wireless communication noise suppression method based on OFDM modulation and demodulation. *Radio Science*, 55, e2019RS006959. https://doi.org/10.1029/2019RS006959

Kanhere, O., Ju, S., Xing, Y., & Rappaport, T.S. (2019). Map-Assisted Millimeter Wave Localization for Accurate Position Location. *2019 IEEE Global Communications Conference (GLOBECOM)* (pp. 1-6). https://doi.org/10.1109/GLOBECOM38437.2019.9013365

Khawaja, W., Guvenc, I., Matolak, D. W., Fiebig, U. -C., & Schneckenburger, N. (2019). A Survey of Air-to-Ground Propagation Channel Modeling for Unmanned Aerial Vehicles. *IEEE Communications Surveys & Tutorials*, 21(3), 2361-2391. https://doi.org/10.1109/COMST.2019.2915069

Khuwaja, A. A., Chen, Y., Zhao, N., Alouini, M. -S., & Dobbins, P. (2018). A Survey of Channel Modeling for UAV Communications. *IEEE Communications Surveys & Tutorials*, 20(4), 2804-2821. https://doi.org/10.1109/COMST.2018.2856587

Li, X., Feng, W., Chen, Y., Wang, C. -X., & Ge, N. (2020). Maritime Coverage Enhancement Using UAVs Coordinated With Hybrid Satellite-Terrestrial Networks. *IEEE Transactions on Communications*, 68(4), 2355-2369. https://doi.org/10.1109/TCOMM.2020.2966715

Liao, C., Xu, K., Xie, W., & Xia, X. (2020). 3-D massive MIMO channel model for high-speed railway wireless communication. *Radio Science*, 55, e2020RS007070. https://doi.org/10.1029/2020RS007070

Liu, R., Liu, A., Qu, Z., & Xiong, N. N. (2021). An UAV-Enabled Intelligent Connected Transportation System With 6G Communications for Internet of Vehicles. *IEEE Transactions on Intelligent Transportation Systems* (pp. 1-15). https://doi.org/10.1109/TITS.2021.3122567

Liu, Y., Wang, C. -X., Chang, H., He, Y., & Bian, J. (2021). A Novel Non-Stationary 6G UAV Channel Model for Maritime Communications. *IEEE Journal on Selected Areas in Communications*, 39(10), 2992-3005. https://doi.org/10.1109/JSAC.2021.3088664

Liu, Y., Wang, C. -X., Lopez, C. F., Goussetis, G., Yang, Y., & Karagiannidis, G. K. (2019). 3D Non-Stationary Wideband Tunnel Channel Models for 5G High-Speed Train Wireless Communications. *IEEE Transactions on Intelligent Transportation Systems*, 21(1), 259-272. https://doi.org/10.1109/TITS.2019.2890992

Mou, M. A., Mowla, M. M., & Aftabi Momo, S. H. (2019). Statistical Channel Model at mmWave Band Inside High Speed Water Vehicle. *2019 3rd International Conference on Electrical, Computer & Telecommunication Engineering (ICECTE)* (pp. 109-112). https://doi.org/10.1109/ICECTE48615.2019.9303530

NYUSIM. Accessed: Jun. 10, 2019. [Online]. Available: https://wireless.engineering.nyu.edu/nyusim/

Rappaport, T. S. (1996). Wireless communications: Principles and practice. Prentice Hall PTR

Rappaport, T. S., MacCartney, G. R., Samimi, M. K., & Sun, S. (2015). Wideband millimeter-wave propagation measurements and channel models for future wireless communication system design. *IEEE Transactions on Communications*, 63(9), 3029-3056. https://doi.org/10.1109/TCOMM.2015.2434384

Rappaport, T. S., Sun, S., Mayzus, R., Zhao, H., Azar, Y., Wang, K., et al.(2013). Millimeter wave mobile communications for 5G cellular: It will work!. *IEEE Access*, 1, 335-349. https://doi.org/10.1109/ACCESS.2013.2260813

Shen, D., Jiang, B., Liu, T., Guo, J., & Qi, S. (2017). Realizing of a battlefield electromagnetic situation system. *2017 36th Chinese Control Conference (CCC)* (pp. 10304-10309). https://doi.org/10.23919/ChiCC.2017.8028994

Sun, S., MacCartney, G. R., & Rappaport, T. S. (2017). A novel millimeter-wave channel simulator and applications for 5G wireless communications. *2017 IEEE International Conference on Communications (ICC)* (pp. 1-7). https://doi.org/10.1109/ICC.2017.7996792

Sun, S., Rappaport, T.S., Heath, R.W., Nix, A., & Rangan, S. (2014). Mimo for millimeter-wave wireless communications: beamforming, spatial multiplexing, or both?. *IEEE Communications Magazine*, 52(12),110-121. https://doi.org/10.1109/MCOM.2014.6979962

Teixeira, E., Sousa, S., Velez, F. J., & Peha, J. M. (2021). Impact of the propagation model on the capacity in small-cell networks: Comparison between the UHF/SHF and the millimeter wavebands. *Radio Science*, 56, e2020RS007150. https://doi. org/10.1029/2020RS007150

Tian, J., & Shi, J. (2020). A new method for analyzing the attenuation characteristics of satellite radar altimeter signals due to rainfall based on a multilayer medium model. *Radio Science*, 55, e2019RS006962. https://doi.org/10.1029/2019RS006962

Tozer, T., Grace, D., Thompson, J., & Baynham, P. (2000). UAVs and HAPs-potential convergence for military communications. *IEE Colloquium on Military Satellite Communications* (pp. 10/1-10/6). https://doi.org/10.1049/ic:20000130

Traspadini, A., Giordani, M., & Zorzi, M. (2022). UAV/HAP-Assisted Vehicular Edge Computing in 6G: Where and What to Offload?. *2022 Joint European Conference on Networks and Communications & 6G Summit (EuCNC/6G Summit)* (pp. 178-183). https://doi.org/10.1109/EuCNC/6GSummit54941.2022.9815734

Wang, C. -X., Huang, J., Wang, H., Gao, X., You, X., & Hao, Y. (2020). 6G Wireless Channel Measurements and Models: Trends and Challenges. *IEEE Vehicular Technology Magazine*, 15(4), 22-32. https://doi.org/10.1109/MVT.2020.3018436

Wang, J., Wang, C. -X., Huang, J., Wang, H., & Gao, X. (2021). A General 3D Space-Time-Frequency Non-Stationary THz Channel Model for 6G Ultra-Massive MIMO Wireless Communication Systems. *IEEE Journal on Selected Areas in Communications*, 39(6), 1576-1589. https://doi.org/10.1109/JSAC.2021.3071850

Xiao, Z., Zhu, L., Liu, Y., Yi, P., Zhang, R., Xia, X., & Schober, R. (2022). A Survey on Millimeter-Wave Beamforming Enabled UAV Communications and Networking. *IEEE Communications Surveys & Tutorials*, 24(1), 557-610. https://doi.org/10.1109/COMST.2021.3124512

Yang, H., Yang, J., Zhang, B., & Wang, C. (2021). Visualization Analysis of Research on Unmanned-Platform Based Battlefield Situation Awareness. *2021 IEEE International Conference on Artificial Intelligence and Computer Applications (ICAICA)* (pp. 334-338). https://doi.org/10.1109/ICAICA52286.2021.9497890

Yang, J., Li, H., & Xu, Z. (2021). Analysis of channel characteristics between satellite and space station in terahertz band based on ray tracing. *Radio Science*, 56, e2021RS007290. https://doi.org/10.1029/2021RS007290

Yang, X., Song, C., Xu, C., Hao, M., Tan, J., Lou, X., et al. (2022). A survey of the estimation and fusion methods for battlefield situation awareness. *Seventh Asia Pacific Conference on Optics Manufacture and 2021 International Forum of Young Scientists on Advanced Optical Manufacturing (APCOM and YSAOM 2021)*, 1216633. https://doi.org/10.1117/12.2616097

Yang, J.,& Yuan, L. (2022). Analysis of channel characteristics for inter-satellite terahertz communication based on Lambertian model. Journal of Signal Processing, 38(2), 232-240. https://doi.org/10.16798/j.issn.1003-0530.2022.02.002

You, X., Wang, C. -X., Huang, J., Gao, X., Zhang, Z., Wang, M., et al. (2020). Towards 6G wireless communication networks:Vision,enabling technologies, and new pradigm shifts. *Sci China Inf Sci*, 64, 110301. https://doi.org/10.1007/s11432-020-2955-6

Zhang, X., Wang, J., & Poor, H. V. (2022). Statistical QoS-Driven Beamforming and Trajectory Optimizations in UAV/IRS-Based 6G Wireless Networks in the Non-Asymptotic Regime. *2022 IEEE International Symposium on Information Theory (ISIT)* (pp. 3333-3338). https://doi.org/10.1109/ISIT50566.2022.9834715

Zhang, X., Zhu, Q., & Poor, H. V. (2022a). Massive-MIMO Channel Capacity Modeling for mURLLC Over 6G UAV Mobile Wireless Networks. *2022 56th Annual Conference on Information Sciences and Systems (CISS)* (pp. 49-54). https://doi.org/10.1109/CISS53076.2022.9751152

Zhang, X., Zhu, Q., & Poor, H. V. (2022b). Multiple-Access Based UAV Communications and Trajectory Tracking Over 6G Mobile Wireless Networks. *2022 IEEE Wireless Communications and Networking Conference (WCNC)* (pp. 2429-2434). https://doi.org/10.1109/WCNC51071.2022.9771943

Zhang, Y., Zhao, L., & He, Z. (2021). A 3-D hybrid dynamic channel model for indoor THz communications. *China communications*, 18(5), 50-65. https://doi.org/10.23919/JCC.2021.05.004

Zhu, X. (2020). Analysis of military application of UAV swarm technology. *2020 3rd International Conference on Unmanned Systems (ICUS)* (pp. 1200-1204). https://doi.org/10.1109/ICUS50048.2020.9274974

Figure 1.

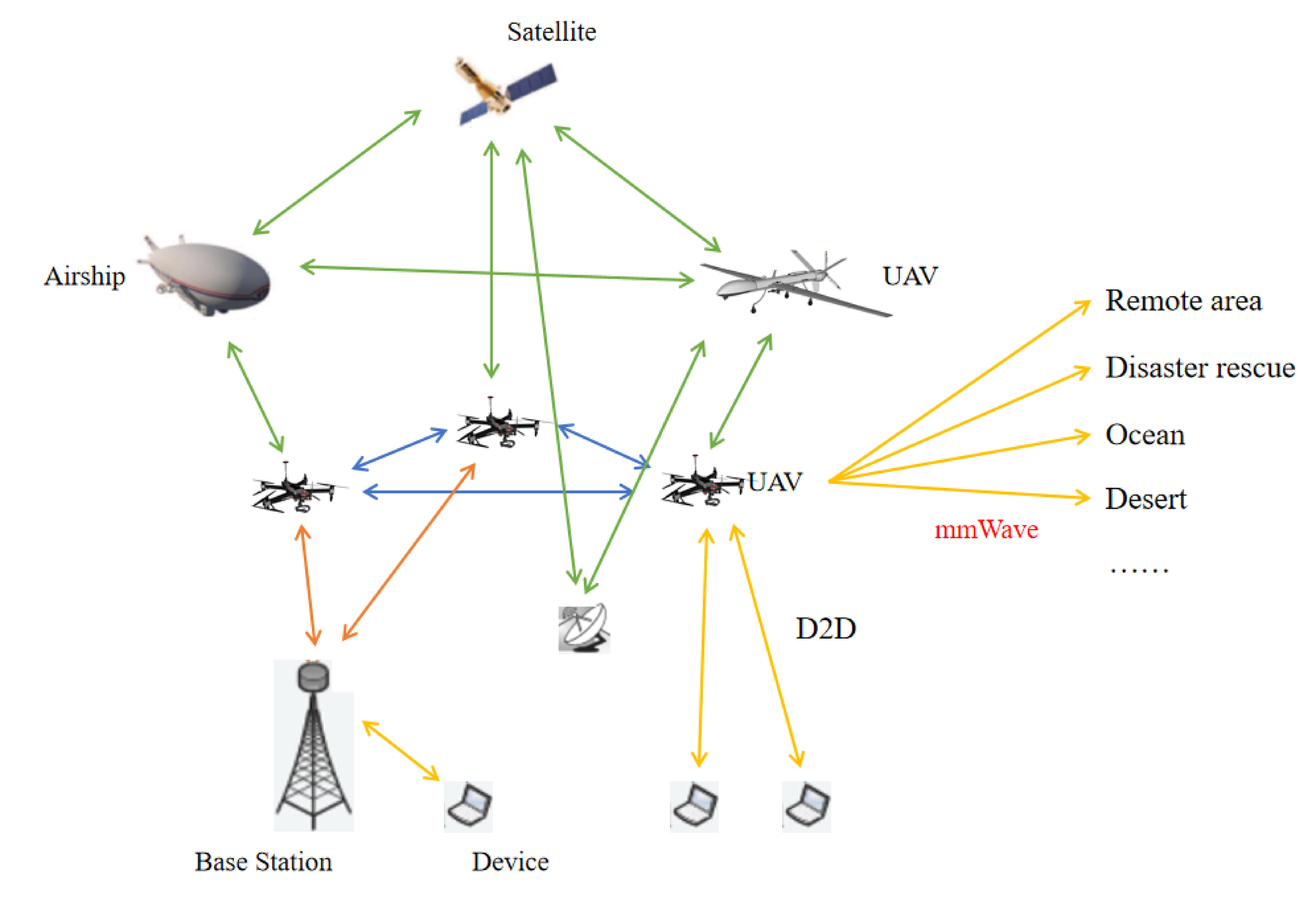
Satellite
Airship
UAV
Remote area
Disaster rescue
Ocean
UAV
Desert
mmWave
……
D2D
Base Station
Device

Figure 2.

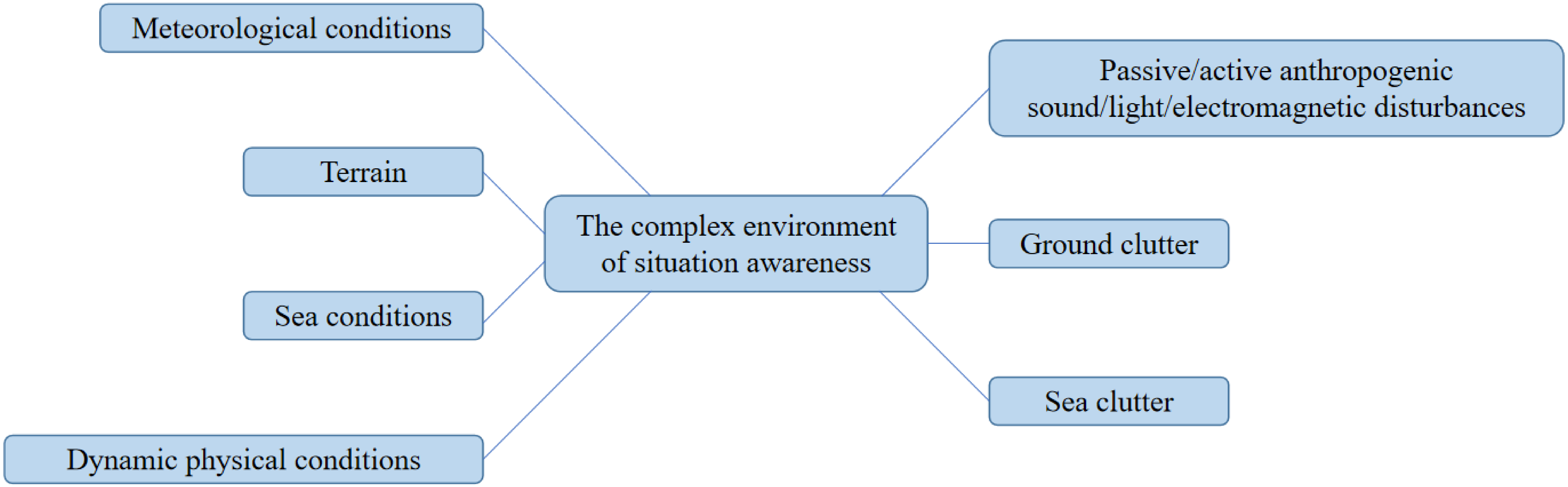
Meteorological conditions
Terrain
Sea conditions
Dynamic physical conditions
The complex environment of situation awareness
Passive/active anthropogenic sound/light/electromagnetic disturbances
Ground clutter
Sea clutter

Figure 3.

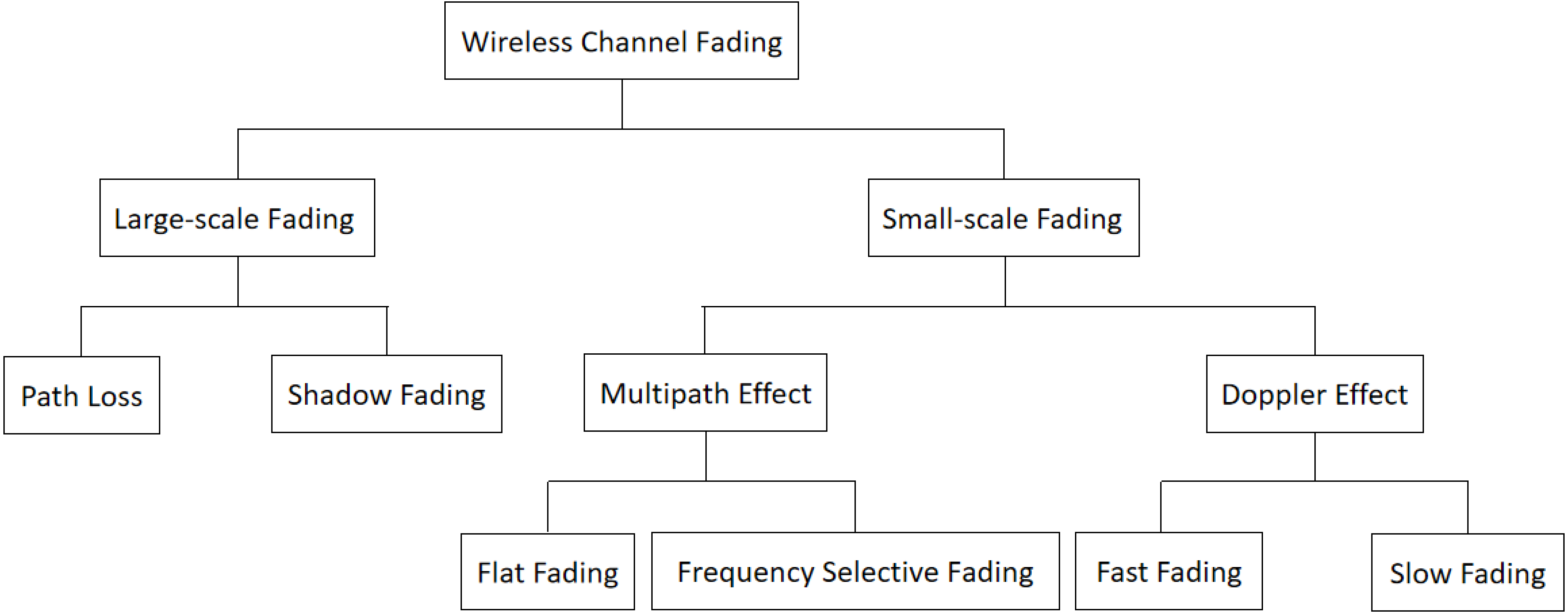
Wireless Channel Fading
Large-scale Fading
Small-scale Fading
Path Loss
Shadow Fading
Multipath Effect
Doppler Effect
Flat Fading
Frequency Selective Fading
Fast Fading
Slow Fading

Figure 4.

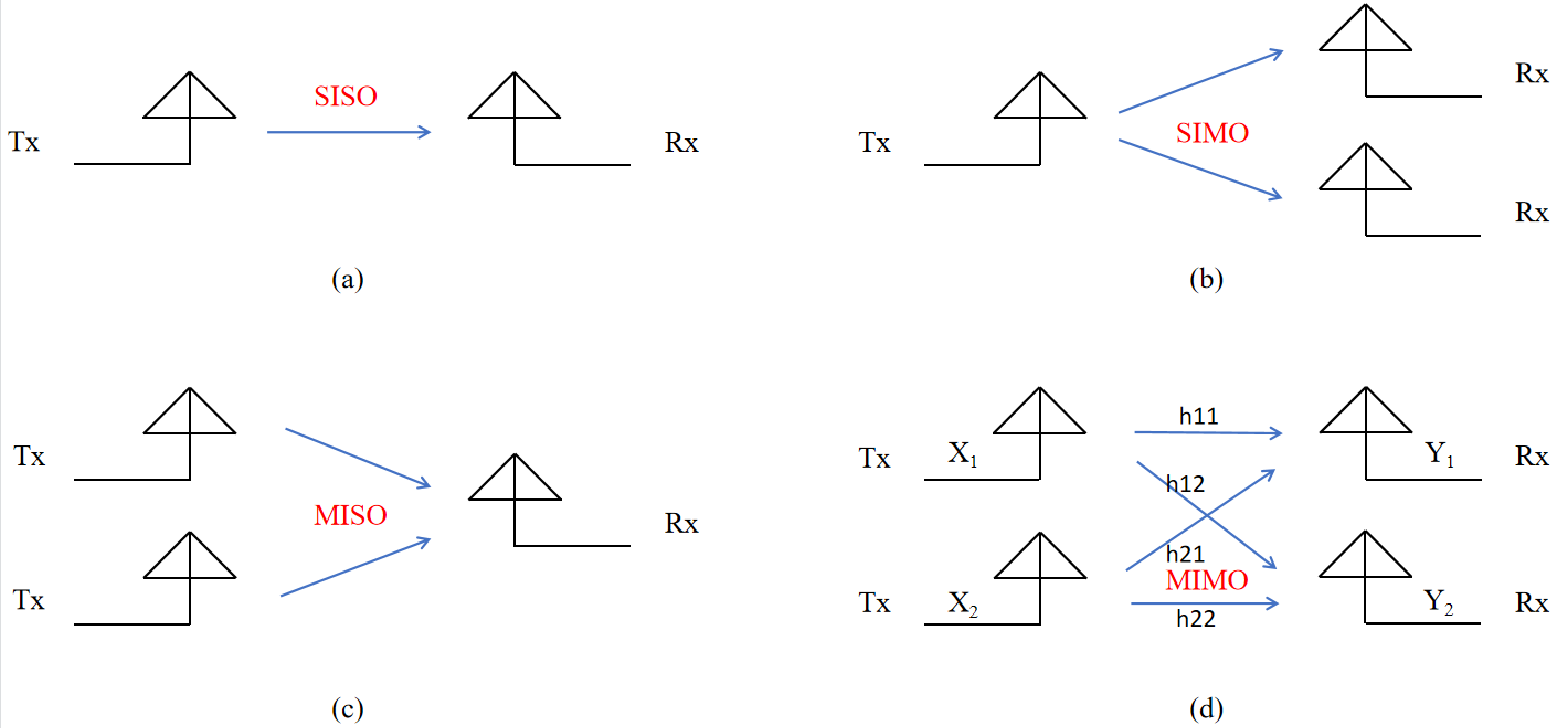
Tx
SISO
Rx
(a)
Tx
SIMO
Rx
Rx
(b)
Tx
Tx
MISO
Rx
(c)
Tx
X_1
h11
h12
h21
MIMO
h22
Y_1
Rx
Tx
X_2
Y_2
Rx
(d)

Figure 5.

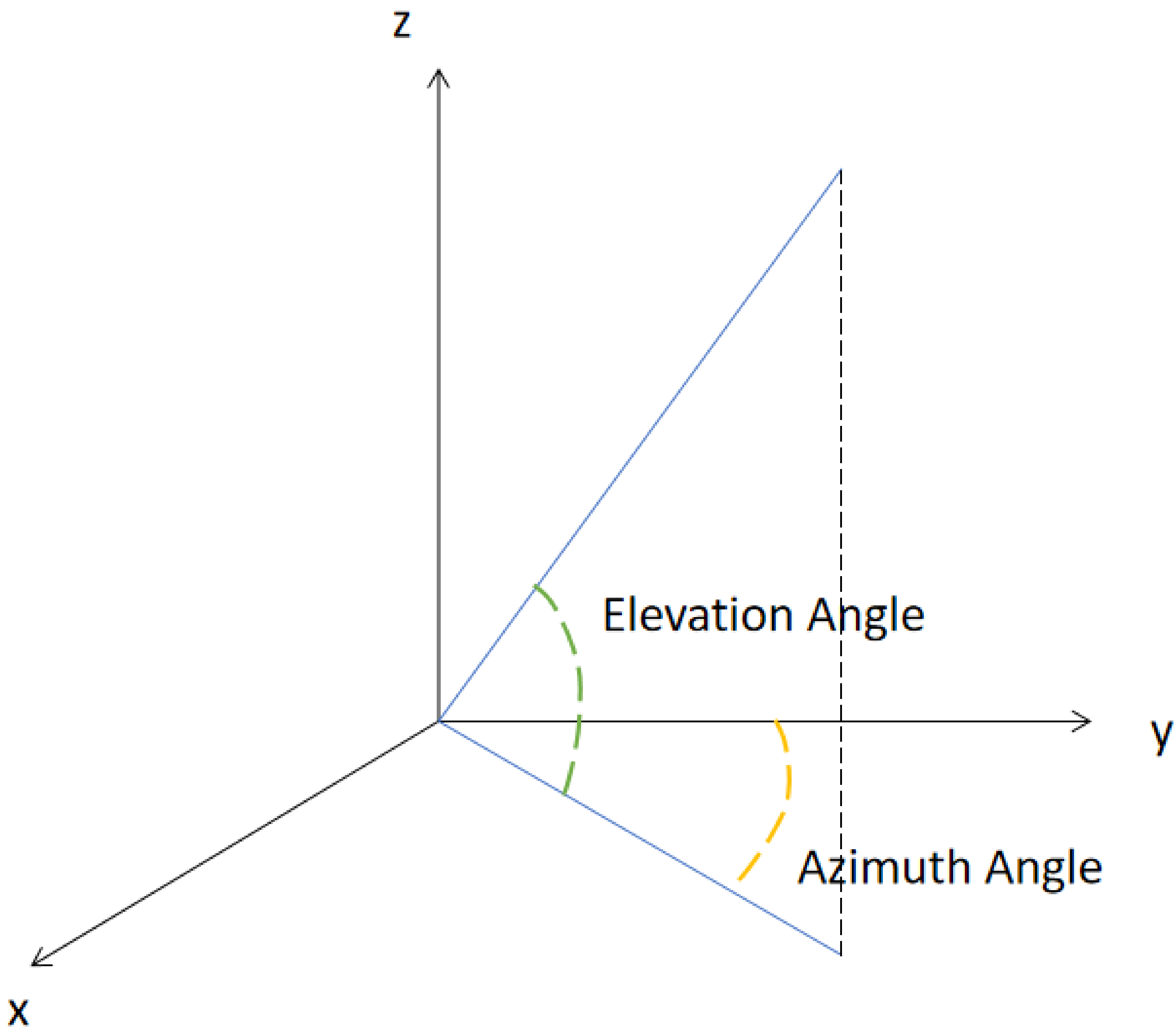
z
Elevation Angle
y
Azimuth Angle
x

Figure 6.

Beam Pattern (the Distribution of Amplitude)

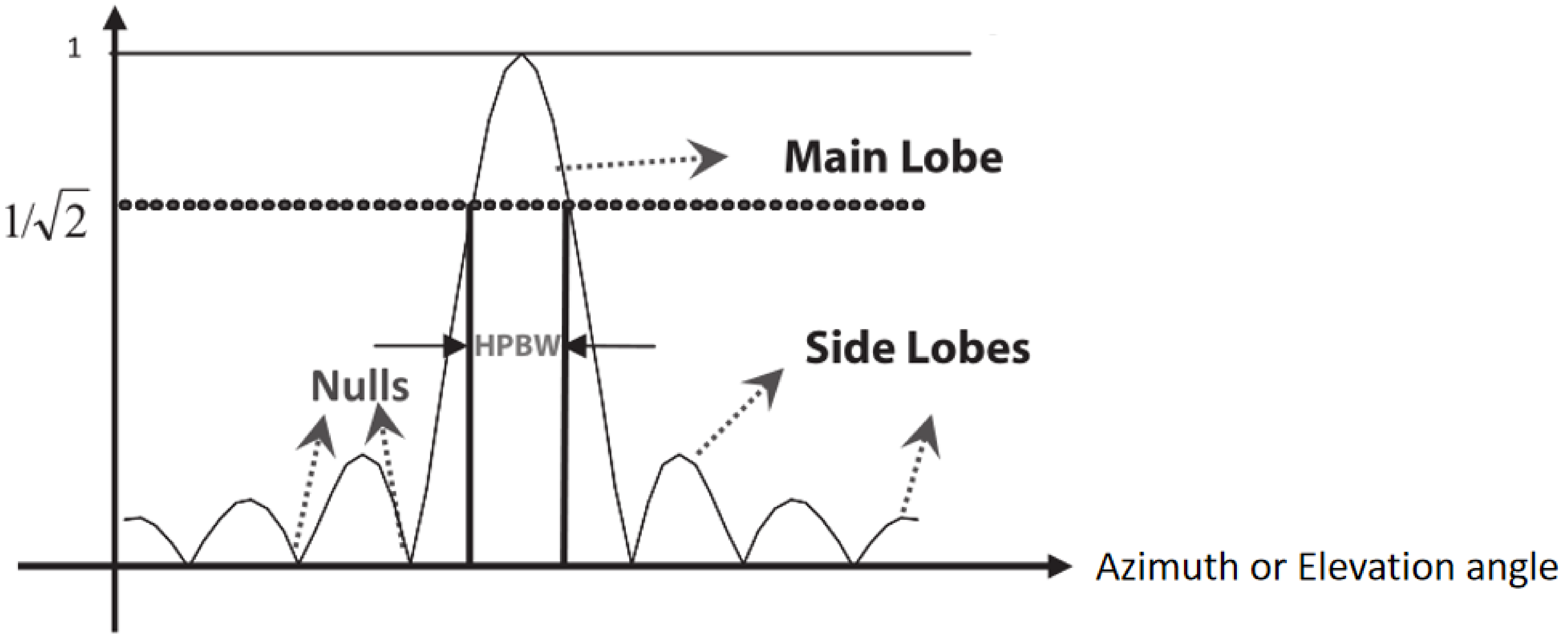

Figure 7.

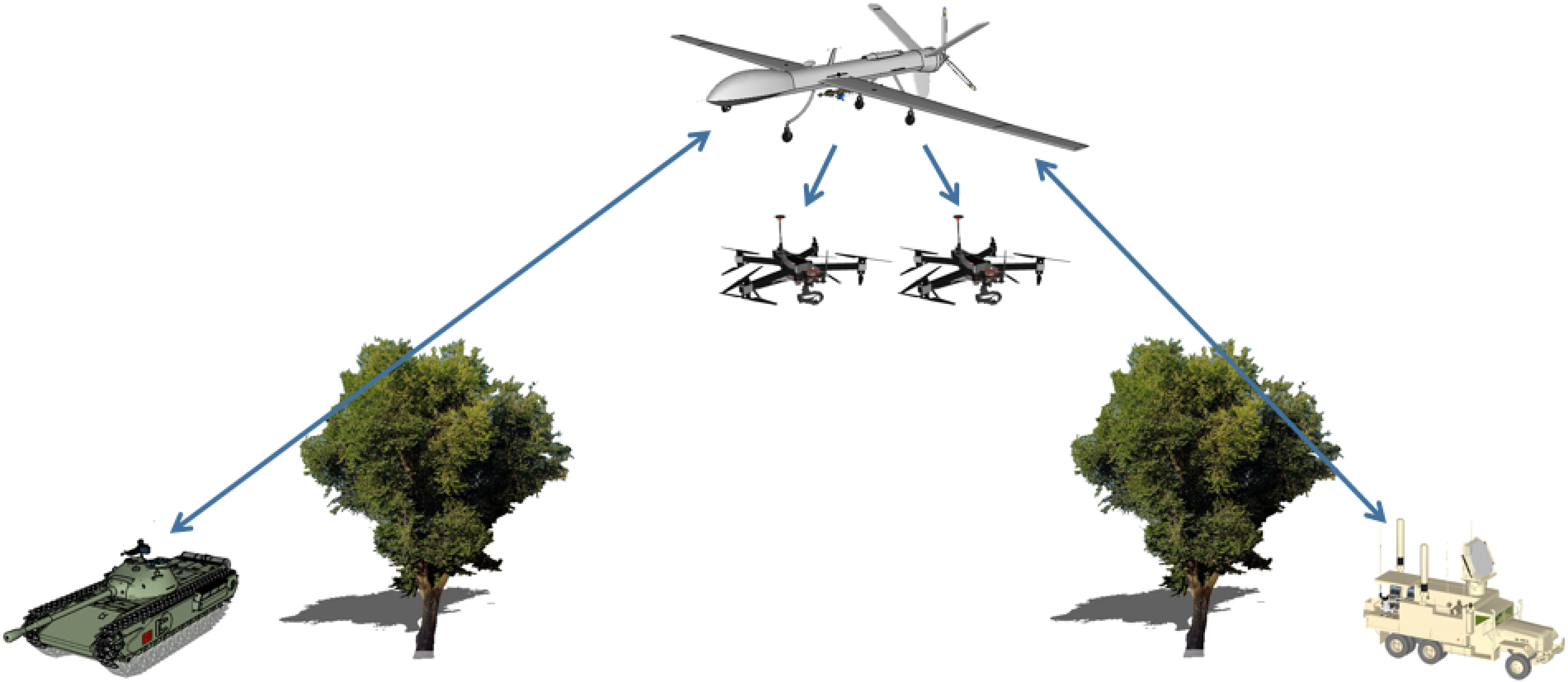

Figure 8.

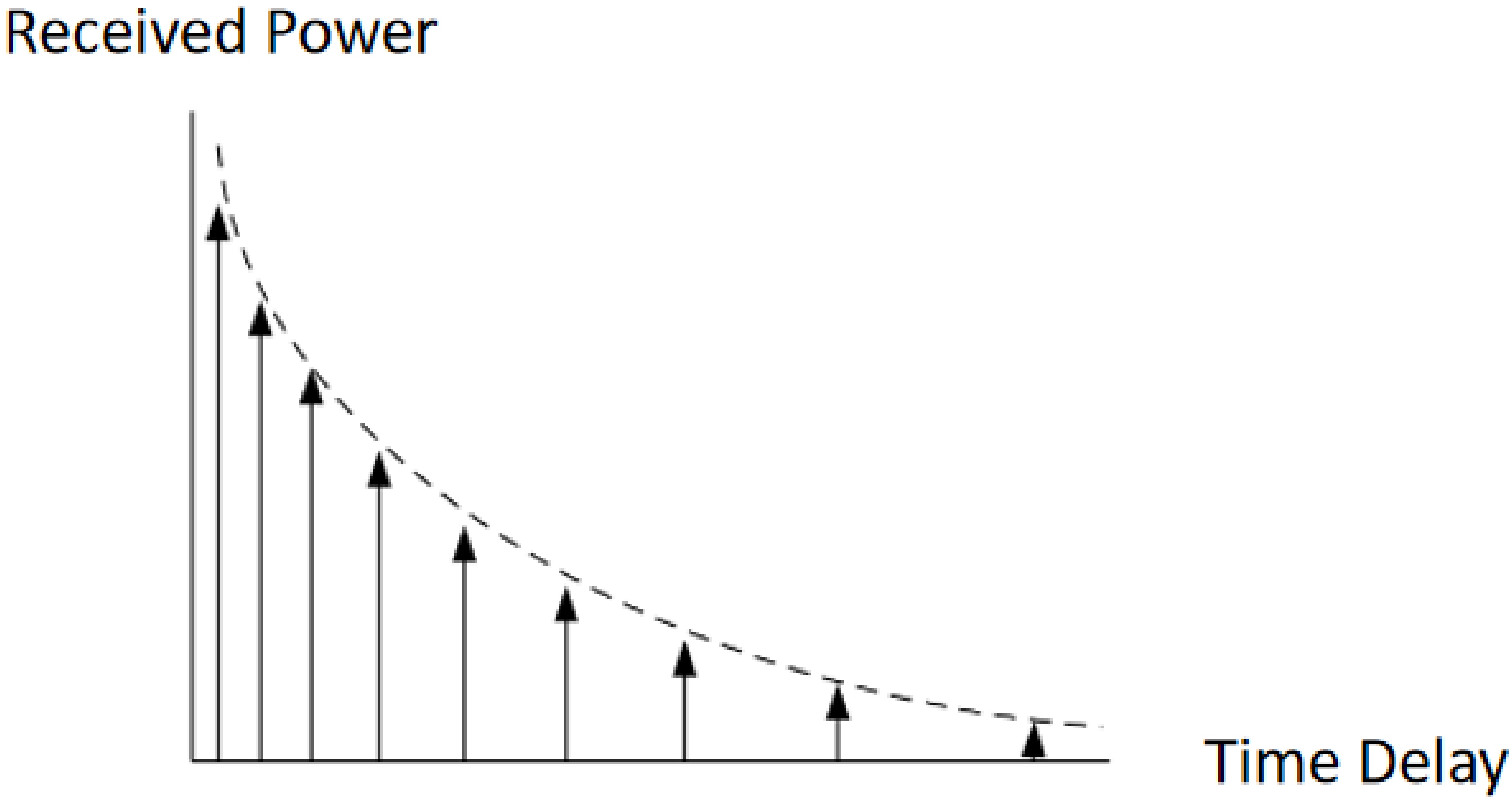
Received Power
Time Delay

Figure 9.

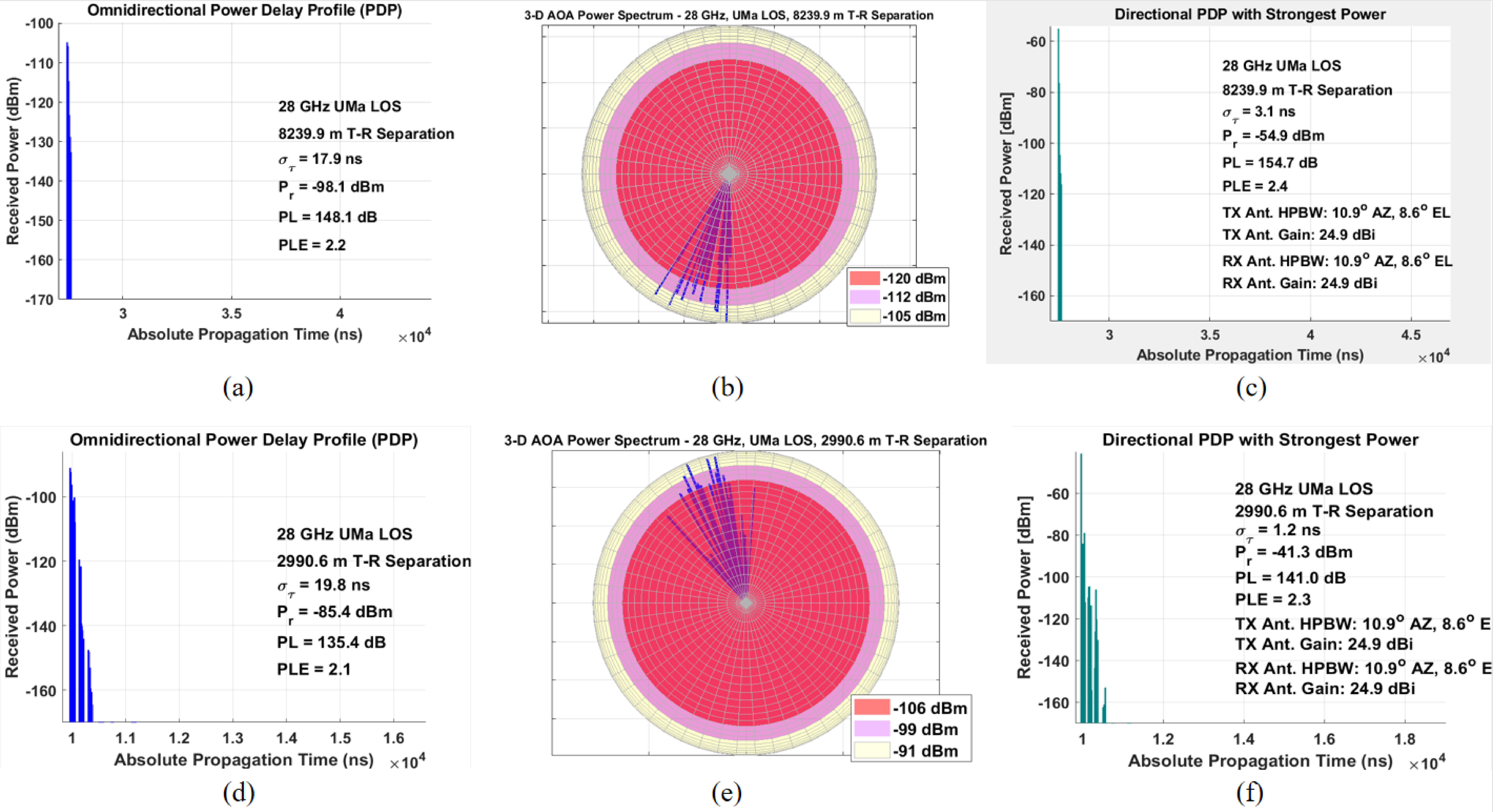

Omnidirectional Power Delay Profile (PDP)
Received Power (dBm)
Absolute Propagation Time (ns)
×10^4
28 GHz UMa LOS
8239.9 m T-R Separation
σ_τ = 17.9 ns
P_r = -98.1 dBm
PL = 148.1 dB
PLE = 2.2
(a)
3-D AOA Power Spectrum - 28 GHz, UMa LOS, 8239.9 m T-R Separation
-120 dBm
-112 dBm
-105 dBm
(b)
Directional PDP with Strongest Power
Received Power [dBm]
Absolute Propagation Time (ns)
×10^4
28 GHz UMa LOS
8239.9 m T-R Separation
σ_τ = 3.1 ns
P_r = -54.9 dBm
PL = 154.7 dB
PLE = 2.4
TX Ant. HPBW: 10.9° AZ, 8.6° EL
TX Ant. Gain: 24.9 dBi
RX Ant. HPBW: 10.9° AZ, 8.6° EL
RX Ant. Gain: 24.9 dBi
(c)
Omnidirectional Power Delay Profile (PDP)
Received Power (dBm)
Absolute Propagation Time (ns)
×10^4
28 GHz UMa LOS
2990.6 m T-R Separation
σ_τ = 19.8 ns
P_r = -85.4 dBm
PL = 135.4 dB
PLE = 2.1
(d)
3-D AOA Power Spectrum - 28 GHz, UMa LOS, 2990.6 m T-R Separation
-106 dBm
-99 dBm
-91 dBm
(e)
Directional PDP with Strongest Power
Received Power [dBm]
Absolute Propagation Time (ns)
×10^4
28 GHz UMa LOS
2990.6 m T-R Separation
σ_τ = 1.2 ns
P_r = -41.3 dBm
PL = 141.0 dB
PLE = 2.3
TX Ant. HPBW: 10.9° AZ, 8.6° E
TX Ant. Gain: 24.9 dBi
RX Ant. HPBW: 10.9° AZ, 8.6° E
RX Ant. Gain: 24.9 dBi
(f)

Figure 10.

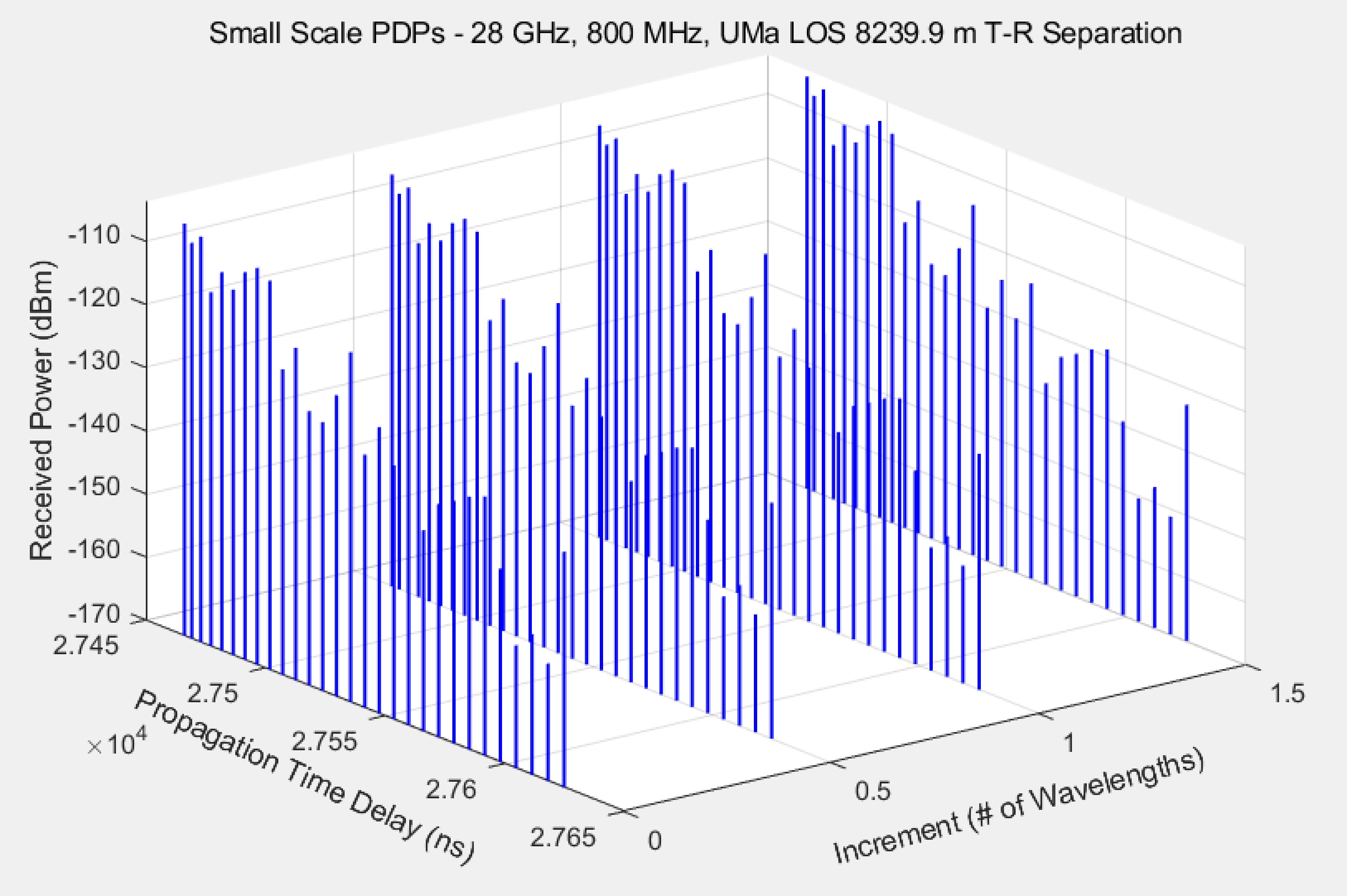

Small Scale PDPs - 28 GHz, 800 MHz, UMa LOS 8239.9 m T-R Separation
Received Power (dBm)
-110
-120
-130
-140
-150
-160
-170
2.745
2.75
2.755
2.76
2.765
×10^4
Propagation Time Delay (ns)
0
0.5
1
1.5
Increment (# of Wavelengths)

Figure 11.

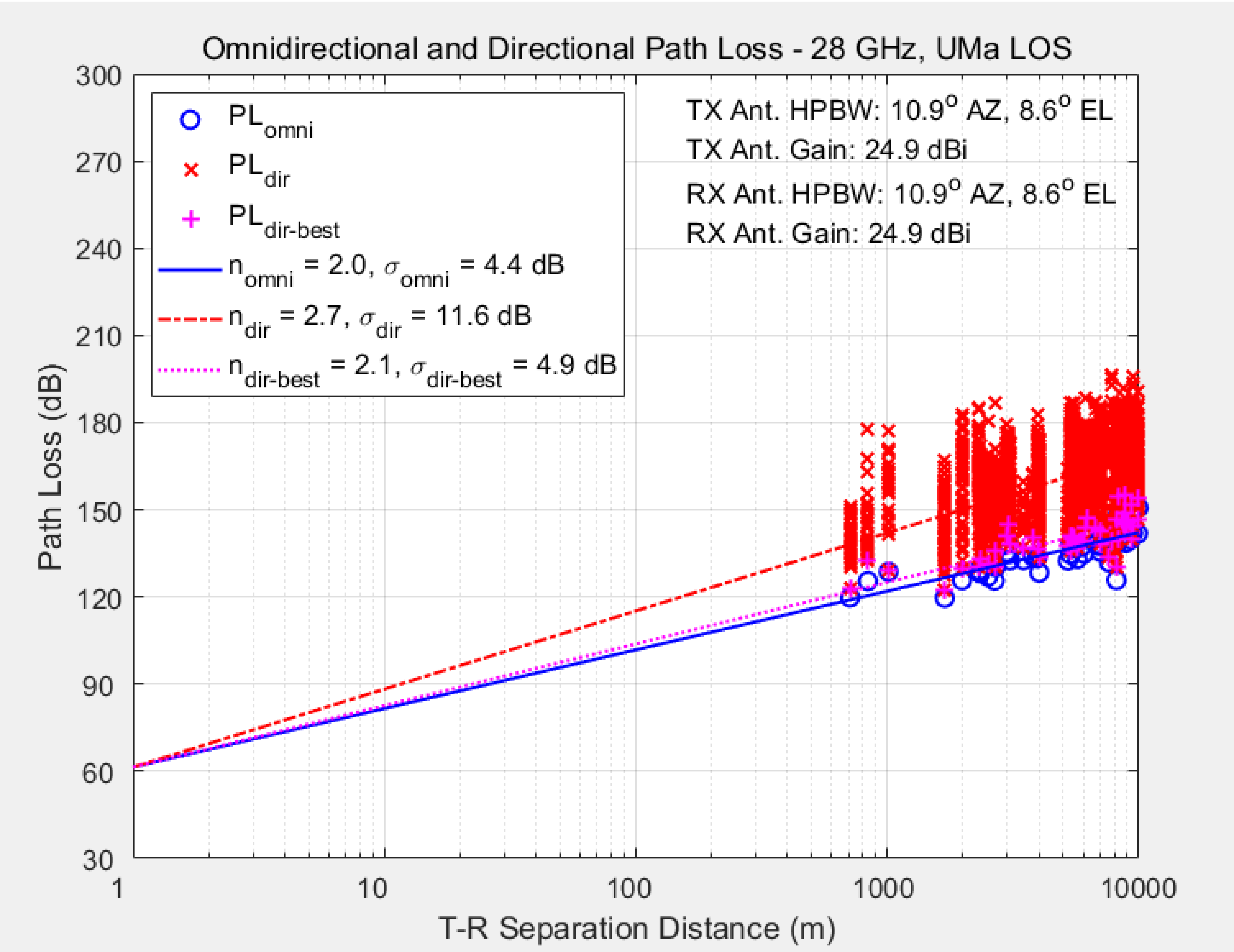

Omnidirectional and Directional Path Loss - 28 GHz, UMa LOS
PL_omni
PL_dir
PL_dir-best
n_omni = 2.0, σ_omni = 4.4 dB
n_dir = 2.7, σ_dir = 11.6 dB
n_dir-best = 2.1, σ_dir-best = 4.9 dB
TX Ant. HPBW: 10.9° AZ, 8.6° EL
TX Ant. Gain: 24.9 dBi
RX Ant. HPBW: 10.9° AZ, 8.6° EL
RX Ant. Gain: 24.9 dBi
Path Loss (dB)
300
270
240
210
180
150
120
90
60
30
1
10
100
1000
10000
T-R Separation Distance (m)

Figure 12.

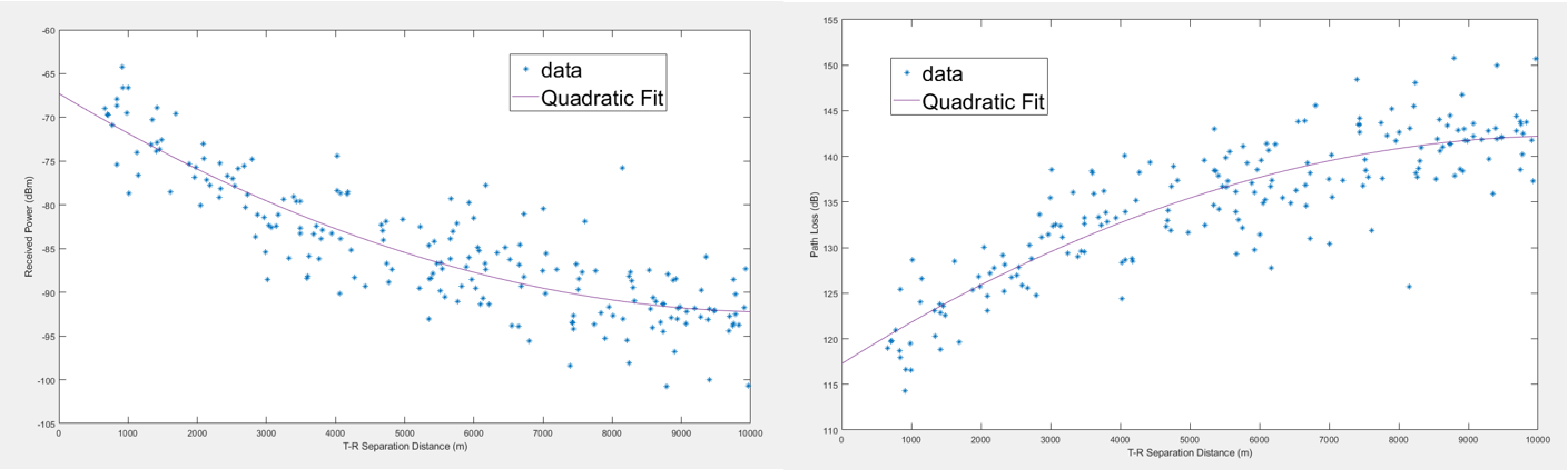
data
Quadratic Fit
Received Power (dBm)
T-R Separation Distance (m)
-60
-65
-70
-75
-80
-85
-90
-95
-100
-105
0
1000
2000
3000
4000
5000
6000
7000
8000
9000
10000
data
Quadratic Fit
Path Loss (dB)
T-R Separation Distance (m)
155
150
145
140
135
130
125
120
115
110

(a) (b)

Figure 13.

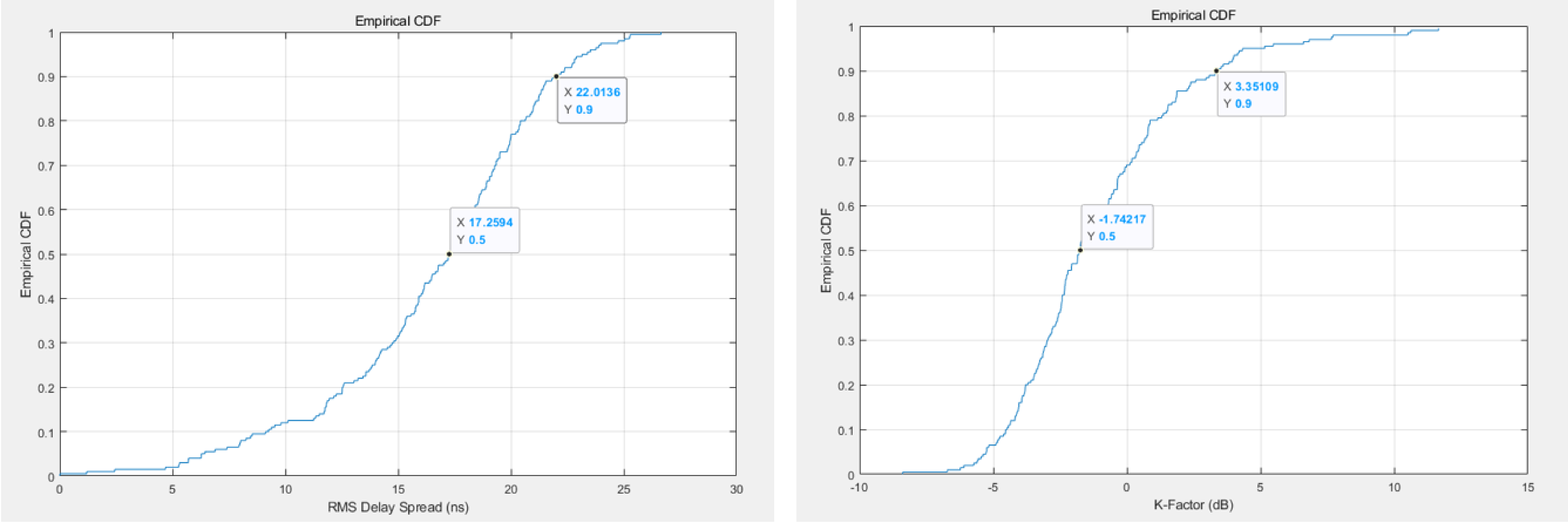
Empirical CDF
Empirical CDF
RMS Delay Spread (ns)
X 22.0136
Y 0.9
X 17.2594
Y 0.5
0
5
10
15
20
25
30
0
0.1
0.2
0.3
0.4
0.5
0.6
0.7
0.8
0.9
1
Empirical CDF
Empirical CDF
K-Factor (dB)
X 3.35109
Y 0.9
X -1.74217
Y 0.5
-10
-5
0
5
10
15

(a) (b)

Figure 14.

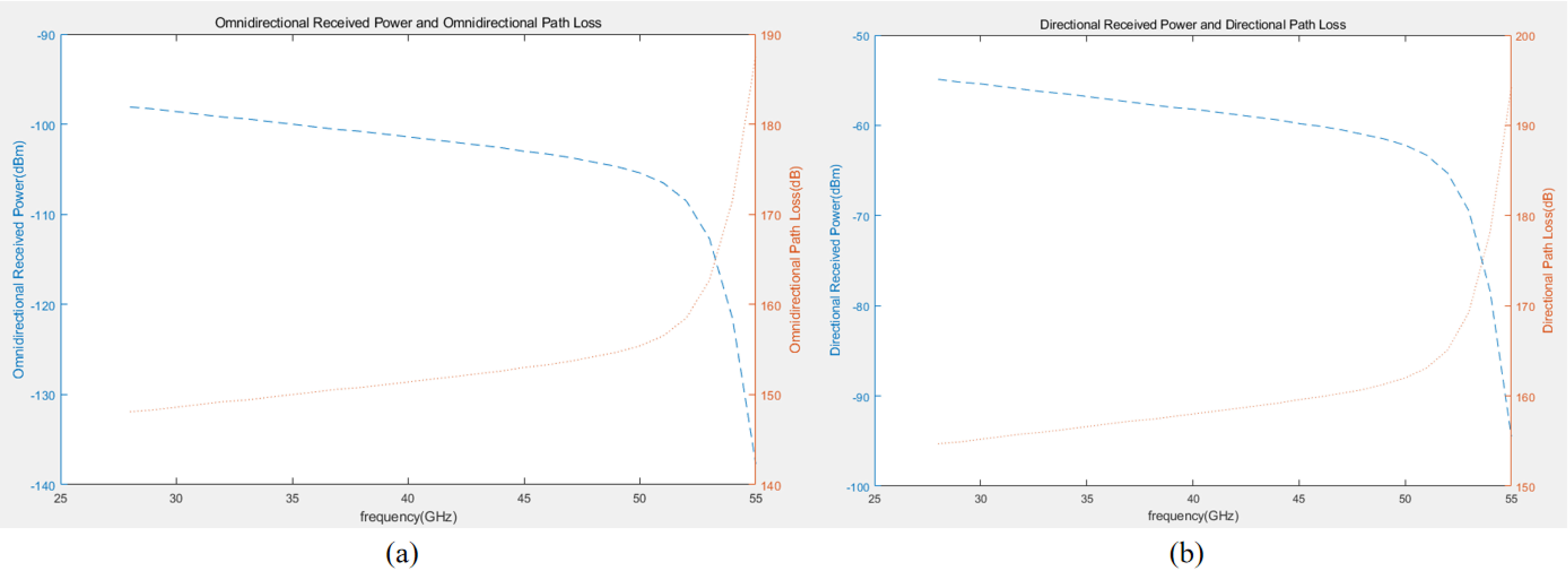
Omnidirectional Received Power and Omnidirectional Path Loss
Omnidirectional Received Power(dBm)
Omnidirectional Path Loss(dB)
frequency(GHz)
-90
-100
-110
-120
-130
-140
190
180
170
160
150
140
25
30
35
40
45
50
55
(a)
Directional Received Power and Directional Path Loss
Directional Received Power(dBm)
Directional Path Loss(dB)
frequency(GHz)
-50
-60
-70
-80
-90
-100
200
190
180
170
160
150
(b)

Figure 15.

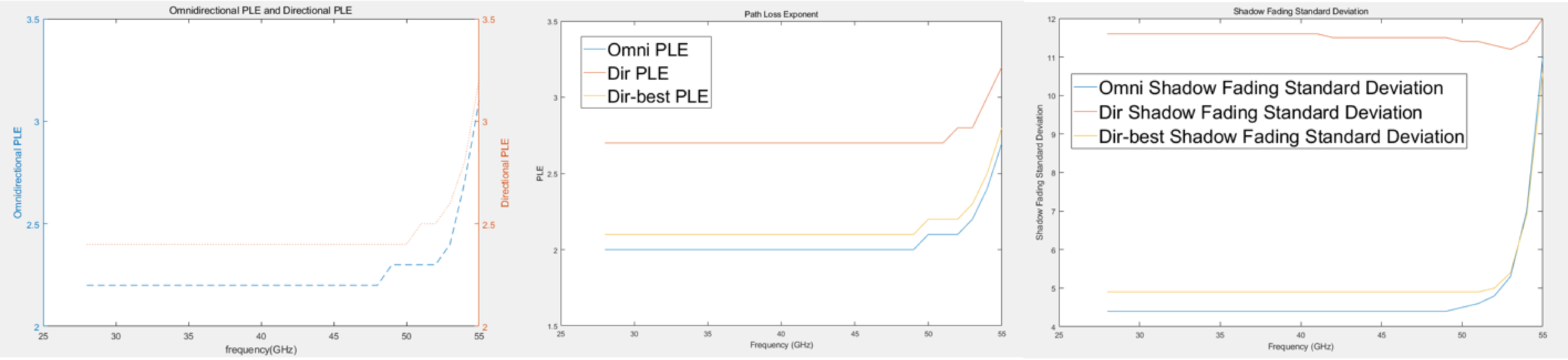
Omnidirectional PLE and Directional PLE
Omnidirectional PLE
Directional PLE
frequency(GHz)
Path Loss Exponent
Omni PLE
Dir PLE
Dir-best PLE
PLE
Frequency (GHz)
Shadow Fading Standard Deviation
Omni Shadow Fading Standard Deviation
Dir Shadow Fading Standard Deviation
Dir-best Shadow Fading Standard Deviation
Shadow Fading Standard Deviation
Frequency (GHz)

(a) (b) (c)

Figure 16.

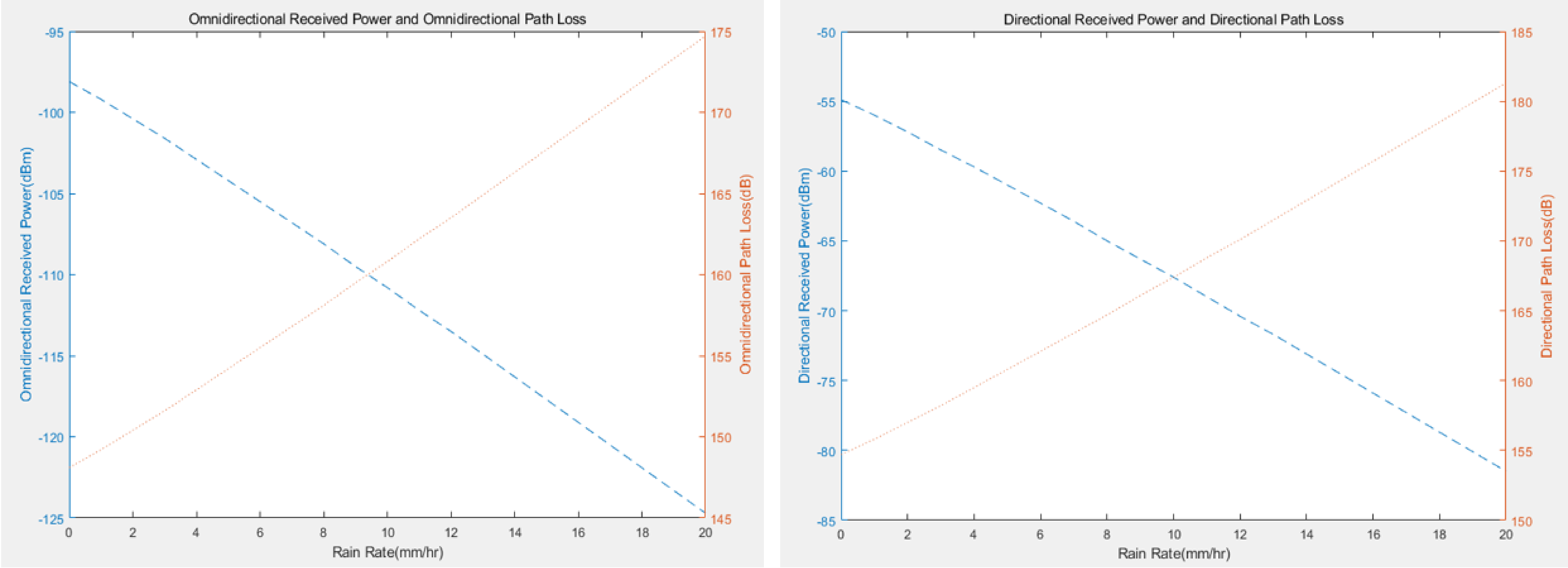
Omnidirectional Received Power and Omnidirectional Path Loss
Omnidirectional Received Power(dBm)
Omnidirectional Path Loss(dB)
Rain Rate(mm/hr)
-95
-100
-105
-110
-115
-120
-125
175
170
165
160
155
150
145
0
2
4
6
8
10
12
14
16
18
20
Directional Received Power and Directional Path Loss
Directional Received Power(dBm)
Directional Path Loss(dB)
Rain Rate(mm/hr)
-50
-55
-60
-65
-70
-75
-80
-85
185
180
175
170
165
160
155
150
0
2
4
6
8
10
12
14
16
18
20

(a) (b)

Figure 17.

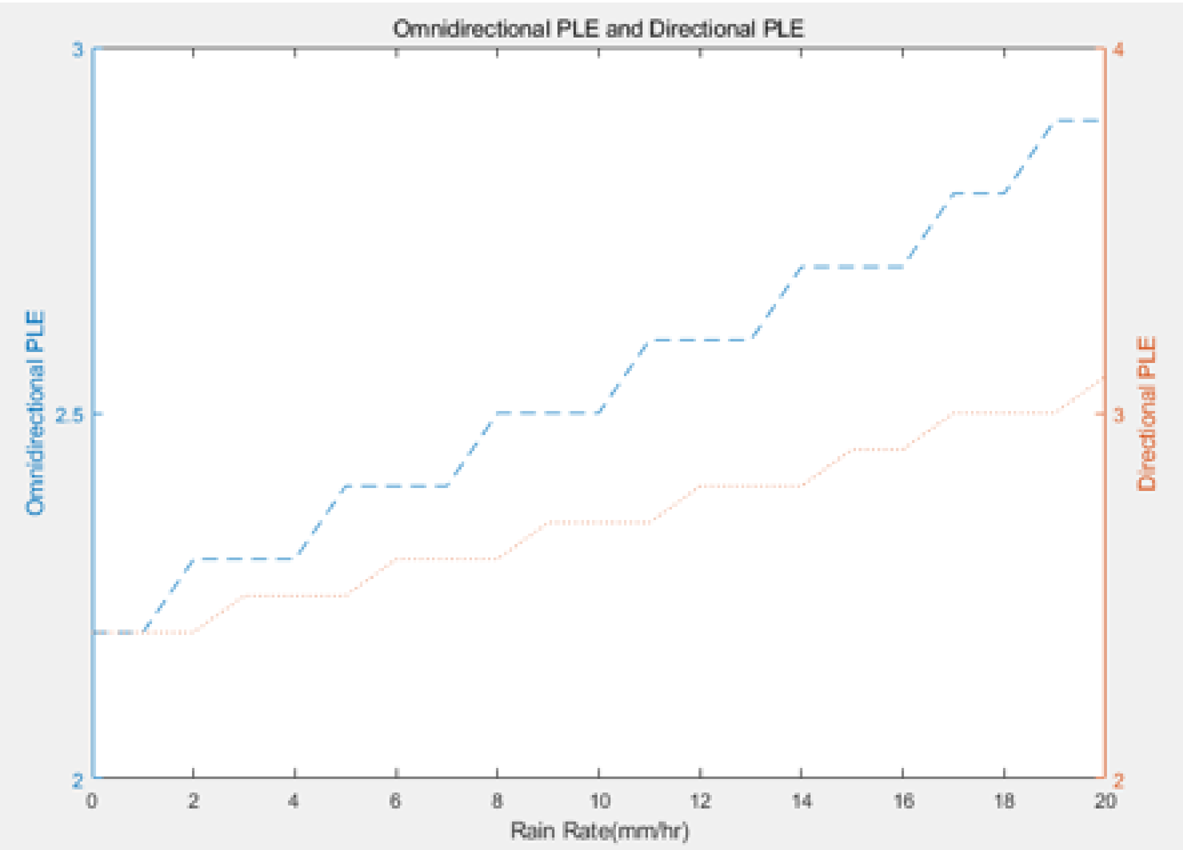
Omnidirectional PLE and Directional PLE
Omnidirectional PLE
Directional PLE
Rain Rate(mm/hr)
3
2.5
2
4
3
2
0
2
4
6
8
10
12
14
16
18
20

(a)

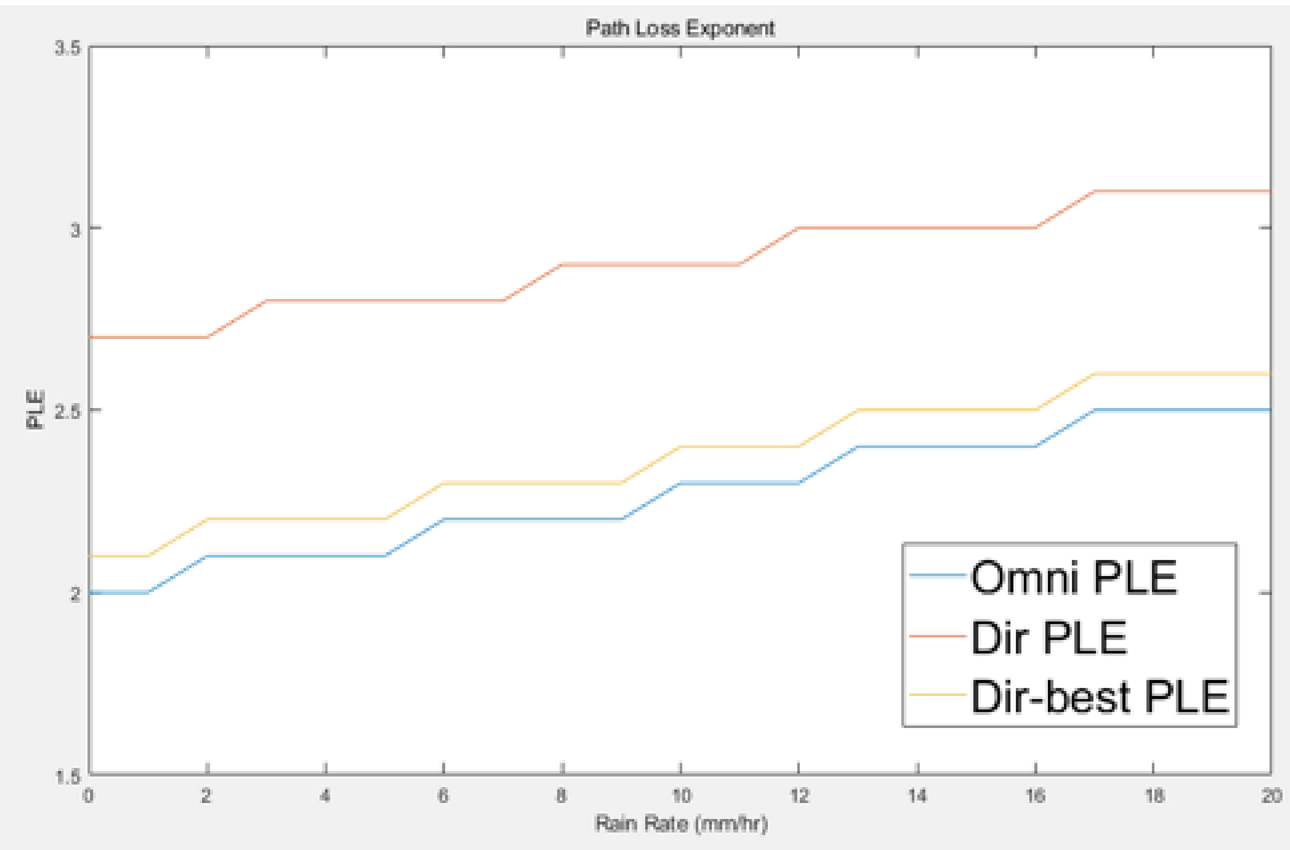
Path Loss Exponent
PLE
Rain Rate (mm/hr)
Omni PLE
Dir PLE
Dir-best PLE
3.5
3
2.5
2
1.5
0
2
4
6
8
10
12
14
16
18
20

(b)

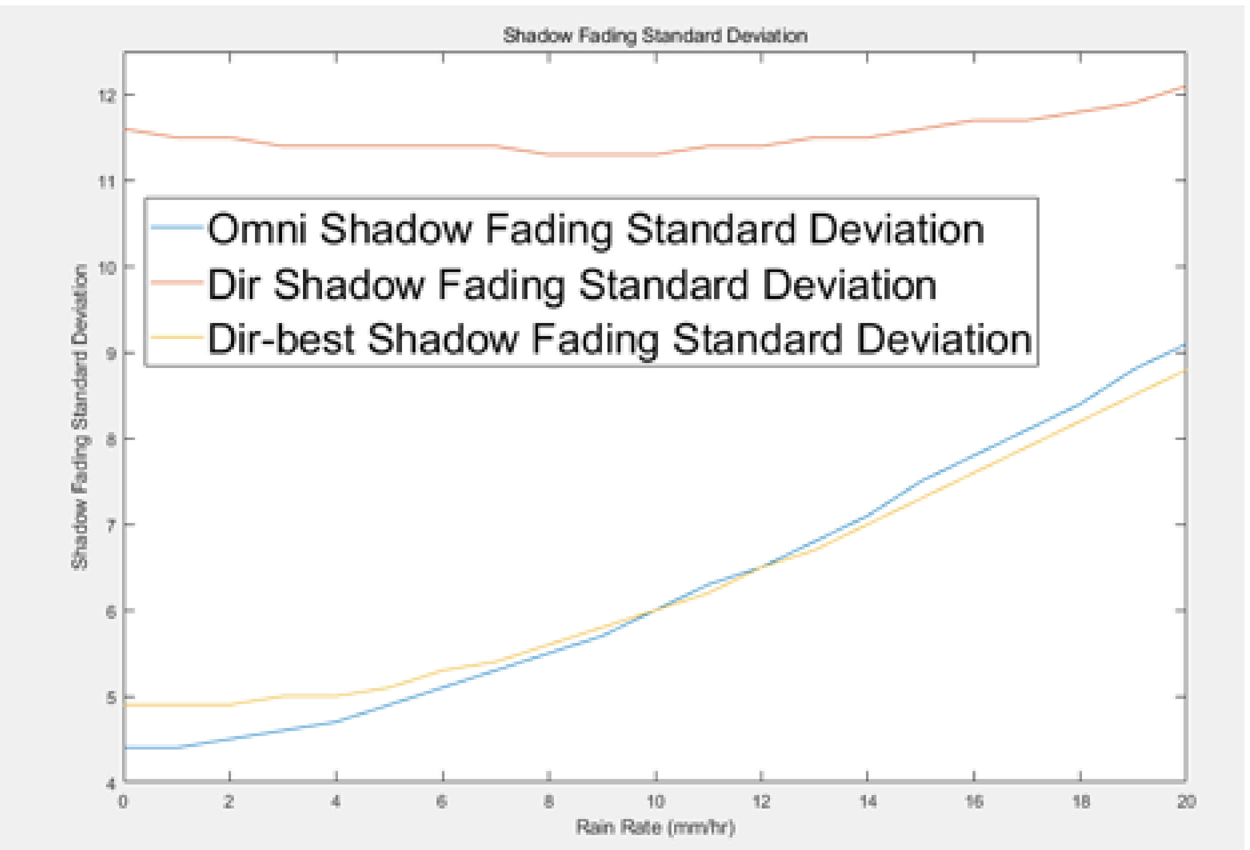
Shadow Fading Standard Deviation
Shadow Fading Standard Deviation
Rain Rate (mm/hr)
Omni Shadow Fading Standard Deviation
Dir Shadow Fading Standard Deviation
Dir-best Shadow Fading Standard Deviation
12
11
10
9
8
7
6
5
4
0
2
4
6
8
10
12
14
16
18
20

(c)

Figure 18.

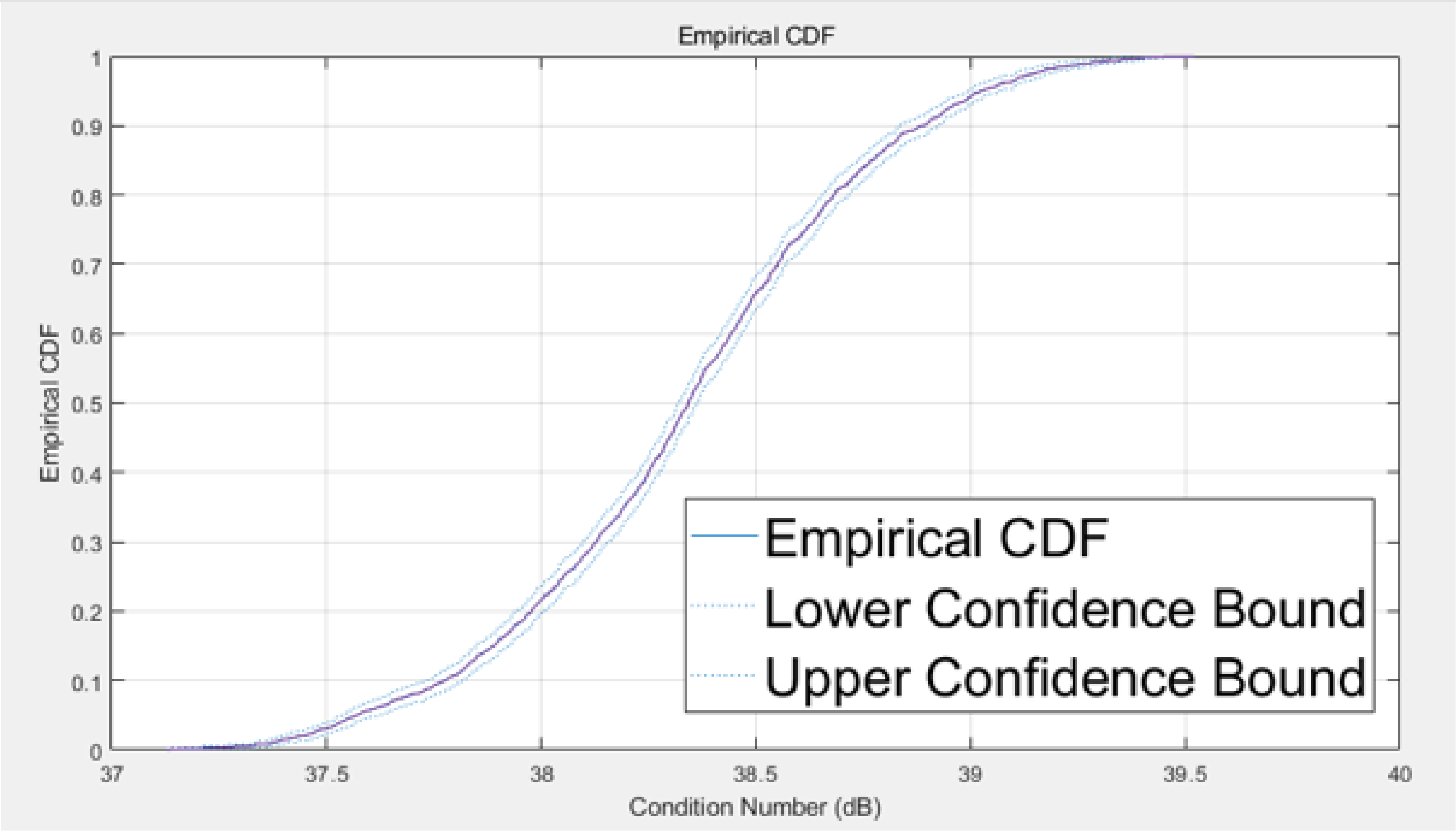
Empirical CDF
Empirical CDF
Condition Number (dB)
Empirical CDF
Lower Confidence Bound
Upper Confidence Bound

(a)

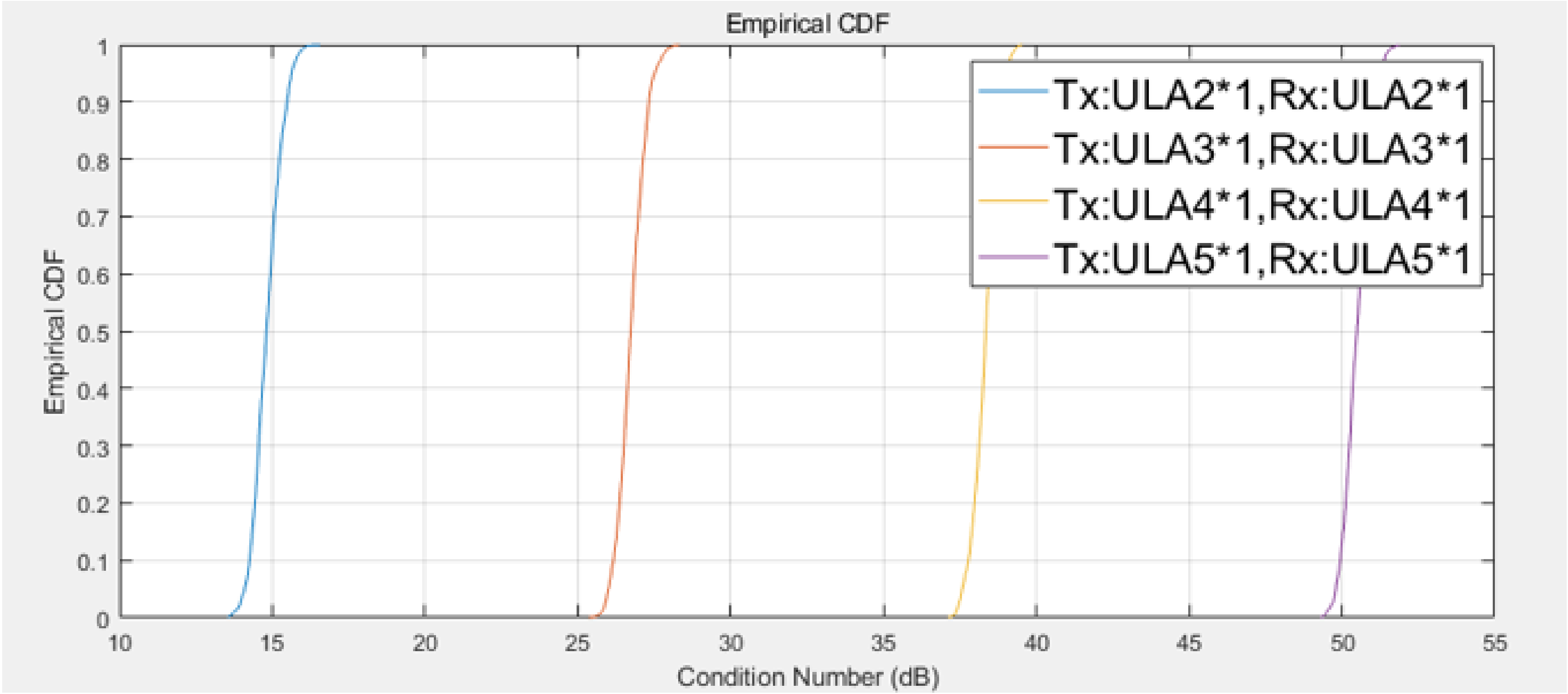
Empirical CDF
Empirical CDF
Condition Number (dB)
Tx:ULA2*1,Rx:ULA2*1
Tx:ULA3*1,Rx:ULA3*1
Tx:ULA4*1,Rx:ULA4*1
Tx:ULA5*1,Rx:ULA5*1

(b)

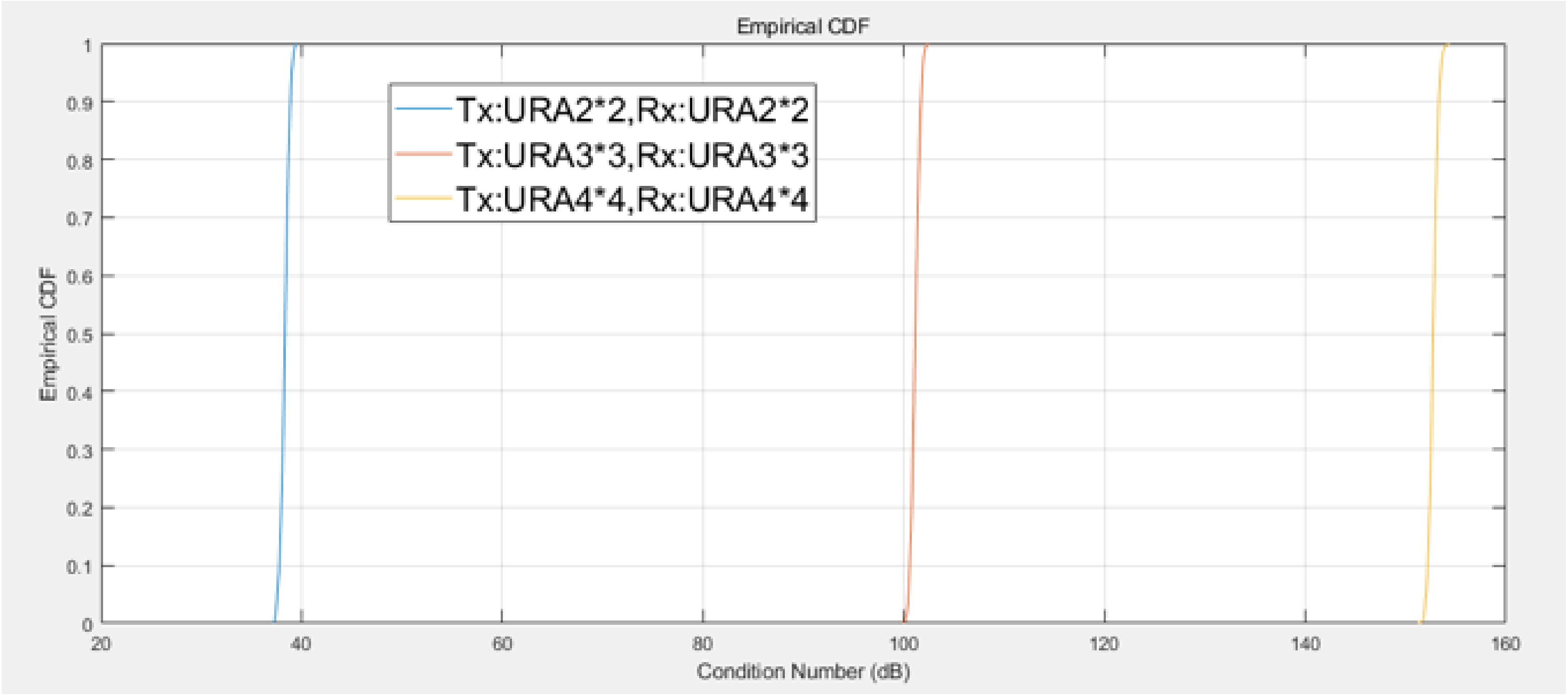
Empirical CDF
Empirical CDF
Condition Number (dB)
Tx:URA2*2,Rx:URA2*2
Tx:URA3*3,Rx:URA3*3
Tx:URA4*4,Rx:URA4*4

(c)

Figure 19.

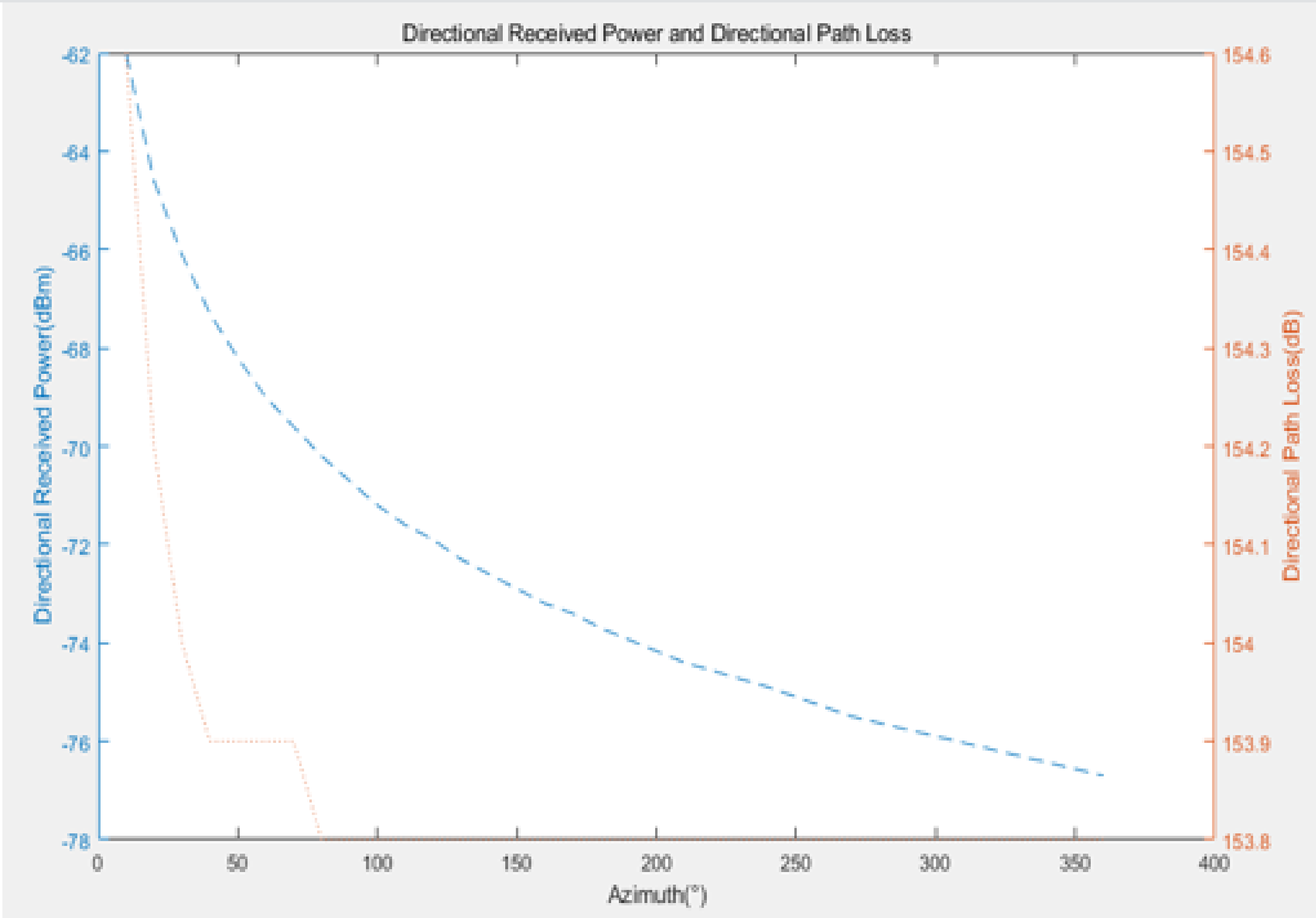
Directional Received Power and Directional Path Loss
Directional Received Power(dBm)
Directional Path Loss(dB)
Azimuth(°)

(a)

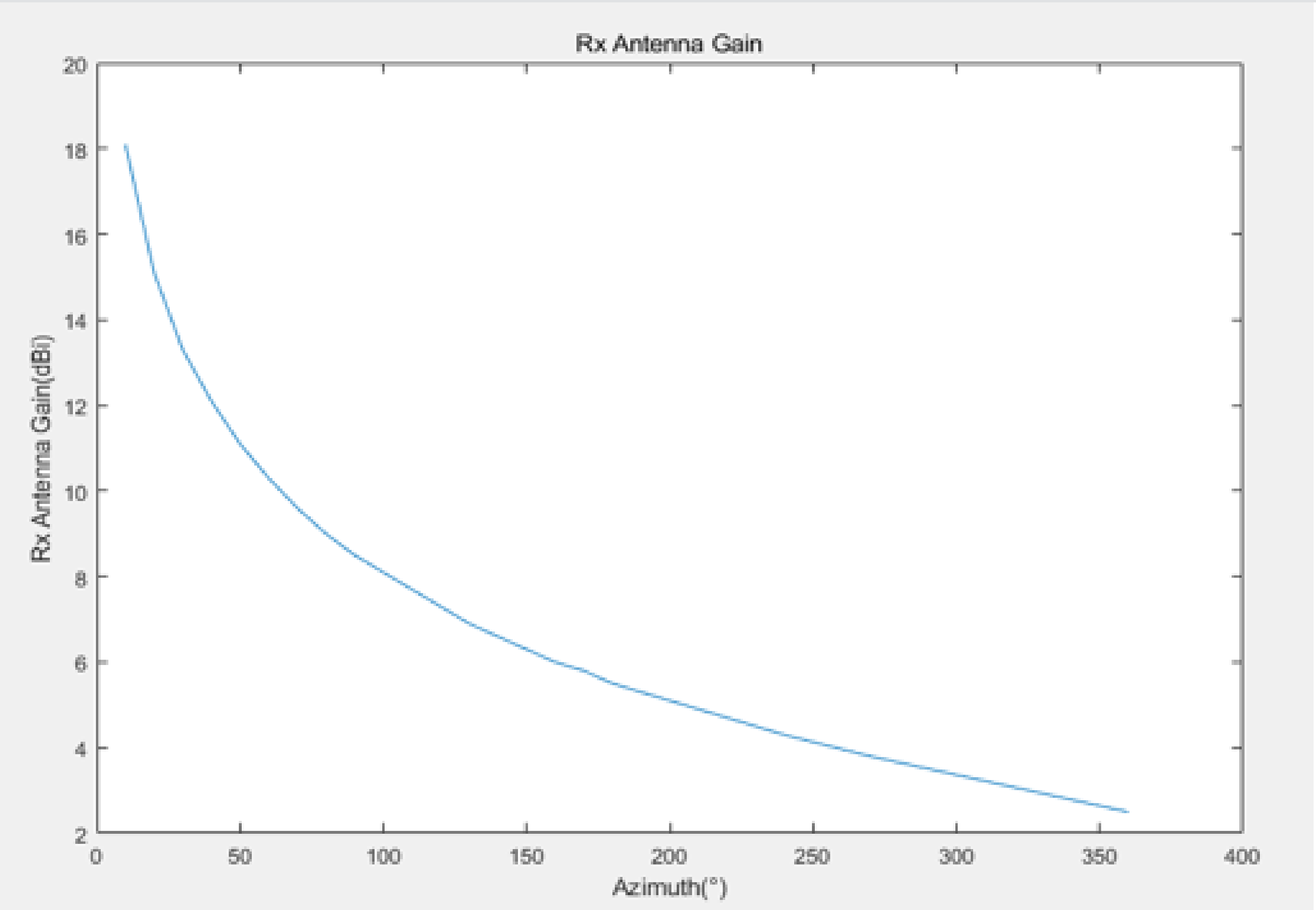
Rx Antenna Gain
Rx Antenna Gain(dBi)
Azimuth(°)

(b)

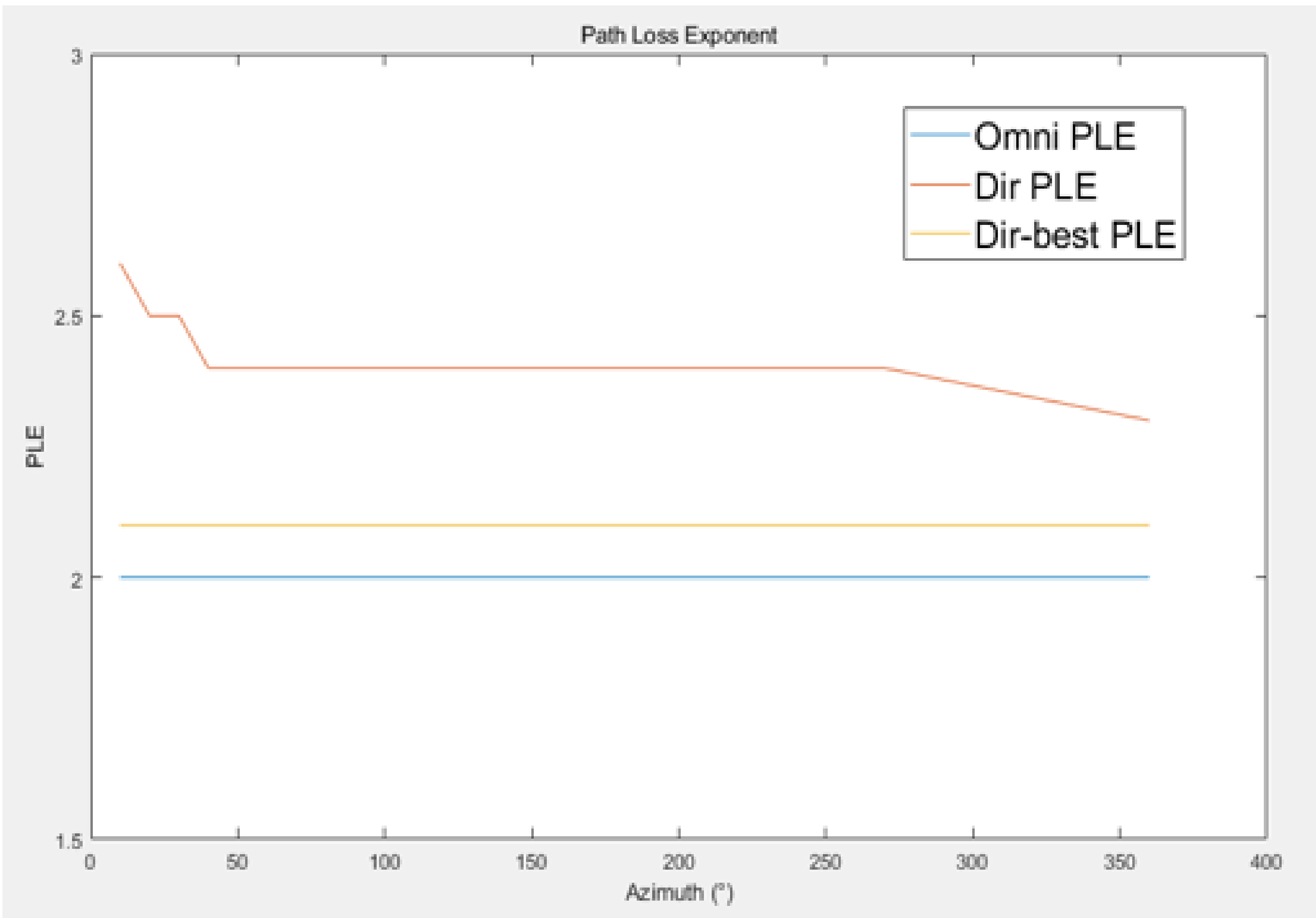
Path Loss Exponent
Omni PLE
Dir PLE
Dir-best PLE
PLE
Azimuth (°)

(c)

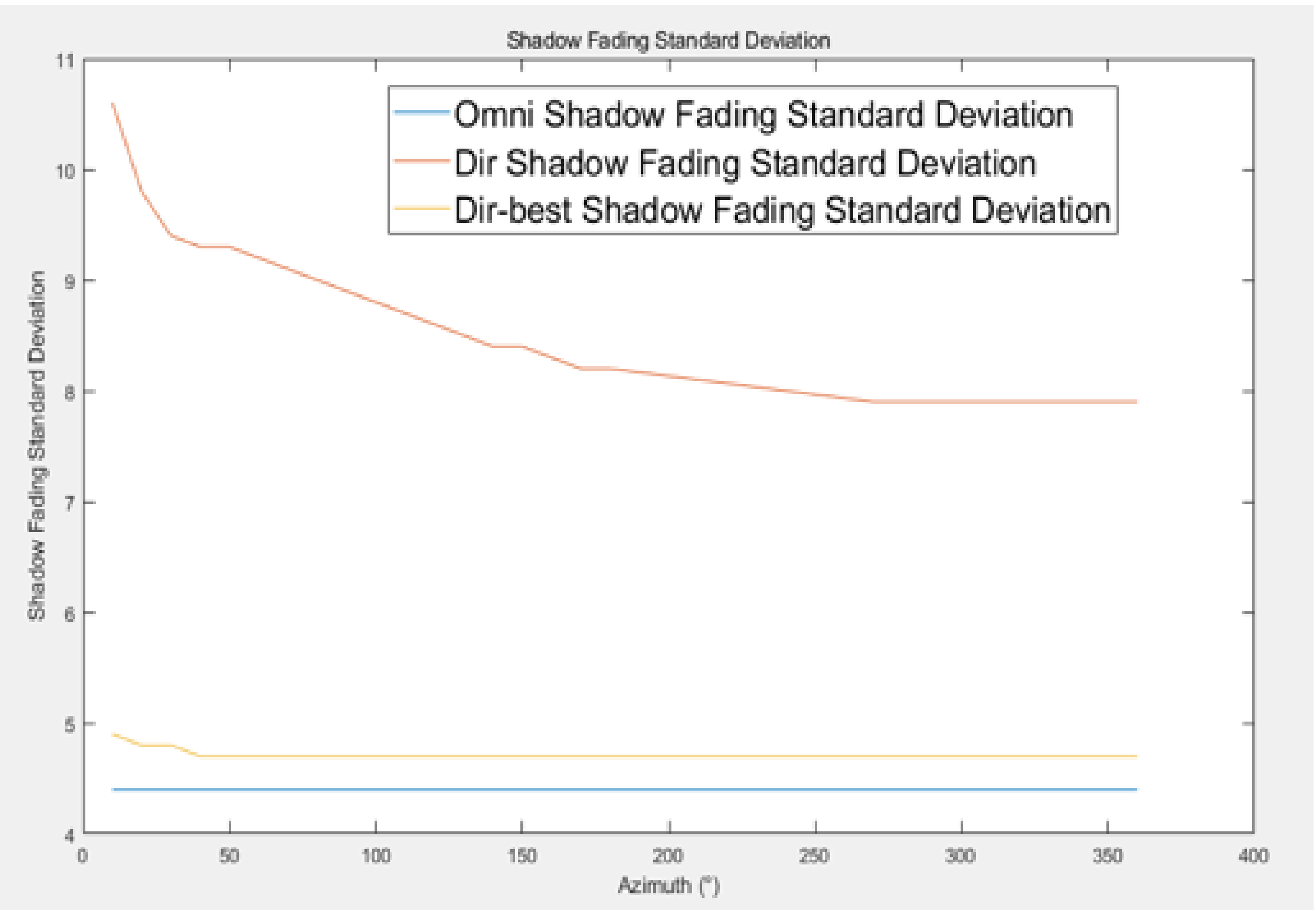
Shadow Fading Standard Deviation
Omni Shadow Fading Standard Deviation
Dir Shadow Fading Standard Deviation
Dir-best Shadow Fading Standard Deviation
Shadow Fading Standard Deviation
Azimuth (°)

(d)

Figure 20.

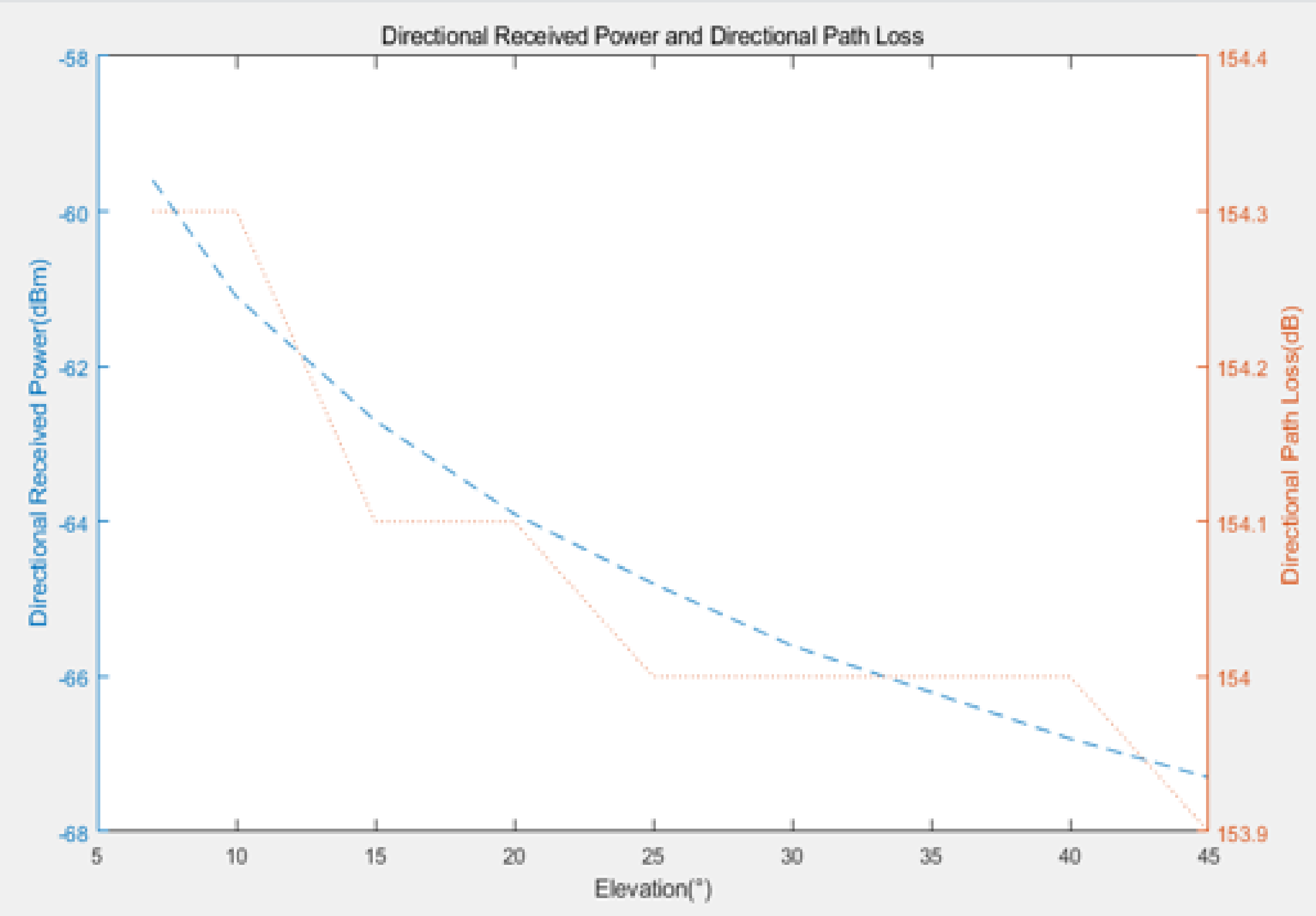
Directional Received Power and Directional Path Loss
Directional Received Power(dBm)
Directional Path Loss(dB)
Elevation(°)
-58
-60
-62
-64
-66
-68
154.4
154.3
154.2
154.1
154
153.9
5
10
15
20
25
30
35
40
45

(a)

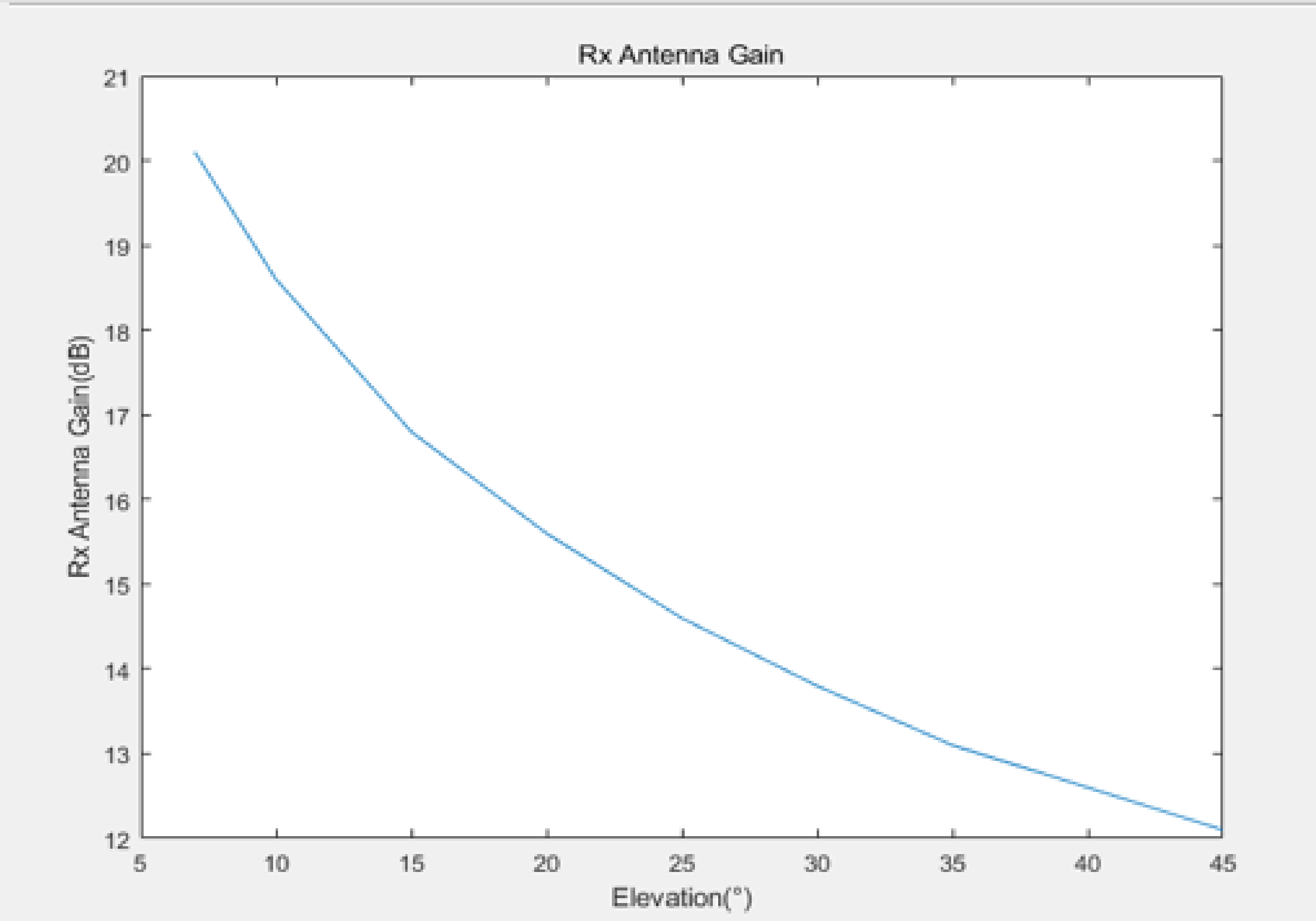
Rx Antenna Gain
Rx Antenna Gain(dB)
Elevation(°)
21
20
19
18
17
16
15
14
13
12
5
10
15
20
25
30
35
40
45

(b)

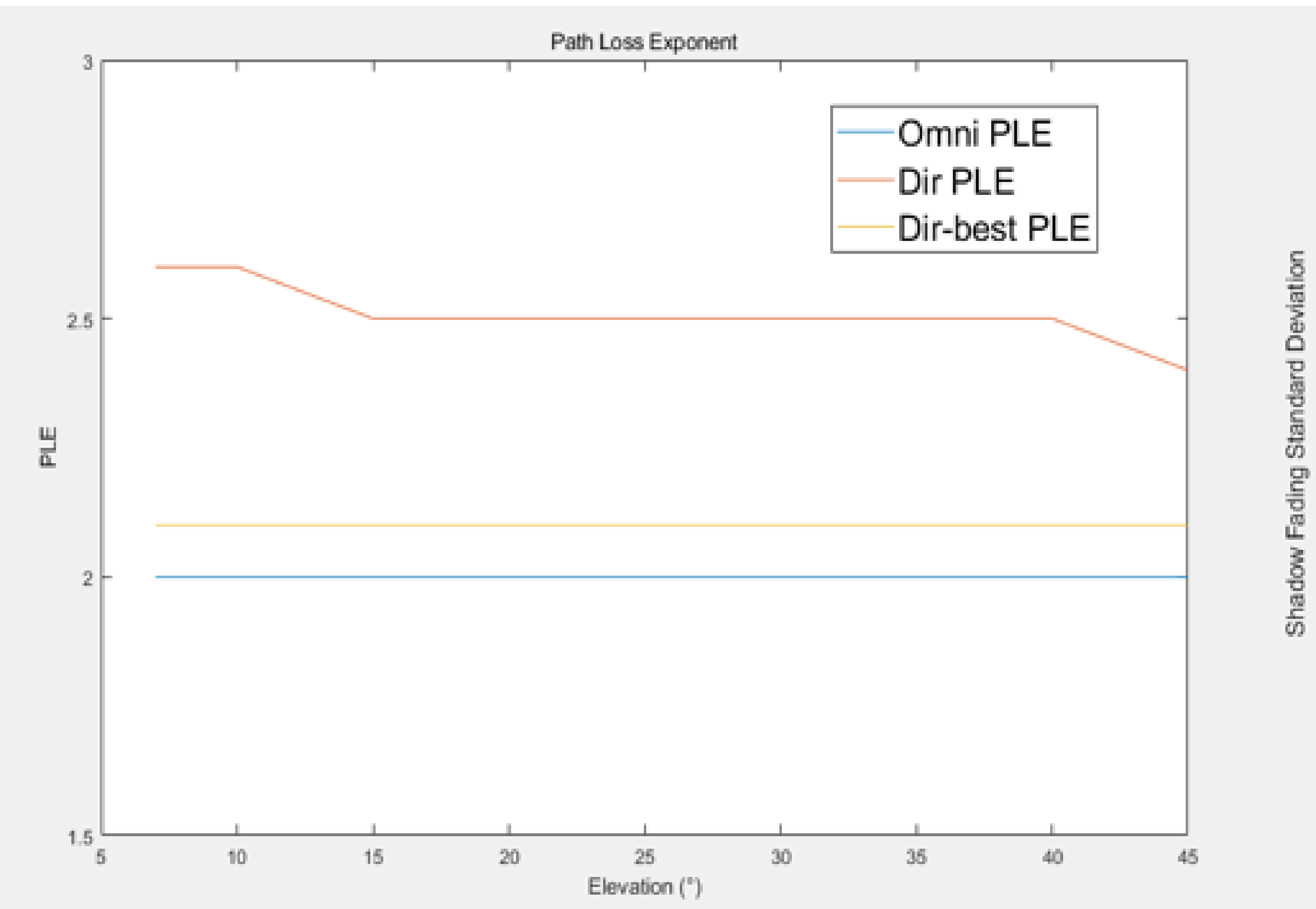
Path Loss Exponent
PLE
Elevation (°)
Omni PLE
Dir PLE
Dir-best PLE
3
2.5
2
1.5
5
10
15
20
25
30
35
40
45

(c)

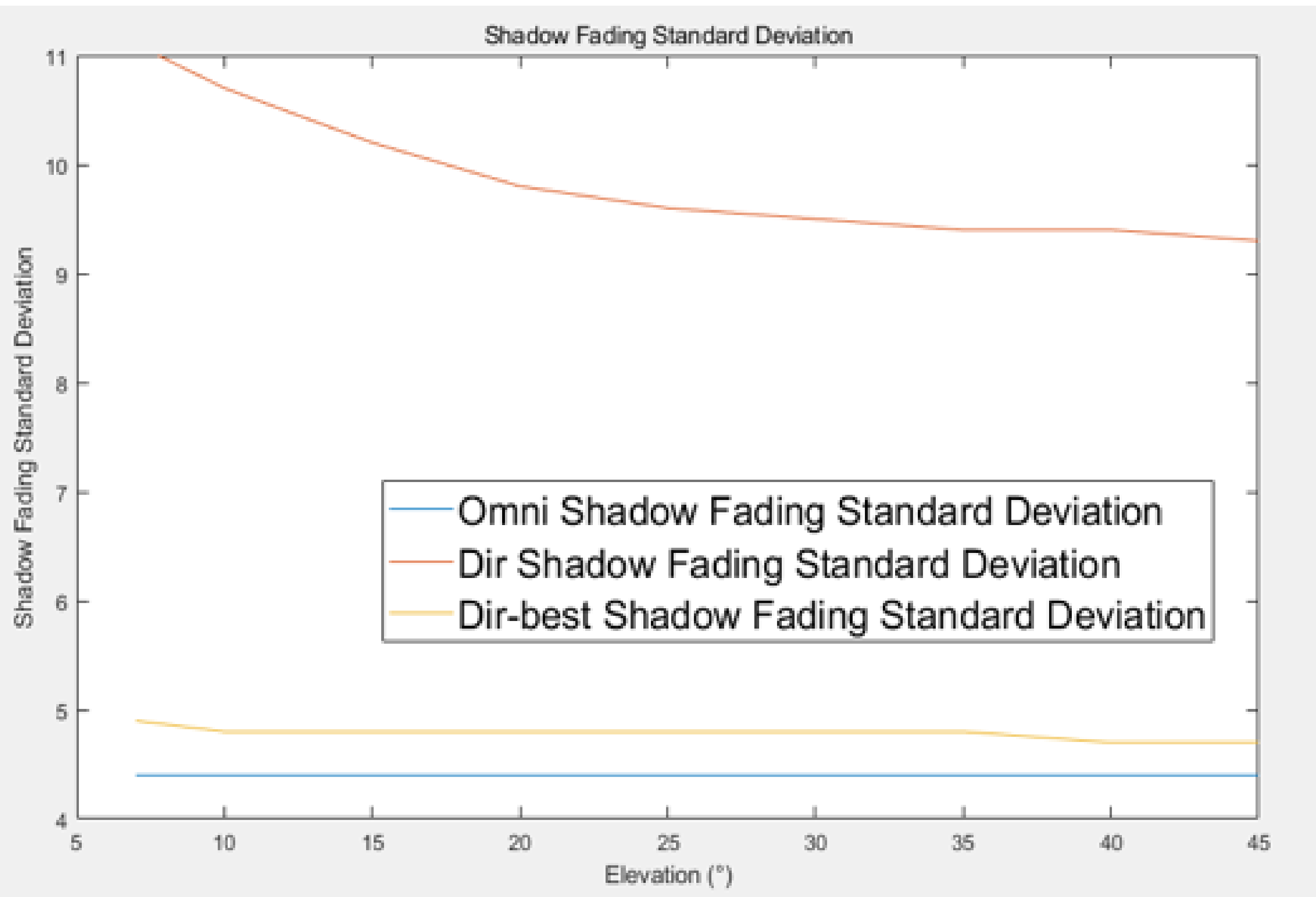
Shadow Fading Standard Deviation
Shadow Fading Standard Deviation
Elevation (°)
Omni Shadow Fading Standard Deviation
Dir Shadow Fading Standard Deviation
Dir-best Shadow Fading Standard Deviation
11
10
9
8
7
6
5
4
5
10
15
20
25
30
35
40
45

(d)